

**RESEARCH PERFORMANCE PROGRESS REPORT**

**U.S. Department of Energy National Energy Technology Laboratory**

**Cooperative Agreement: DE-FE0031558**

**Project Title: Partnership for Offshore Carbon Storage Resources and Technology Development in the Gulf of Mexico**

**Principal Investigator: Dr. Susan Hovorka**

**PH: 512-471-4863**

[susan.hovorka@beg.utexas.edu](mailto:susan.hovorka@beg.utexas.edu)

**Co-Principal Investigator: Dr. Tip Meckel**

**PH: 512-471-4306**

[tip.meckel@beg.utexas.edu](mailto:tip.meckel@beg.utexas.edu)

**Co-Principal Investigator: Mr. Ramon Trevino**

**PH: 512-471-3362**

[ramon.trevino@beg.utexas.edu](mailto:ramon.trevino@beg.utexas.edu)

**Submission Date: December 31, 2020**

**DUNS Number: 170230239**

**The University of Texas at Austin  
Jackson School of Geosciences  
Bureau of Economic Geology  
University Station, Box X  
Austin, Texas, 78713**

**Project Period: April 1, 2018 – March 31, 2023**

**Reporting Period End Date: December 31, 2019**

**Report Frequency: Quarterly**

**Signature Submitting Official: \_\_\_\_\_**

## **EXECUTIVE SUMMARY OF RESEARCH DEVELOPMENTS DURING THIS QUARTER**

### Project Management

Milestone 4, “Identification of Geologic storage prospects and data gaps,” and Deliverable 4.1a “Table of MVS technologies and methodologies” were submitted.

Due to logistical and other considerations, the planned BP1 HR3D seismic survey acquisition will not occur before the end of BP1. Consequently, a request for a no-cost extension (NCE) of BP1 until December 31, 2020 was submitted to the NETL project manager (PM) and contract specialist.

A subrecipient agreement was signed with Aker Solutions US, Inc. (FGO) in mid-December.

### Offshore Storage Resource Assessment

Undergraduate research assistants continued to populate the Petra™ project with well curve raster images and digitized well log curves.

A key stratigraphic horizon (MFS09) has been mapped throughout several 3D seismic volumes and has been subsequently extended through the entire new Offshore OBS South 3D seismic volume; structural interpretations include 709 fault polygons.

As of December 2019, the MFS09 surface has been interpreted throughout the West Cameron Fairfield 3D survey provided by the National Archive of Marine Seismic Surveys (NAMSS). This additional 3D survey helps extend our understanding of the subsurface structure of this important seal interval in the Offshore Louisiana Federal waters.

Three regional, well-log strike cross sections comprising approximately 100 wells each and seven regional, well-log cross-sections of about 12 wells each were constructed across the mid-Texas coast study area.

As with the lower Miocene succession previously correlated along the upper Texas coast, the *Amphistegina B* shale associated with a regional transgressive flooding event is also a prominent marker in the current study area and constitutes a firm tie to the stratigraphic sections of the upper coast areas.

Sonic and density well-log curves for five wells in the mid-Texas coast have been identified, purchased and will be used to help tie the seismic volume (currently in the time domain) with the correlated surfaces on the well logs (in depth). Moreover, check-shot data for an additional 29 wells in the area have been purchased to further integrate the stratigraphy with the seismic profiles.

High-resolution datasets can be used as analogues for an assessment of the buoyant storage volume of the lower Miocene in the Gulf of Mexico. The USGS buoyant storage methodology (Brennan et al., 2010; Blondes et al., 2013) uses data of known hydrocarbon production and reserves as well as the estimated undiscovered hydrocarbons to create a distribution of possible pore volume available for buoyant storage. The analogues and geologic structural surfaces within an assessment unit are used to estimate a maximum potential buoyant storage volume to complete the boundaries of the distribution.

Using previously interpreted surfaces as inputs, a PaleoScan™ (from Eliis, Inc.) multi-surface automated surface framework was generated through the interval of interest in the Chandeleur Sound area. This included a sequence of 100 auto-generated surfaces produced from seismic peak, troughs, and seismic inflections.

## Risk Assessment

We invert petroleum exploration approaches at a geologic play level to assess subsurface risks to long-term storage, as a mechanism to lower cost and increased security. Basin-scale screening, play definition and prospect description are core tasks of petroleum exploration however and there is a well-defined suite of tools to deal with the problem. The work described here are the first steps in adapting and applying those tools to the identification of CCS sites. We focus on the U.S. Gulf of Mexico as it is a well-understood petroleum basin and the Gulf Coast is a hub of CO<sub>2</sub> emissions.

## Geologic Modeling

Part I of a final report on Compressibility Effects on Viscous Instability Under Sealing and Partially Sealing Boundaries was submitted. See Appendix I.

## Monitoring, Verification, and Assessment (MVA)

In the past quarter we revised, proofed, and published our paper documenting the analysis of a marine DAS experiment conducted near Moss Landing, CA in the Monterey Bay. As mentioned in the last quarterly, the DAS experiment successfully observed a sequence of mapped and unmapped faults near the seafloor using the passive noise field, mainly mode conversions generated by local earthquakes. The combination of fault identification and EQ detection suggest two modes that future seafloor DAS cables might be utilized in the context of GCS. The final publication information for the paper is:

Lindsey, N., Dawe, C.T., and **J.B. Ajo-Franklin**, “Illuminating seafloor faults and ocean dynamics with dark fiber distributed acoustic sensing”. *Science*, Vol. 366, No. 6469, pp. 1103-1107. DOI: 10.1126/science.aay5881

We are now developing a processing flow to utilize non-EQ ambient noise to image the same fault zones at finer resolutions.

Three stations in the High Island 10L region are used to collect environmental conditions. The stations are located at the Sabine Pass, Sabine Bank Channel, and the Galveston Bay Entrance

The scenario of CO<sub>2</sub> leak from the High Island 10 L Injection Well was evaluated. The worst case scenario for the CO<sub>2</sub> leakage was assumed, total rupture of the pipe at the top of the injection well (bottom of the ocean). The flow rate of CO<sub>2</sub> that can be injected to the well is approximately 195,000 lb/hr. The pipe diameter size utilized in the study is 4”. Table 4.1 was used to select the pipe size. The leakage of CO<sub>2</sub> was evaluated using the computational fluid dynamics (CFD) software Ansys Fluent.

## Infrastructure, Operations and Permitting

Trimeric reviewed various literature sources and talked with industry experts about offshore infrastructure and its reuse. As Trimeric has gathered data on existing infrastructure in the GoM and applied screening criteria in analog/proxy regions, Trimeric has developed and updated a work flow/research approach for evaluating infrastructure. The goal of this workflow is to document the high-level methodology used in the infrastructure evaluation and organize research activities moving forward (e.g., assessment of other infrastructure).

- In Trimeric’s interview with an oil and gas industry expert, the expert provided several important insights. Regarding pipelines, the industry expert believed that most large

diameter pipelines would be in use.

- Cited a project in Louisiana where a pipeline was re-used (CO<sub>2</sub> for EOR), but the pipeline quality necessitated the use of multiple booster stations to limit the maximum pressure in the pipeline during transport.

Expert cited familiarity with both public and private tools to evaluate existing pipeline data in Texas and Louisiana state waters as well as associated federal data. Trimeric will engage the expert for further evaluation of pipeline data in Q1 2020.

During the most recent quarter, Trimeric continued the development of an LNG case study to facilitate outreach in the region and develop a basis for potential scenario optimization moving forward. Trimeric will further develop a case study for LNG as a CO<sub>2</sub> source for storage in the Gulf of Mexico, as several LNG facilities are starting-up in Texas and Louisiana.

### Knowledge Dissemination

[GoMCarb](#) project consultant, Dr. Robert J. Finley, traveled to Austin to teach a class to GCCC first-year master's students. Finley has a long and celebrated career in geology, including decades at the Bureau of Economic Geology and the Illinois State Geological Survey. The class, titled "An Introduction to Some Concepts of Reservoir Heterogeneity," explored how different sedimentary depositional systems affect reservoir quality (and ultimately capacity) for carbon dioxide injection, providing a more nuanced view of reservoir models particularly relevant to sand intervals that are potential targets for CO<sub>2</sub> injection.

## **Task 1.0 – Project Management, Planning, and Reporting**

Milestone 4, “Identification of Geologic storage prospects and data gaps,” was submitted November 1. Project co-PIs met with Partner, Trimeric Corp. on November 18. (See Subtask 5.1.)

Due to logistical and other considerations, the planned BP1 HR3D seismic survey acquisition will not occur before the end of BP1. Consequently, a request for a no-cost extension (NCE) of BP1 until December 31, 2020 was submitted to the NETL project manager (PM) and contract specialist.

In order to clarify disparities between enumerated deliverables in the SOPO and the PMP, a new Gantt chart was generated, which corrected the disparities. A revised PMP (with corrected Gantt) was submitted on December 18, 2019. Deliverable D4.1a was submitted on December 20, 2019.

A subrecipient agreement was signed with Aker Solutions US, Inc. (FGO) in mid-December.

On November 11, 2019, HR3D seismic system equipment previously ordered and received from Geometrics, Inc. was tested and approved (Figure 1.1).

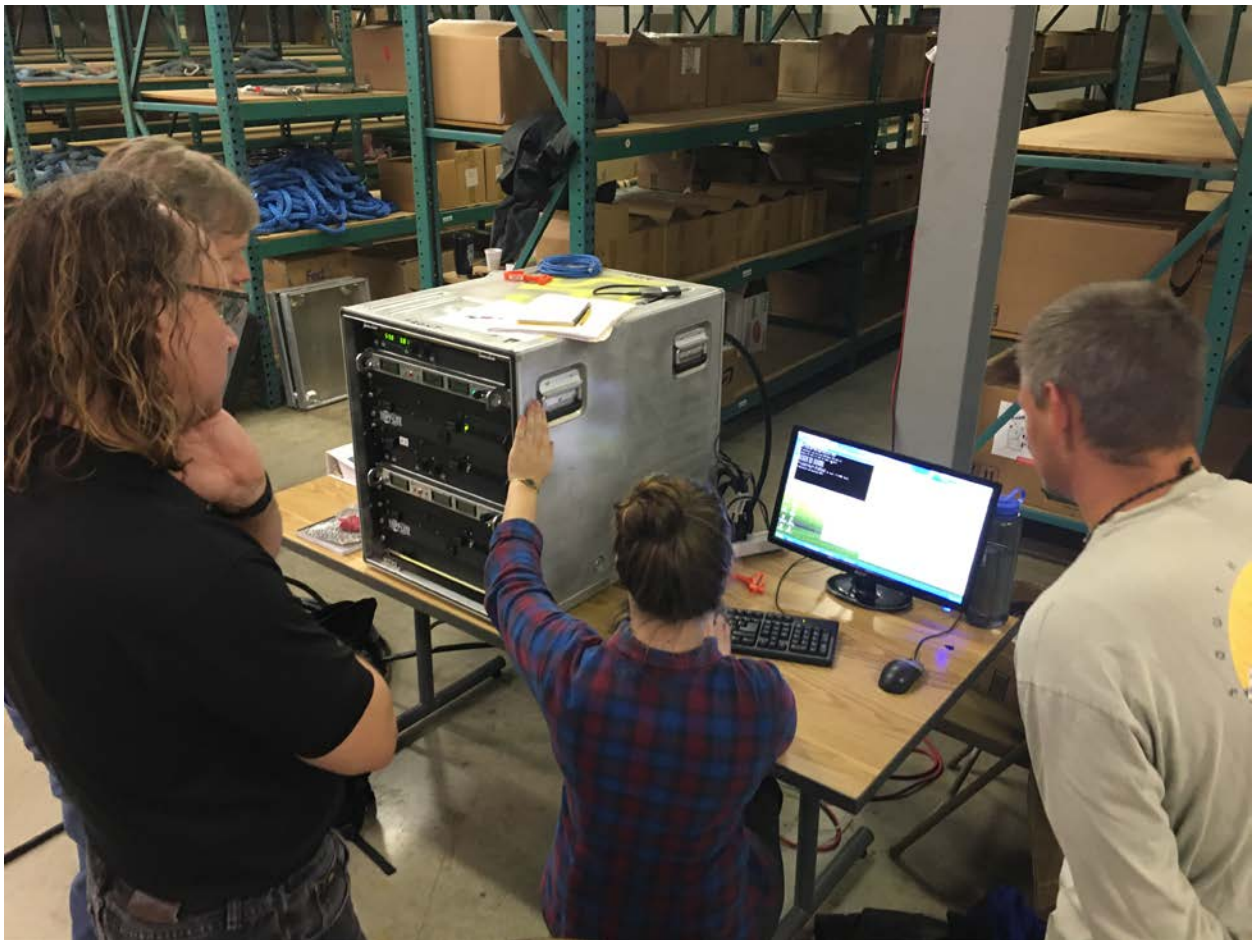


Figure 1.1 – Testing of new HR3D equipment at BEG’s Houston Research Center (HRC).

## **Task 2.0 – Offshore Storage Resource Assessment**

### **Subtask 2.1 – Database development:**

#### Well Database

During the quarterly reporting period, three undergraduate research assistants continued to populate the Petra™ project with well curve raster images and digitized well log curves. They did this by loading raster images from available sources (e.g., Lexco OWL7) and digitizing log curves from the images, thus, generating digital LAS (Log ASCII Standard) curves. Primarily, SP (spontaneous potential) curves have been digitized because they are used to define log facies and correlate wells. The total number of wells with LAS curves as of the end of the reporting period was 200. Figures 2.1.1 and 2.1.2 illustrate the distribution of wells and the primary 3D seismic datasets within the project area and also show lines of section for three regional well-log cross sections.

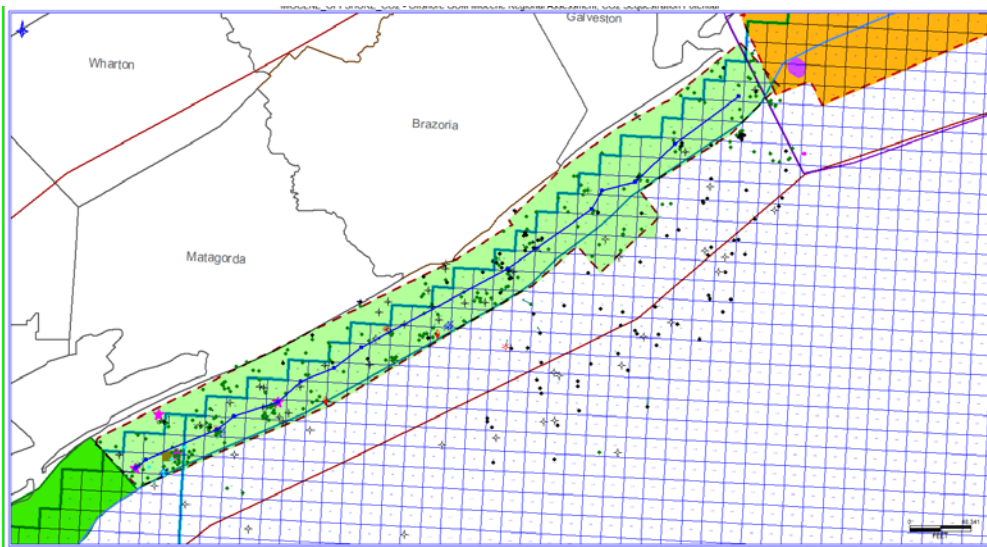


**Figure 2.1.1** – Map of the study area from Matagorda to Galveston Counties showing the OBS 3D seismic survey (highlighted in green) The state - federal waters boundary is demarcated by the blue line subparallel to the coast. There are 446 wells in this portion of the study area, 431 of which have wireline well log raster data only (black dots) and 347 of which have digital SP curves (green dots). The line of section of regional stratigraphic strike cross-section in Figure is shown in blue.

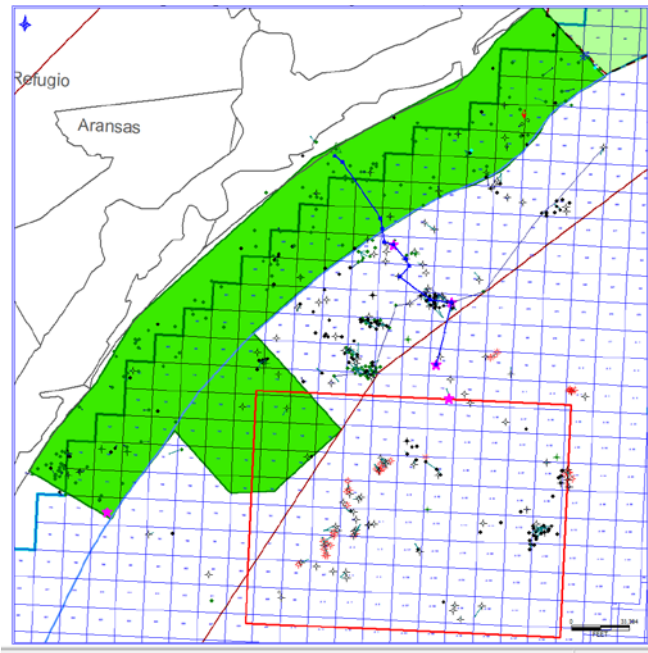


**Figure 2.1.2** – Map of the study area showing the OBS South 3D seismic survey (highlighted in green) The state - federal waters boundary is demarcated by the blue line subparallel to the coast. There are 540 wells in total, 460 of which have wireline well log raster data only (black dots) and 272 wells have digital SP curves (green dots). Strike (Fig. 4) and dip cross-sections (Fig. 5) are indicated in blue.

### Seismic Database

Seismic based investigations of the GOMCarb CO<sub>2</sub> project are continuing. Previous results from the regional seismic studies, Offshore OBS, TexLA Merge 3D, and Chandeleur Sound 3D will be augmented by new publicly available 3D seismic data volumes from the National Archive of Marine Seismic Surveys (NAMSS) (Figure 2.1.3).

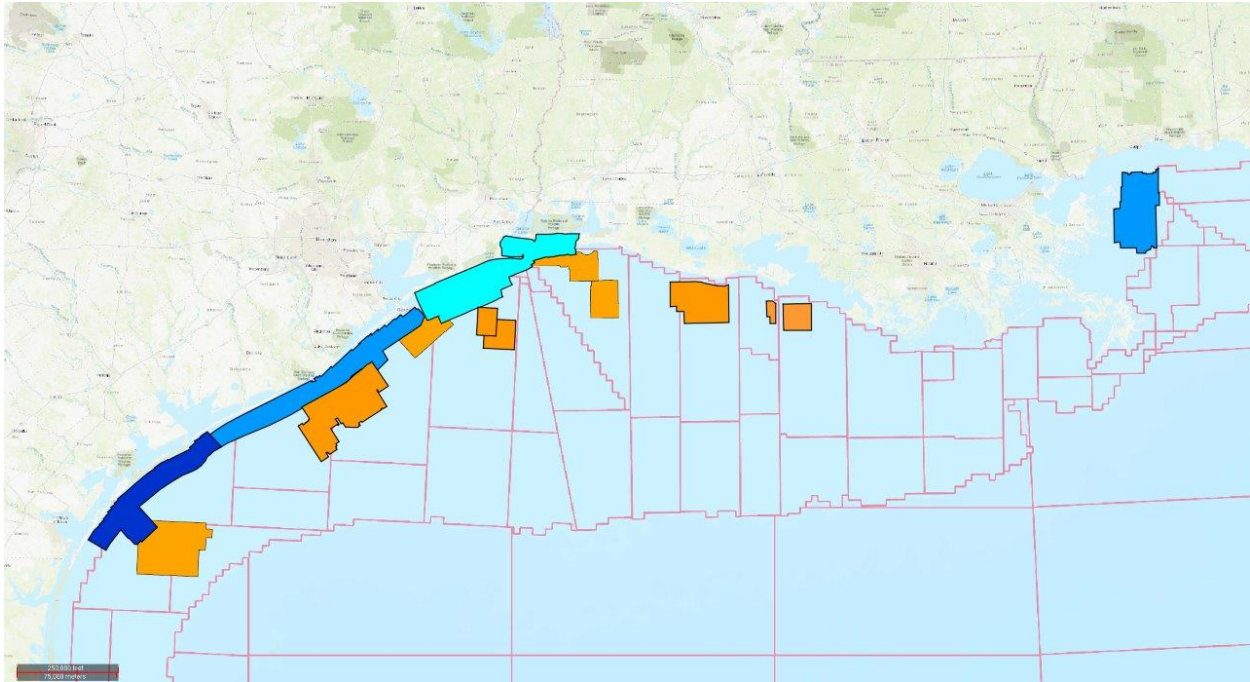


Figure 2.1.3 Basemap of GOMCarb 3D seismic volumes. From left to right: Offshore OBS South 3D (Cobalt blue), Offshore OBS 3D (Cerulean blue), TXLA Merge (Turquoise blue), and Chandeleur Sound 3D (Cerulean blue), and publicly available NAMSS 3D seismic data sets (Orange).

A key stratigraphic horizon (MFS09) has been mapped throughout several 3D seismic volumes and has been subsequently extended through the entire new Offshore OBS South 3D seismic volume (Figure 2.1.4). These key features will then be used to build detailed 3D models that can be used in a variety of reservoir characterization simulations. Structural interpretations include 709 fault polygons (Figure 2.1.5) identified while mapping the MFS09 surface.

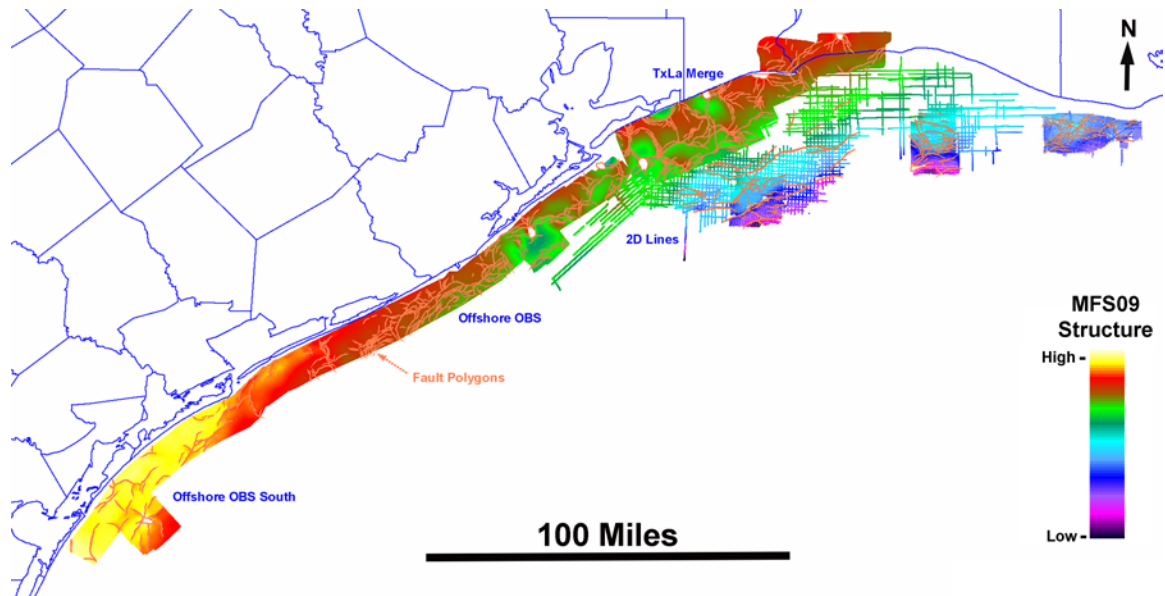


Figure 2.1.4 – Regionally interpreted MFS09 surface, including the Offshore OBS South 3D survey.



Figure 2.1.5 – Regionally interpreted MFS09 fault polygons, including the Offshore OBS South 3D survey. There are 709 fault polygons in this image.

**Subtask 2.1.1 – Geographic Focus Area A - Lake Jackson, Lake Charles, and Lafayette (OCS) districts**

### Subtask 2.1.1.1 Western Louisiana, Lafayette and Lake Charles Districts

As of December 2019, the MFS09 surface has been interpreted throughout the West Cameron Fairfield 3D survey (Figure 2.1.1.1) provided by the National Archive of Marine Seismic Surveys (NAMSS). This additional 3D survey helps extend our understanding of the subsurface structure of this important seal interval in the Offshore Louisiana Federal waters.

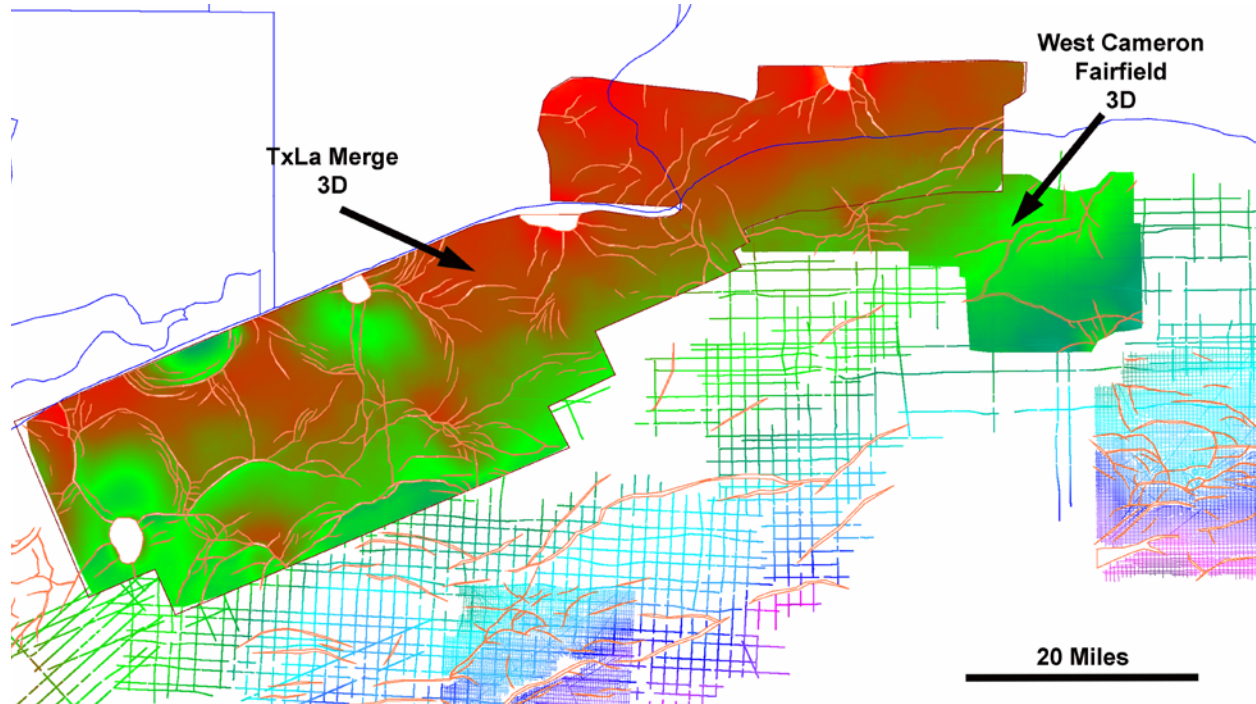
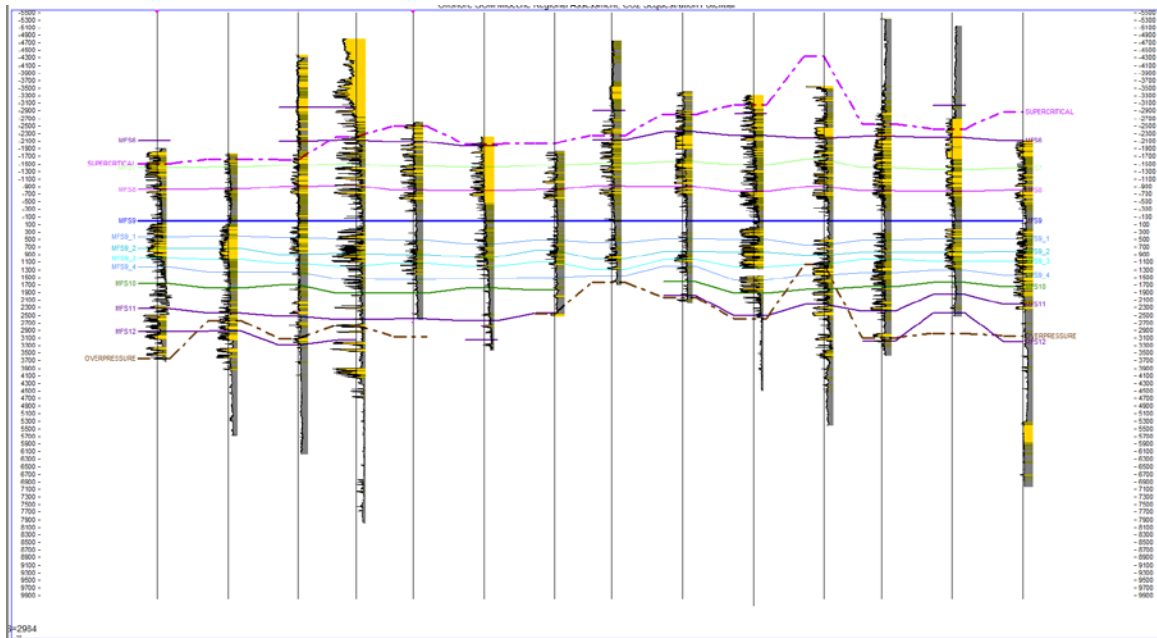


Figure 2.1.1.1 – The structure map of MFS09 that extends into the West Cameron Fairfield 3D survey.

### Subtask 2.1.1.2 Mid-Texas coast offshore Houston to Corpus Christi

The upper depth limit for CO<sub>2</sub> injection is determined by the minimum temperature and pressure conditions at which CO<sub>2</sub> is supercritical (about 3300 ft). The lower depth limit for CO<sub>2</sub> injection is determined by the depth at which the hydrostatic pressure in the subsurface significantly exceeds the expected pressure for a particular depth. The top of overpressure shown on the cross sections in Figures 2.1.1.2.1 - 2.1.1.2.3 comes from a U.S. Geological Survey regional geopressure-gradient model of the pressure system spanning the onshore and offshore portions of Texas and Louisiana (Pitman, 2011) (Burke et al., 2012).

A preliminary interpretation indicates that the primary reservoir targets along the middle Texas coast are Lower Miocene sandstone reservoirs between MFS 9 and MFS 10 (Figures 2.1.1.2.1 – 2.1.1.2.3) and the primary sealing unit is the regional transgressive shale unit associated with *Amphistegina B* (“Amph B”) biochronozone. In places the Amph B unit can reach a thickness of approximately 200 m. The supercritical depth roughly coincides with MFS 6 and MFS7, and the depth of the overpressure is reached at (MFS 11 and MFS 12) the base of the Lower Miocene. Note that the depth at which CO<sub>2</sub> will remain in a supercritical state (dashed magenta line) is assumed to be approximately 1000 meters (~3300 ft) throughout the area, and on a structural cross section, this is a horizontal line. Conversely, the top to overpressure (dashed brown line) varies according to local conditions in the geologic section.



**Figure 2.1.1.2.1** – Strike-oriented stratigraphic cross-section, offshore Texas coast between Galveston and Matagorda Bay. See Figure 2.1.1 for the line of section. The cross section is flattened on MFS9. Note the supercritical depth and top to overpressure (dashed lines), which vary as would be expected for a stratigraphic cross section.

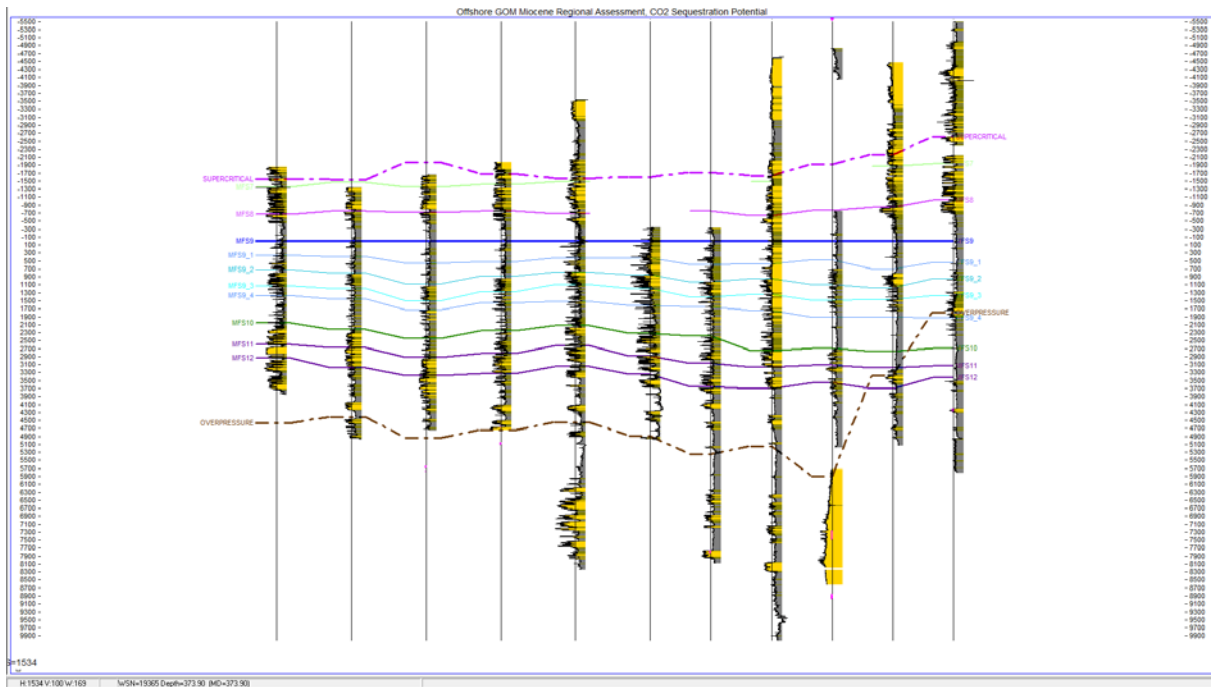


**Figure 2.1.1.2.2** – Strike-oriented stratigraphic cross-section, offshore Texas coast between Matagorda and Corpus Christi Bay. The cross section is flattened on MFS9. Note the supercritical depth and top of overpressure (dashed lines), which vary as would be expected for a stratigraphic cross section.

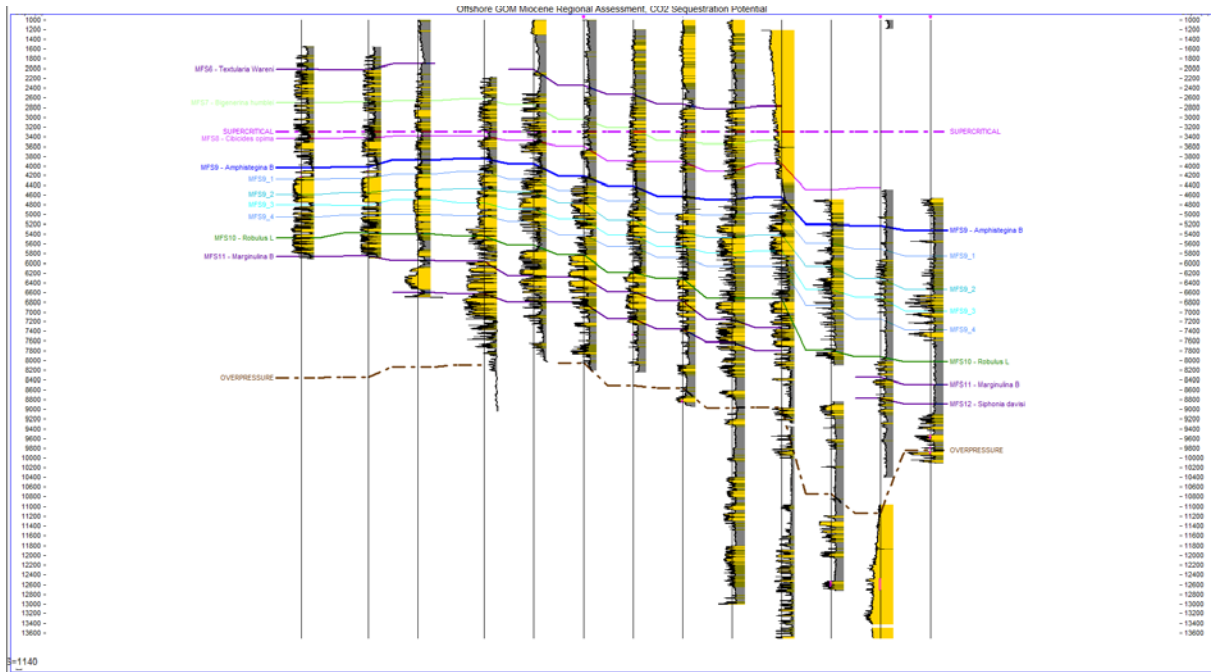


**Figure 2.1.1.2.3** – Dip-oriented structural cross-section, offshore Texas coast. The top of the overpressure coincides roughly with the base of the Lower Miocene.

Three regional, well-log strike cross sections comprising approximately 100 wells each and seven regional, well-log cross-sections of about 12 wells each were constructed across the study area (Figure 2.1.1.2.4). Within these lines, three low-order sequences (including sequence boundaries, transgressive surfaces of erosion, and maximum flooding surfaces) were correlated in the lower Miocene succession, and the Anahuac Shale was identified and correlated in the Oligocene section. Figure 2.1.1.2.5, which composes a central portion of cross section Strike 2-2', provides an example of the correlations.

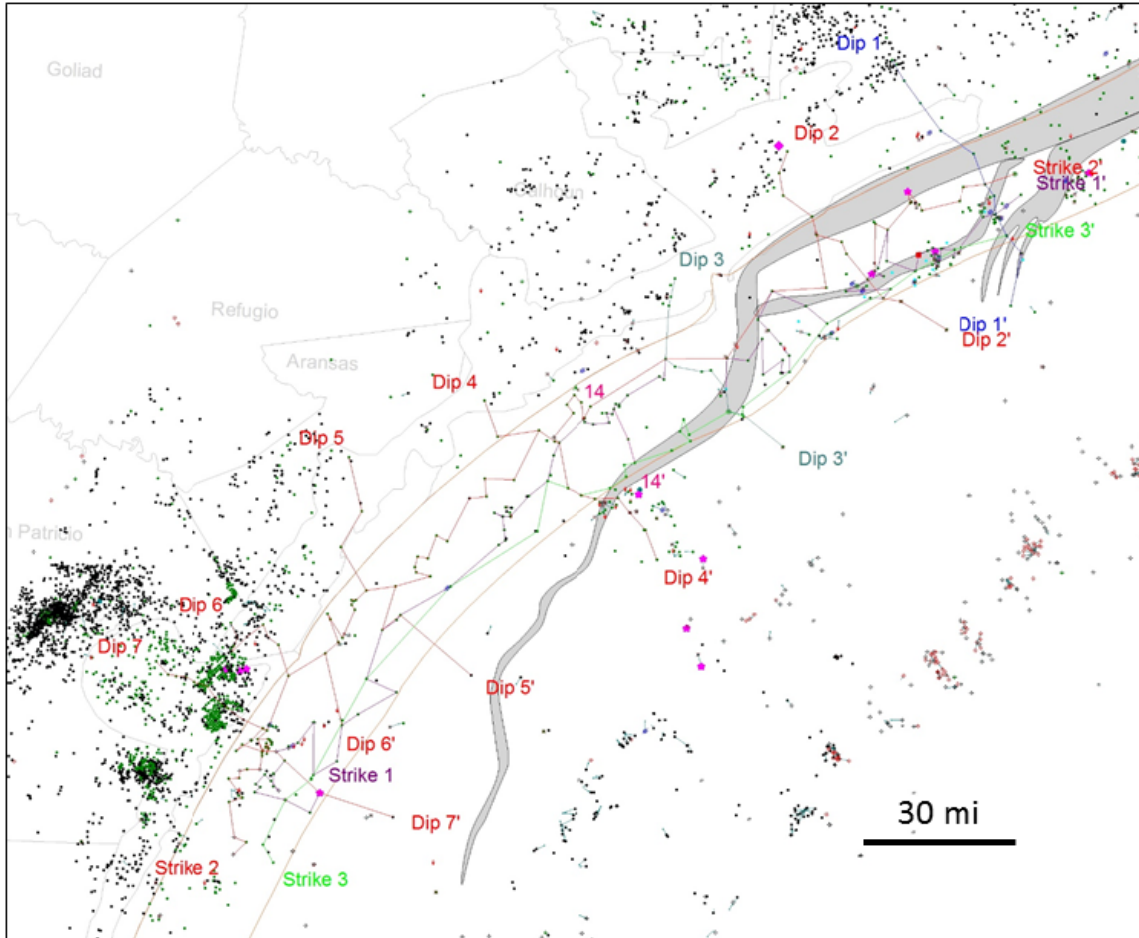


Figure 2.1.1.2.4 – Map showing three regional strike (i.e., Strike 1, Strike 2 and Strike 3), and seven dip (i.e., Dip 1 through Dip 7) well-log cross sections in the study area. Note that numbering of the dip cross sections goes north to south with “Dip 1” farthest north and “Dip 7” farthest south.

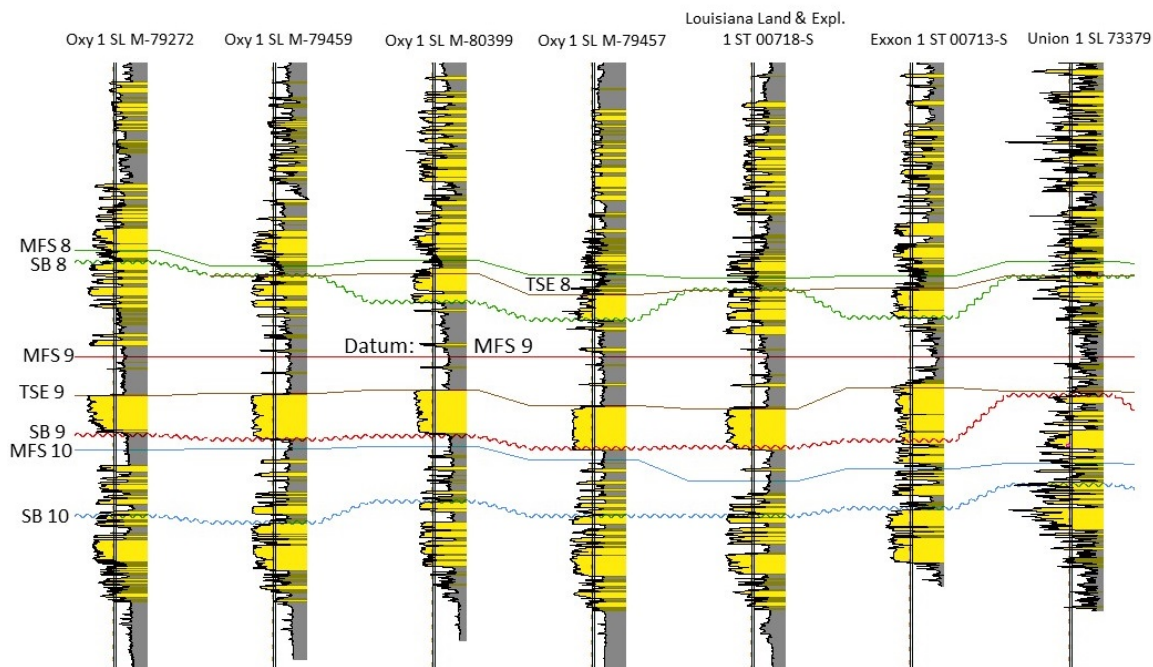


Figure 2.1.1.2.5 – A central portion of cross section, Strike 2-2'. The cross section is oriented along depositional-strike. Note inferred sequence-stratigraphic surfaces (SB = sequence boundary, TSE = transgressive surface of erosion, MFS = maximum flooding surface). MFS 9 marks the approximate *Amphistegina B* biostratigraphic extinction horizon. Wells are non-proportionally (evenly) spaced over a distance of about 5 mi.

As with the lower Miocene succession previously correlated along the upper Texas coast, the *Amphistegina B* shale associated with a regional transgressive flooding event is also a prominent marker in the current study area and constitutes a firm tie to the stratigraphic sections of the upper coast areas. Nonetheless, identification of all correlated surfaces is tentative until the surfaces are integrated into the 3-D seismic volume to confirm regional equivalency. Toward that end, paired sonic and density well-log curves for five wells in the area (Table 2.1.1.2.1, Figure 2.1.1.2.6) have been identified and will be used to help tie the seismic volume (currently in the time domain) with the correlated surfaces on the well logs (in depth). Moreover, check-shot data for an additional 29 wells in the area (Table 2, Figure 3) have been purchased to further integrate the stratigraphy with the seismic profiles.

Table 2.1.1.2.1 – Wells with sonic and velocity data.

<b>API number</b>	<b>Well name</b>
42602300090000	SABCO B-1 SL 41338
42602301710000	Louisiana Land 1 ST TR 00883-S
42603301410000	Louisiana Land 1 SL 79455
42703300120000	Mobil 1 ST TR 00632-L
42703303190000	SONAT 1 SL 80375

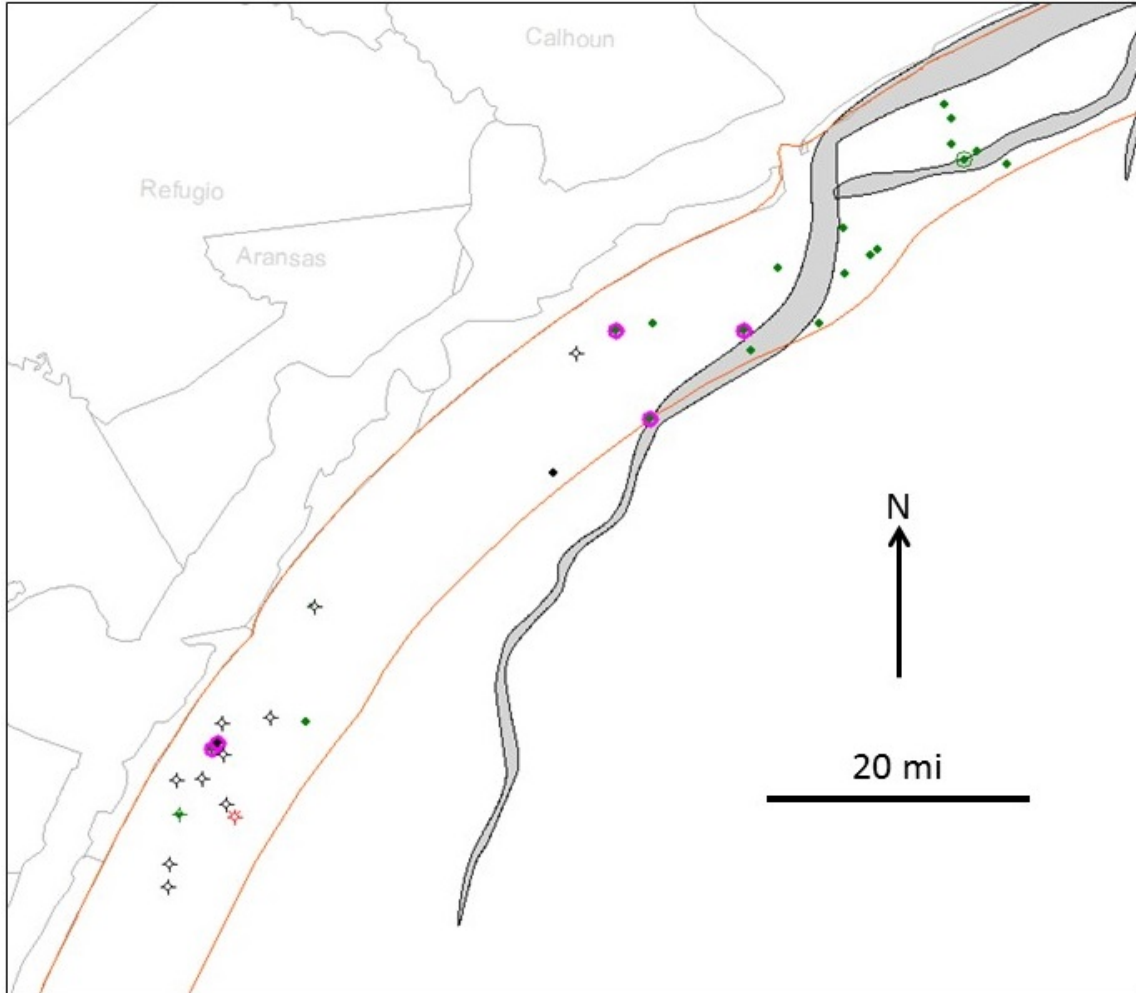


Figure 2.1.1.2.6 – Map of five wells with sonic and density data (magenta highlights) and 29 wells with check shot data.

Table 2.1.1.2.2 – Wells with check-shot data

<u>API number</u>	<u>Well name</u>
42603300020000	Corpus Christi 1 ST TR 00722-S
42603300230000	Mesa 1 ST TR 00607-S
42603301280000	Oxy 1 SL M-79457
42703000120000	Humble 1 ST TR 00558-L
42703000380000	Shell 1 ST TR 00520-L NW/4
42703000420000	Coastal States 1 ST TR 00592-L
42703300120000	Mobil 1 ST TR 00632-L

42703300240000	Monsanto 1 ST TR 00562-L
42703300590000	Corpus Christi 1 ST TR 00519-L NW/4
42703301400000	Kirby 3 SL 69112
42703301440000	Zapata 1 SL 68984
42703301820000	Choctaw 1 SL M-77985
42703302010000	McMoran 1 ST TR 00484-L SE/4
42703302240000	Mesa 1 ST TR 00484-L NE/4
42703302310000	Mesa 1 ST TR 00559-L SE/4
42703302570000	C&K 1 ST TR 00658-L SW/4
42703303300000	Getty 1 ST TR 00599-L
42703303340000	McMoran 2 STATE TRACT 564-L N
42602301360000	Texas Gas 1 SL 83914
42602301610000	Challenger 1 ST TR 00895-S
42702000010000	Humble 1 ST TR 00772-L
42702000150000	Cities Service 1 ST TR 00796-L
42702000170000	Cities Service 1 ST TR 00773-L
42702300130000	Houston Oil 1 ST TR 00749-L
42702300240000	Partick 1 SL 00774
42702301470000	Patick 3 ST TR 00774-L
42702301630000	Exxon 1 ST TR 00750-L
42702301970000	Hunt 1 SL 78094
42702302150000	Zapata 1 ST TR 00796-L NE/4

### Subtask 2.1.1.3 Buoyant storage capacity

The U.S. Geological Survey (“USGS”) is tasked with estimating the buoyant CO<sub>2</sub> storage resource in the state waters of Texas and Louisiana, and the federal waters offshore Texas and western Louisiana. As part of the initial phases of this task the focus has been on using high resolution data of the lower Miocene strata from two blocks offshore Texas. These data and interpretations are from two separate Master’s theses (Garcia, 2019; Ruiz, 2019). The sections have interpreted trap volumes identified from surfaces modeled using interpreted tops data from well logs and seismic data. The porosity within the traps have been estimated using well log data, allowing estimates of pore volume available for buoyant storage.

These high-resolution datasets can be used as analogues for an assessment of the buoyant storage volume of the lower Miocene in the Gulf of Mexico. The USGS buoyant storage methodology (Brennan et al., 2010; Blondes et al., 2013) uses data of known hydrocarbon production and reserves as well as the estimated undiscovered hydrocarbons to create a distribution of possible pore volume available for buoyant storage. The analogues and geologic structural surfaces within an assessment unit are used to estimate a maximum potential buoyant storage volume to complete the boundaries of the distribution.

The USGS has been gathering data of production within the lower Miocene shelf reservoirs in the relevant assessment area, along with the Bureau of Ocean Energy Management (“BOEM”) undiscovered hydrocarbon assessment of the lower Miocene Gulf of Mexico shelf. The reservoir data are derived from the Nehring dataset of significant oil and gas reservoirs (NRG Associates, 2018) and the USGS Comprehensive Resource Database (“CRD”) (Carolus et al., 2018), which have relevant reservoir data that can be used to characterize assessment units. The undiscovered estimates are from BOEM’s 2014 undiscovered hydrocarbon assessment of the Gulf of Mexico (BOEM, 2017). These data, along with the high-resolution data from the Master’s theses (Garcia, 2019; Ruiz, 2019) have been brought into a GIS project in order to see where existing reservoirs are located and the area where the undiscovered hydrocarbon resources are estimated to reside.

The next steps will be to work with the Gulf Coast Carbon Center (GCCC) at the Texas Bureau of Economic Geology on getting structural maps of relevant horizons in the lower Miocene, and to determine how the high-resolution data can be employed as analogues. These data will be used to define a distribution, which can then be run through the USGS buoyant storage methodology to estimate the buoyant CO<sub>2</sub> storage resource of the lower Miocene shelf region of the state waters of Texas and Louisiana, and the federal waters of Texas and western Louisiana.

Blondes, M.S., Brennan, S.T., Merrill, M.D., Buursink, M.L., Warwick, P.D., Cahan, S.M., Cook, T.A., Corum, M.D., Craddock, W.H., De Vera, C.A., Drake, R.M., II, Drew, L.J., Freeman, P.A., Lohr, C.D., Olea, R.A., Roberts-Ashby, T.L., Slucher, E.R., and Varela, B.A., 2013, National assessment of geologic carbon dioxide storage resources—Methodology implementation: U.S. Geological Survey Open-File Report 2013–1055, 26 p., <http://pubs.usgs.gov/of/2013/1055/>.

BOEM, 2017, Assessment of technically and economically recoverable hydrocarbon resources of the Gulf of Mexico outer continental shelf as of January 1, 2014: U.S. Department of the Interior, Bureau of Ocean Energy Management, Gulf of Mexico OCS Region, New Orleans, OCS Report BOEM 2017–005, 50 p.

Brennan, S.T., Burruss, R.C., Merrill, M.D., Freeman, P.A., and Ruppert, L.F., 2010, A probabilistic

assessment methodology for the evaluation of geologic carbon dioxide storage: U.S. Geological Survey Open-File Report 2010–1127, 31 p., accessed, October 15, 2012, at <http://pubs.usgs.gov/of/2010/1127/>.

Carolus, M., Biglarbigi, K., Warwick, P.D., Attanasi, E.D., Freeman, P.A., and Lohr, C.D., 2018, Overview of a comprehensive resource database for the assessment of recoverable hydrocarbons produced by carbon dioxide enhanced oil recovery (ver 1.1, June 2018): U.S. Geological Survey Techniques and Methods, book 7, chap. C16, 31 p., <https://doi.org/10.3133/tm7C16>.

Garcia, O.R., 2019, Geologic characterization and modeling for quantifying CO<sub>2</sub> storage capacity of the High Island 10-L field in Texas state waters, offshore Gulf of Mexico, 2019, University of Texas at Austin, Master's thesis, 144 p.

Nehring Associates, Inc., 2019 [data current as of December 2017], The significant oil and gas fields of the United States: Colorado Springs, Colo., Nehring Associates, Inc., database available from Nehring Associates, Inc., P.O. Box 1655, Colorado Springs, CO 80901, U.S.A.

Ruiz, I., 2019, Characterization of the High Island 24L Field for Modeling and Estimating CO<sub>2</sub> Storage Capacity in the Offshore Texas State Waters, Gulf of Mexico, University of Texas at Austin, Master's thesis, 134 p.

Subtask 2.1.1.4 Fluid inclusion stratigraphy

No activity this quarter

### **Subtask 2.1.2 – Geologic Characterization of Chandeleur Sound, LA**

Using previously interpreted surfaces as inputs, a PaleoScan™ (from Eliis, Inc.) multi-surface automated surface framework was generated through the interval of interest. This included a sequence of 100 auto-generated surfaces produced from seismic peak, troughs, and seismic inflections. Figure 2.1.2.1 highlights seven representative horizons out of the 100 total horizons. The Software links coherent patches of seismic reflections stratigraphically then iteratively re-links, interpolates, and snaps to the correct seismic events to build n-number representative surfaces.

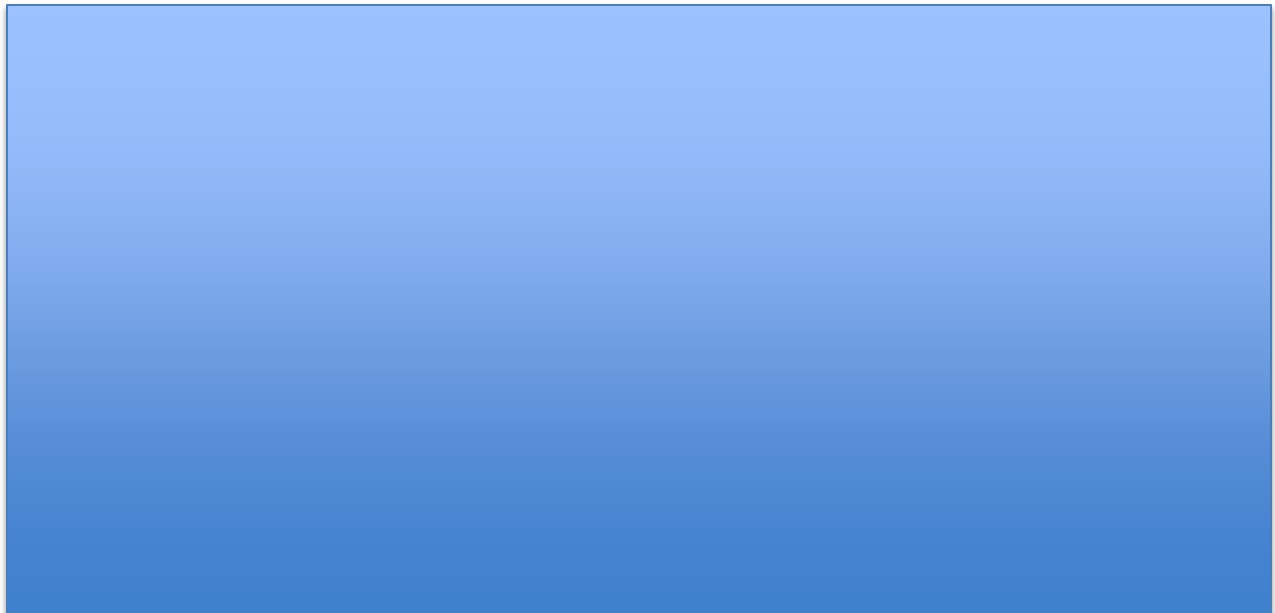


Figure 2.1.2.1 – North-south seismic section with representative auto-correlated surfaces used for preliminary attribute analysis.

***Note: Figure 2.1.2.1 proprietary data removed.***

Multiple seismic attributes were run for each of the 100 auto-generated horizons across windows adjacent to the horizons, these extractions include RMS amplitude, coherency, and spectral decomposition (at 15hz, 30hz, and 45hz). The 100 “horizon stacks” (collapsing the window of attributes into a single surface attribute) highlighted distinct stratigraphic changes in depositional environments and structural controls to be used to inform future interpretation and analysis. Specifically, spectral decomposition illuminated numerous depositional and structural features. Spectral decomposition separates seismic responses into energy components indicative of changes in density and thickness at specific frequencies. Thus, 15hz, 30hz, and 45hz frequency energy volumes were produced (30hz approximating the dominant frequency) and extractions generated with the goal of isolating genetically related or desperate geologic features.

Figure 2.1.2.2 is an example of a spectral decomposition horizon stack within the lower extent of the interval (assumed Paleogene age, magenta horizon in figure 2.1.2.1) and shows a channel incision on the shelf and numerous debris flow and fan deposits downslope from (i.e., south of) the paleo shelf edge. The seismic profiles directly above the lower slice illustrate the downlapping clinoforms advancing basinward over the incised shelf.

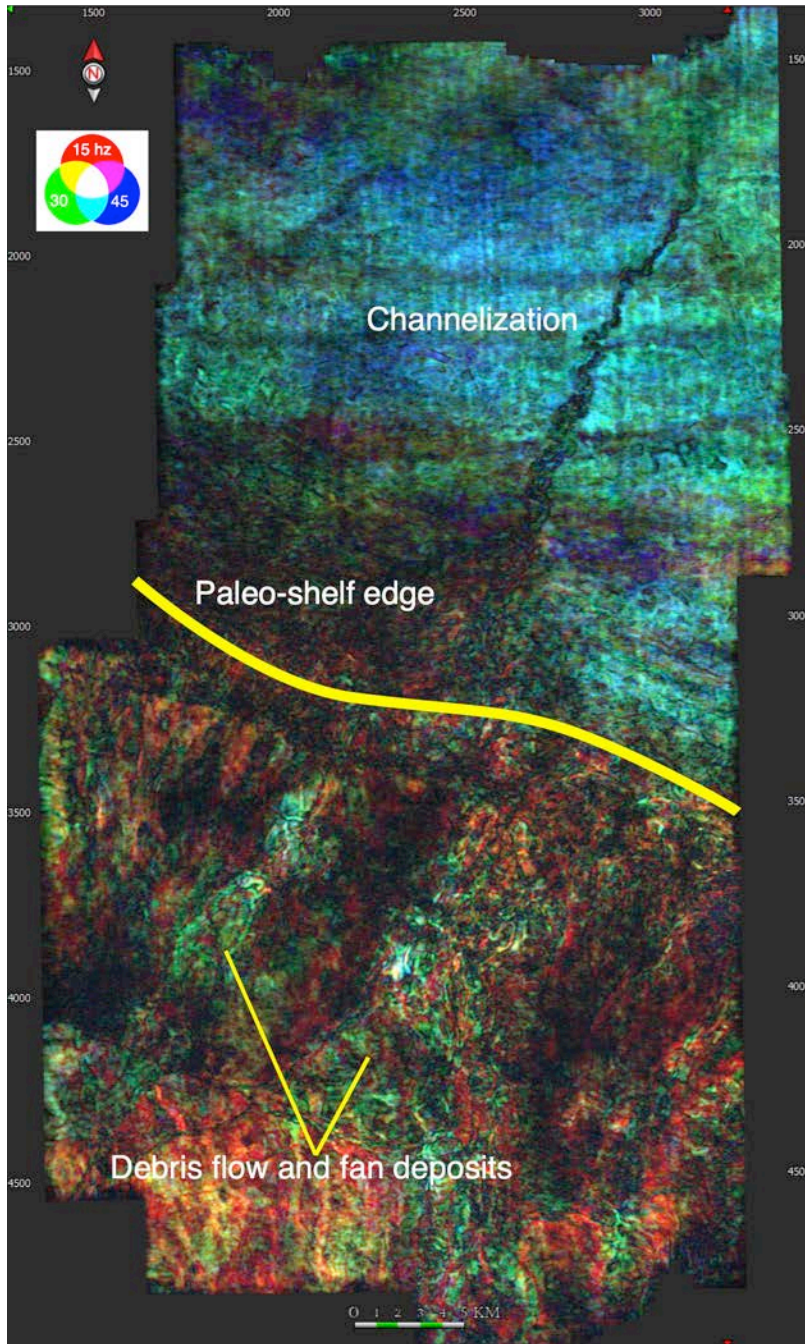


Figure 2.1.2.2 – PaleoScan™ map of lower "horizon stack" (magenta in Figure 2.1.2.1) with incised channel and slope debris flow and fan deposits noted.

Higher in the section, the “orange” horizon stack (Middle Mio, Fig. 2.1.2.3) documents an increase in abundance of slope failure (as noticed from the chaotic seismic facies), shelf edge retreat, and channel incision. Near the top of the zone of interest, the shelf edge extends distally with distinct changes in

depositional morphologies. The green “horizon stack” (near top Middle Miocene, Figure 2.1.2.4) shows various scales of fluvial channelization that indicates the transition into younger shelf deposits. These horizon stacks will be used to quality control the surface correlations as well as to inform geologic interpretations of the various units.

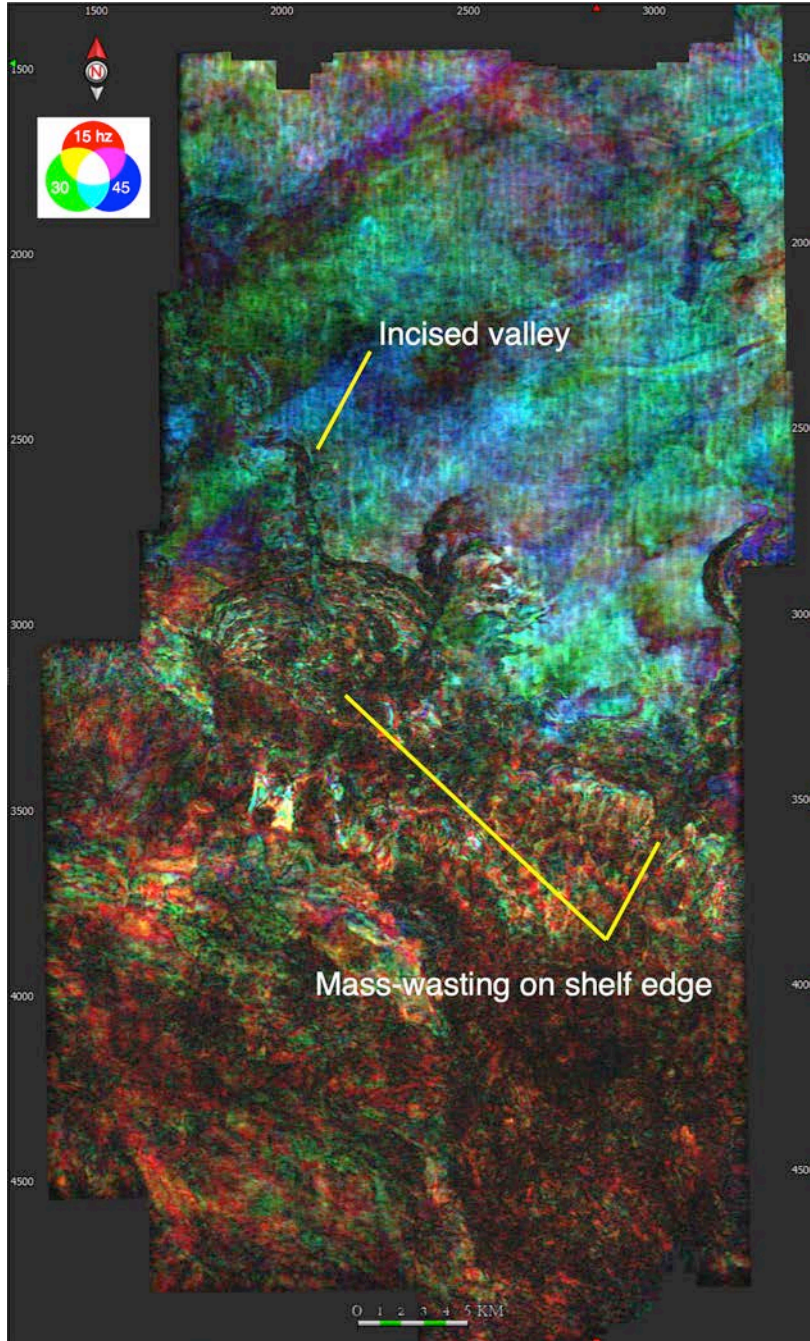


Figure 2.1.2.3 – PaleoScan™ map of middle representative horizon (orange in Figure 2.1.2.1) stack

showing an increase in shelf edge mass-wasting and channel incision.

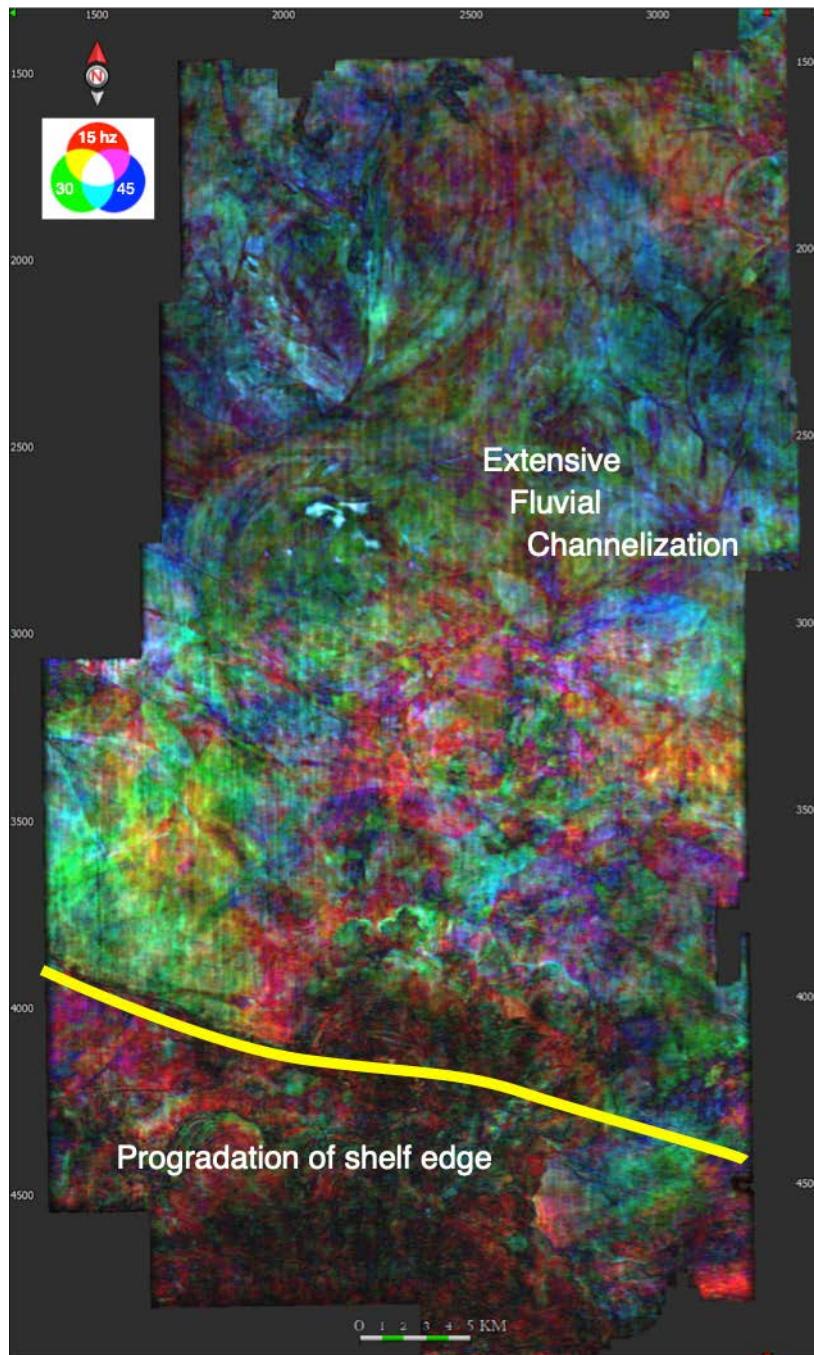


Figure 2.1.2.4 – PaleoScan™ map of upper horizon (green in Figure 2.1.2.1) denoting the transition to fluvial and shelf deposits

### **Paleoenvironmental interpretation and Update**

In the previous quarterly report, paleoenvironmental characterization found that *Amphistegina* B, a Gulf Coast benthic foraminifer that marks a sealing shale at the top of the Lower Miocene is absent in the Chandeleur Islands Survey Area. The explanation given at the time was depositional setting. Specifically, the shelf was interpreted to have been potentially sub-aerially exposed, while the slope and basin regions were too deep to accommodate this species or its deep water equivalent. Further investigation has shown that this SA was likely not sub-aerially exposed during the existence of *Amph. B*, leaving the reason for its absence to some other environmental parameter such as temperature, salinity, nutrient availability, etc. Regional paleoenvironmental maps produced by the GBDS group show that depositional environments vary within the Chandeleur SA and between the rest of western Gulf coast including the additional GoM Carb SA's (Figure 2.1.2.5). Half of the GoM Carb SA's, including Chandeleur, are situated in a shore zone (yellow), which could be associated with prohibitive environmental characteristics; however, we have not compared paleontology data from other sites to confirm this. What is unique about Chandeleur from all other sites along the western Gulf coast, however, is its situation over a facies identified as “retrogradational apron sandy” and “area of non-deposition or erosion” (Table 2.1.2.1). It is not possible at this time to be more specific about the environmental conditions that allowed or prohibited *Amph B* from living a given area because virtually nothing is known about the environmental preferences of extinct foraminifers.

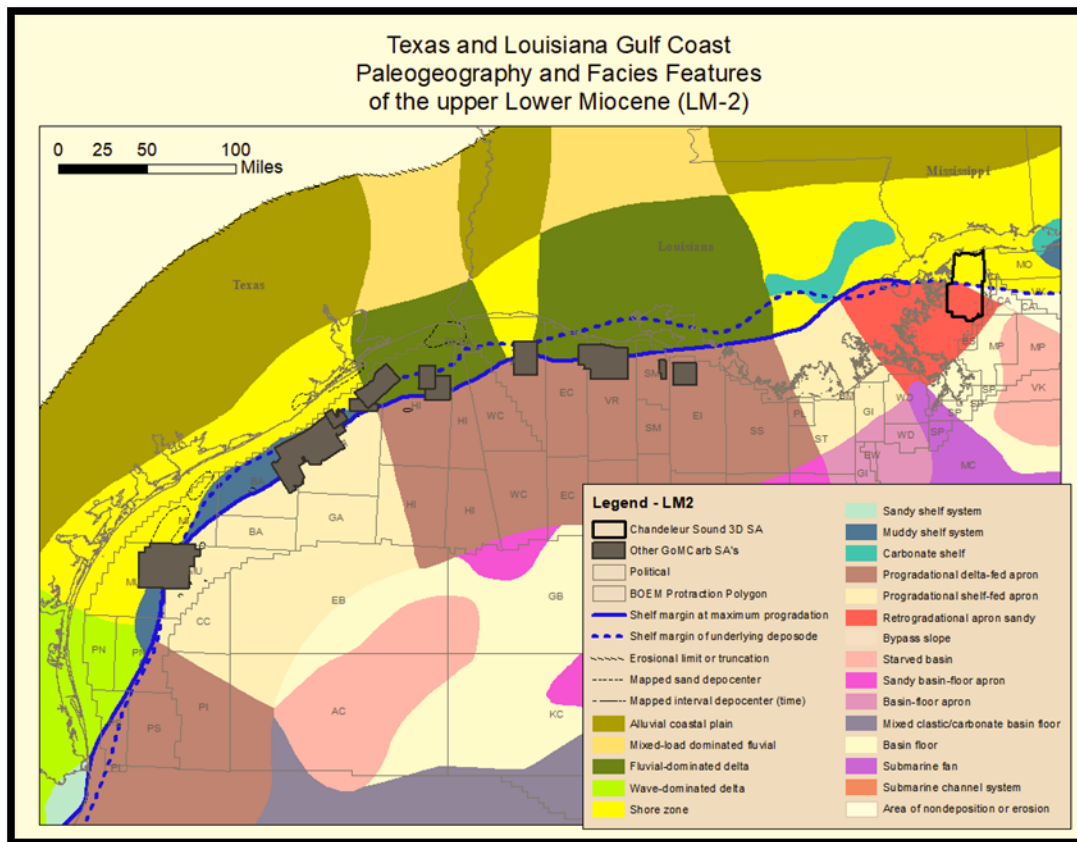


Figure 2.1.2.5 – Regional map showing GBDS Paleogeographic Facies

Table 2.1.2.1 – GBDS Facies definitions and depositional interpretations (Galloway, W.E., 2014; GBDS)

DEPOSITIONAL SYSTEM AND FACIES ASSOCIATION	LITHOFACIES DESCRIPTION	INTERPRETATION	OCCURRENCE IN BASIN
Fluvial dominated delta A. Platform delta B. Shelf-margin delta	Progradational facies succession. Heterolithic composition. Upward coarsening, lenticular, discontinuous sand bodies overlying prodelta mud. Digitate, laterally discontinuous sand bodies.	Major delta system prograding across shelf platform (A) or directly onto the continental slope (B).	Major fluvial-dominated deltas are prominent in the S. Louisiana, Houston and Macuspana depocenters.
Wave-dominated shore zone	Progradational to aggradational facies successions. Sand rich. Upward-coarsening to massive, lenticular to tabular, clean sand bodies. Transitional to sharp base; sharp top.	Constructional shorelines supplied by longshore reworking from major deltaic systems and/or reworking of non-deltaic coastal plain fringes. Includes barrier/lagoon and strandplain complexes.	Thick shore-zone systems occur in Paleogene through Middle Miocene deposodes.
Progradational delta-fed apron A. Sandy B. Muddy	Offlapping succession of sandy to muddy turbidite and debris flow deposits. Upward-shoaling succession with bathyal faunas. Discontinuous, sharp to transitionally bounded sand bodies. Abundant syndepositional faults. Capped by delta system facies.	Constructional continental margin primarily supplied by a superjacent shelf-margin delta complex.	Front major delta depocenters of N., N.W. and S.W. Gulf.
Progradational shelf-fed apron A, Sandy B. Muddy	Offlapping succession of sandy to muddy turbidite and debris flow deposits. Upward-shoaling succession with bathyal faunas. Discontinuous, sharp to transitionally bounded sand bodies. Capped by shelf system facies.	Constructional continental margin primarily supplied by a superjacent shelf.	Front major shelf and shore-zone depositional system tracts of the N.W. and N.C. Gulf Paleogene-Miocene deposodes.
Sandy retrogradational slope apron	Offlapping succession of muddy to sandy turbidite, debris flow and slump deposits. Upward-deepening and fining succession with bathyal or mixed faunas. Heterolithic interbedded, discontinuous facies association	Destructional sandy to heterolithic continental margin undergoing long-term mass wasting.	Locally prominent within OF, LM, PGa, and PAB deposodes.
A. Mud-dominated shelf B. Sandy wave-dominated shelf C. Carbonate-dominated shelf	Aggradational to progradational blankets and prisms. Sharp to transitional vertical boundaries. Transitional lateral boundaries. Massive to interstratified lithologies. Neritic faunas.	Constructional shelves marginal to major delta systems, fronting shore-zone systems, or capping transgressive coastal successions.	Carbonate shelves and ramps dominate the Florida and Yucatan margins. Relatively thick, clastic shelf systems occur in Paleogene-Miocene deposodes along N.W. and N.C. Gulf margins.

## Identification of Seal Rock (Shale)

The absence of *Amph B* does not necessarily equate to the absence of a sealing shale at the top of the Lower Miocene in Chandeleur. Some logs have been examined for the identification of a shale. Available logs useful for this task are primarily spontaneous potential (SP) and resistivity (RES). Currently, it is unclear whether a suitable shale was deposited at the top of the Lower Miocene in Chandeleur. A comprehensive query of wells penetrating through the Lower Miocene needs to be done and associated logs need to be searched for, interpreted and compared.

Aside from *Amph B*, *Textularia W* (*Textularia stapperi*) has been identified in Chandeleur, albeit few. *Tex W* marks the top of the Middle Miocene and is also a marker associated with a sealing shale. The same requirements for a thorough query of wells and logs is required for further investigation, but currently, of the few logs examined, the potential of a sealing shale at the top Middle Miocene in the Chandeleur SA is encouraging, although faulting through this interval remains a variable of concern.

## Calculating Top of Overpressure

The “supercritical cutoff” and “top of overpressure” define the interval of pressure appropriate for CO<sub>2</sub> injection. The supercritical cutoff is defined at 1000’ below seafloor, which is approximately the top of the seismic data in Chandeleur. The top of overpressure was calculated using the equation:  $P = MW / c_2$  ; where  $P$  is pressure,  $MW$  is mud weight, and  $c_2$  is the constant 9.252803 ppg/psi/ft (Burke et al., 2012). Of the 170 wells in the Chandeleur SA, 122 wells had logs, of which 12 wells reached the minimum required overpressure measurement of 0.70 psi/ft in the “hard overpressure regime” (Table 2.1.2.2). These 12 wells are all located in the southern half of the SA, beyond the shelf break. When the data were plotted and gridded in Decision Space, they were not extrapolated to cover the entire area (Figure 2.1.2.7). Soon our data will be imported to ArcGIS so that our local calculations can be easily compared to the regional pressure map produced by Burke et al. (2012) (Figure 2.1.2.6).

Table 2.1.2.2 – Wells in Chandeleur SA that reach high overpressure regime

API	Depth Driller	Mud Weight (ppg)	Pressure Gradient (psi/ft)	Latitude	Longitude	Total Depth
17727000580000	10322	13.5	0.701	29.75790146	-89.1492421	10315
17727001270000	9805	13.5	0.701	29.72360329	-89.16714333	9805
17727001720000	10000	13.4	0.696	29.70290127	-88.98893851	10000
17727001710000	10000	13.6	0.706	29.74280101	-89.05093779	10000
17727002350000	10542	13.4	0.696	29.7789016	-89.04273808	16556
17727201190000	10402	14.6	0.758	29.84547189	-88.98815162	11000
17727201220000	12300	14.5	0.753	29.93079095	-89.0539136	13458
17727201290000	15938	14.8	0.768	29.89483465	-89.12256667	19000
17727205070000	9791	13.5	0.701	29.77833112	-88.93590625	9791
17727205310000	10331	14.5	0.753	29.7652912	-88.95044064	10330
17727205330000	10022	13.6	0.706	29.75502099	-88.9193045	10560
17727205410000	10800	15	0.779	29.76890901	-89.07400782	10800

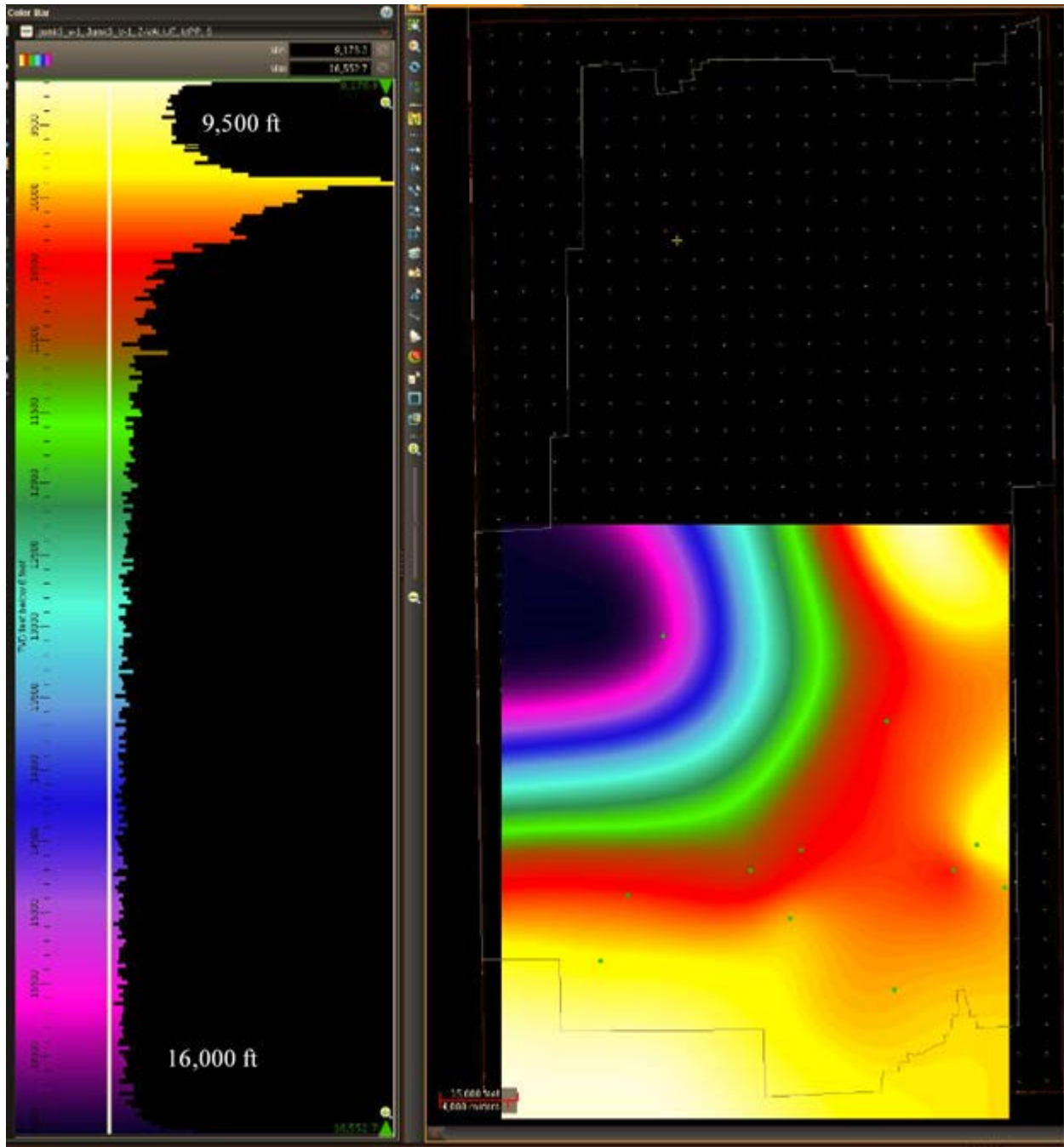


Figure 2.1.2.6 – Plan view of depth contours of the 0.70 psi/ft pressure gradient (psi/ft) in Chandeleur SA. Wells depicted by green dots.

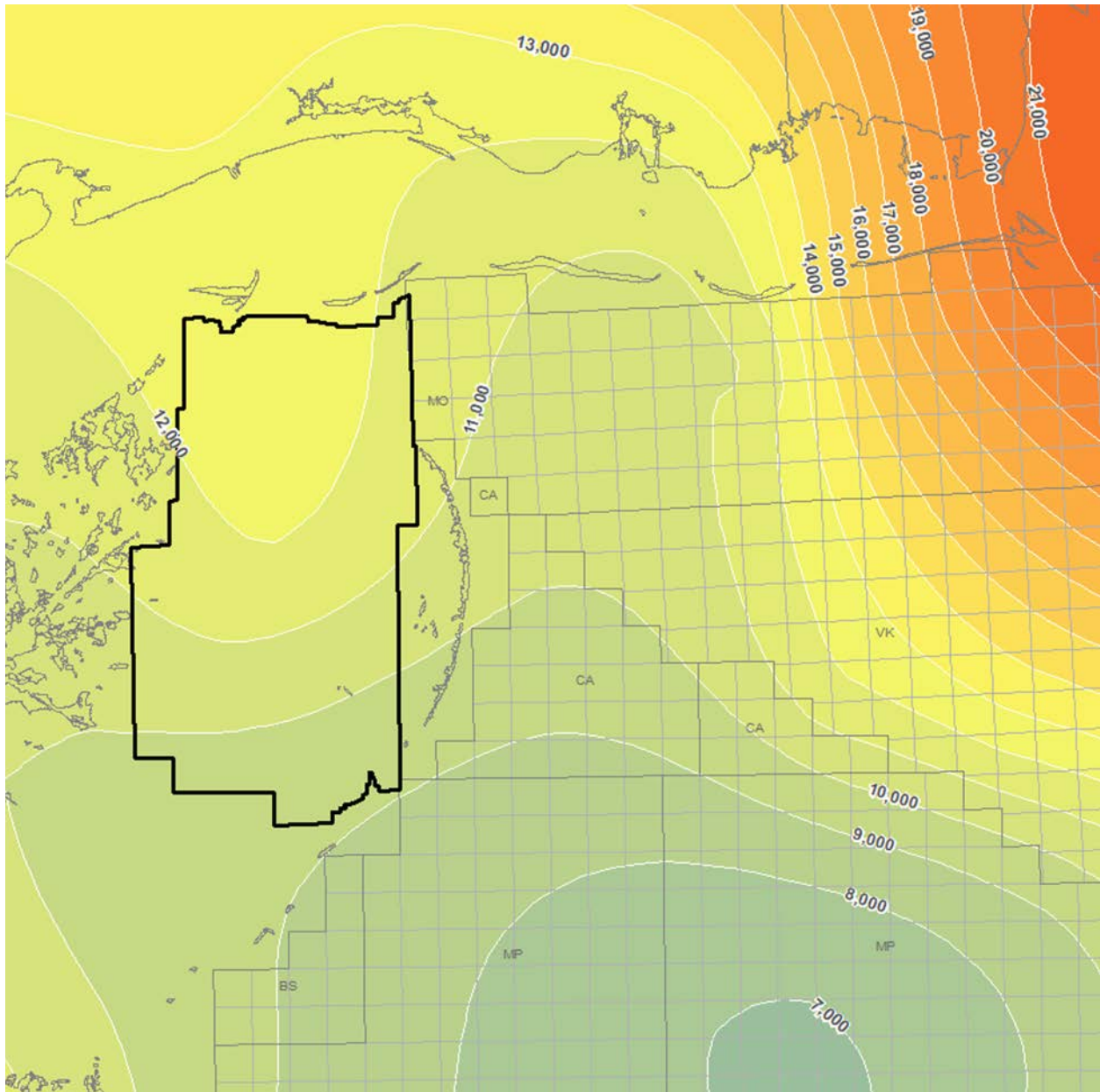


Figure 2.1.2.7 – Regional distribution of depth contours of the 0.70 psi/ft pressure gradient surface in the Chandeleur region (Burke et al., 2012)

**Reference Cited**

Burke, L.A., Kinney, S.A., Dubiel, R.F., Pitman, J.K., 2012. Regional map of the 0.70 psi/ft pressure gradient and development of the regional geopressure-gradient model for the onshore and offshore Gulf of Mexico basin, U.S.A. GCAGS Journal, vol 1, pp 97-106.

### **Subtask 2.1.3 – Geologic Characterization of High Island, TX**

See subtask 2.1.1 for overlapping activities.

### **Subtask 2.2 – Data Gap Assessment**

#### **Subtask 2.2.1: Data gap assessments will focus on regionally relevant analog settings**

No activity this quarter

### **Subtask 2.3 – Offshore and reservoir storage Enhanced Oil Recovery (EOR) Potential**

No activity this quarter

#### **Subtask 2.3.1 Texas (High Island area of Lake Jackson district) and Louisiana (Lake Charles and Lafayette districts)**

An effort to generate regional Gulf of Mexico map series was initiated in October, 2019. The map series will cover area along the Gulf of Mexico, from Port Arthur to Corpus Christi and will be divided into three geographical areas based on three 3-D seismic surveys covering an area of more than 10,000 km<sup>2</sup> (Figure 2.3.1.1). Types of maps in the map series will include structure maps (time and depth), fault maps, and seismic attribute maps. Other information related to CCS, such as oil and gas fields' outline, CO<sub>2</sub> point sources, pipelines, etc. will also be included in the maps. For each area, a regional cross-section will also be included to provide more information regarding the geology of the area. The map series will be published through BEG publications.

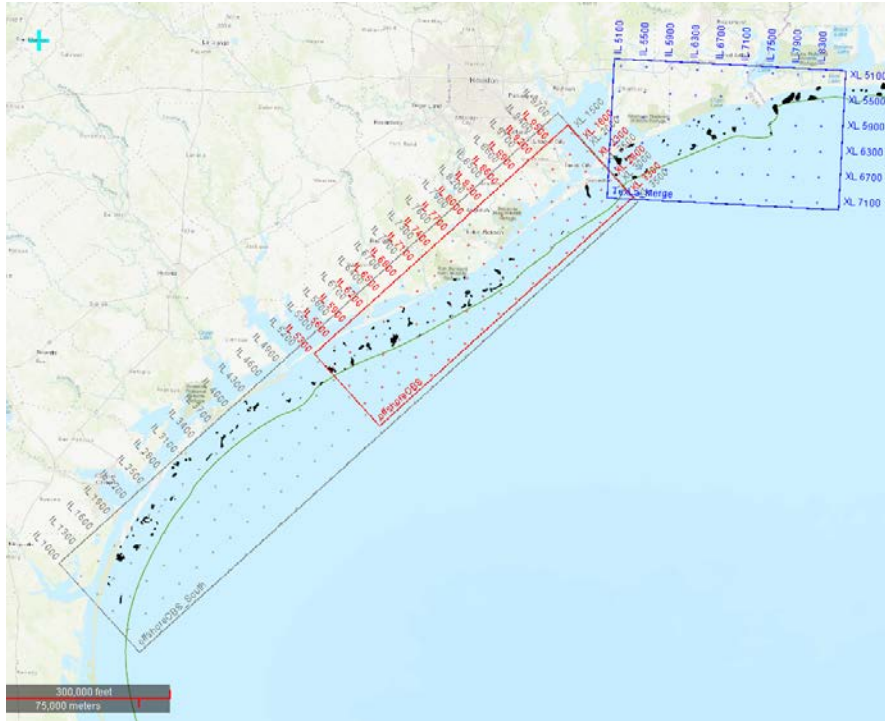


Figure 2.3.1.1 – Three 3-D seismic surveys (blue, red, and green outlines) along the Gulf of Mexico area, from Port Arthur to Corpus Christi, covering an area of more than 10,000 km<sup>2</sup> as the basis of the regional map series of the Gulf of Mexico for CCS purposes.

Seismic horizons and faults based on subsurface interpretation and mapping of the High Island 24-L site were shared with collaborators from TOTAL (Herve Gross and Antoine Mazuyer). In November 2019, a teleconference meeting was held to discuss the progress of the geo-modeling effort by TOTAL using GCCC seismic horizons and faults (Figure 2.3.1.2). The results of this geomodeling effort will be written as a manuscript to be submitted for publication with GCCC personnel.

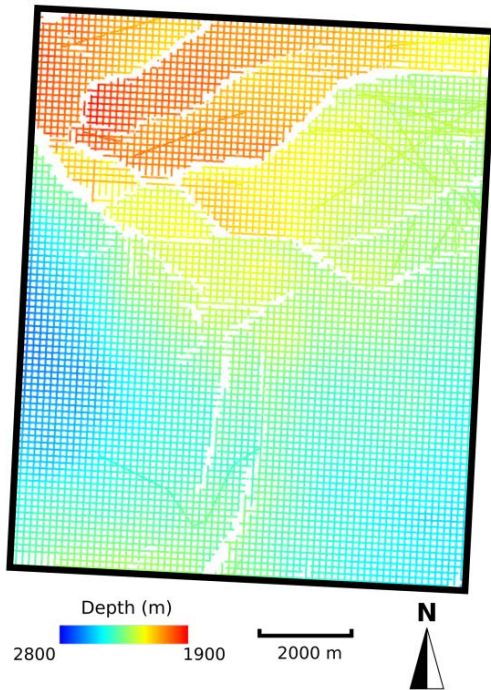


Figure 2.3.1.2. Base map of the High Island 24-L geomodel (Mazuyer et al., in preparation)

By using the regionally interpreted MFS-09 as the base of regional seal (*Amphistegina B* shale) structure maps within the three 3-D seismic survey (Figure 2.3.1.3), preliminary closures and fetch areas were identified. These structure maps were constrained by faults interpreted from the 3-D seismic volumes (Figure 2.3.1.4). Closures and fetch areas analysis were performed and generated using Permedia software. These closures and fetch areas may serve as future potential locations for CO<sub>2</sub> storage sites. Detailed closures and fetch areas distribution are available from each area (Figures 2.3.1.5, 2.3.1.6, and 2.3.1.7). There is high degree of agreement between closures resulted from this study with the distribution of existing oil and gas fields (Figure 2.3.1.8). The closures and fetch areas will be used together with regional CRS (common risk segment) maps in order to produce robust CO<sub>2</sub> storage play concepts.

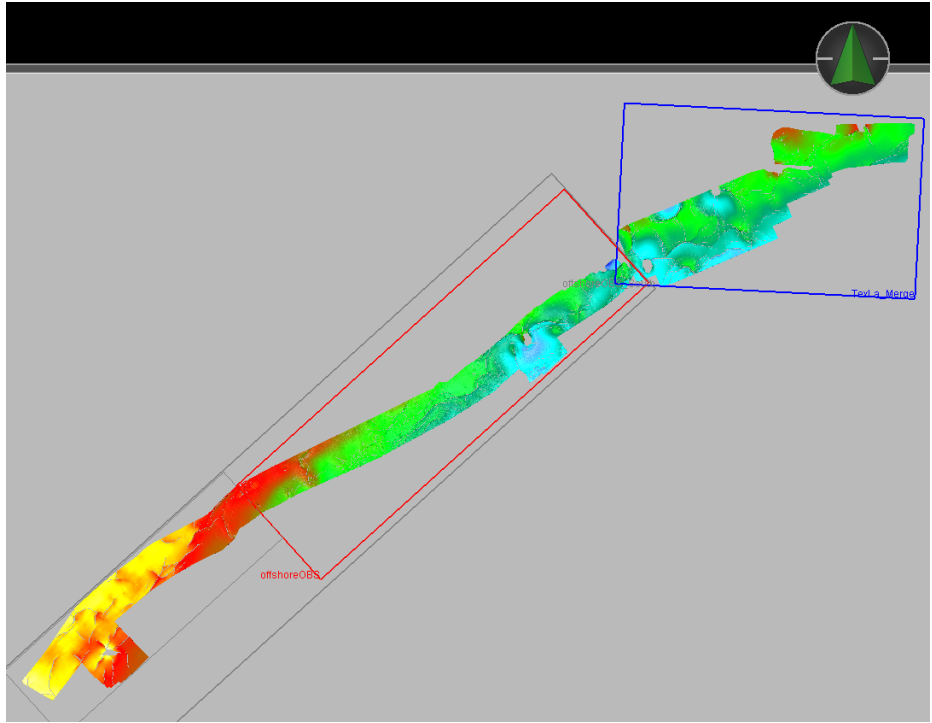


Figure 2.3.1.3. Structure maps of the MFS09 as base of regional seal (Amph-B shale) in the study area based on three 3-D seismic surveys in the Gulf of Mexico.

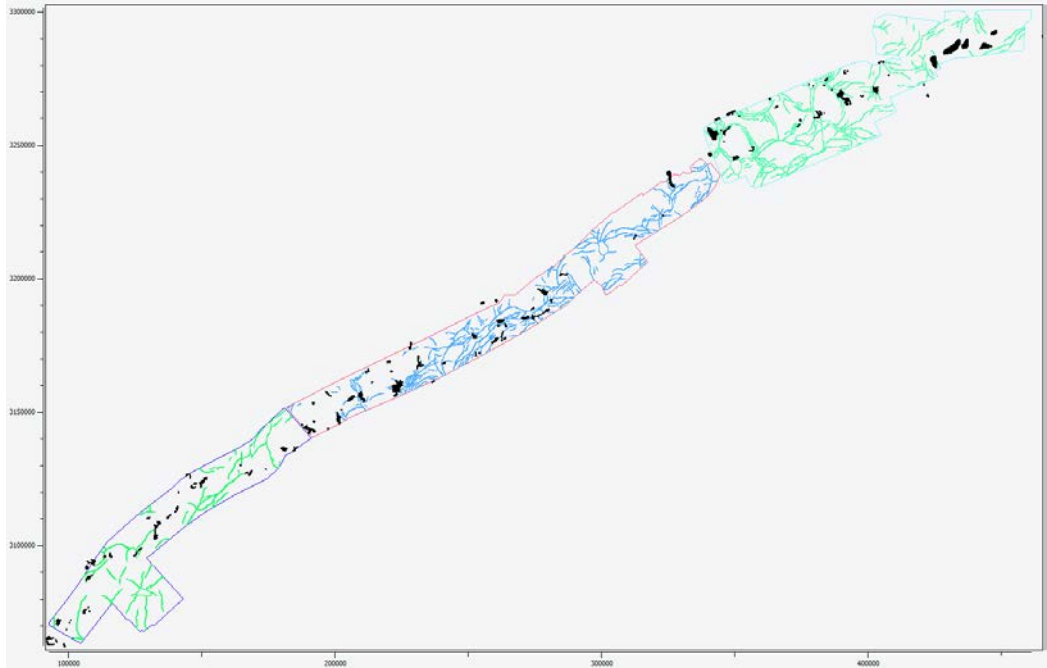


Figure 2.3.1.4. Faults distribution based on 3-D seismic interpretation (green and blue polygons) in the study area. Black-filled polygons are existing oil and gas fields outline.

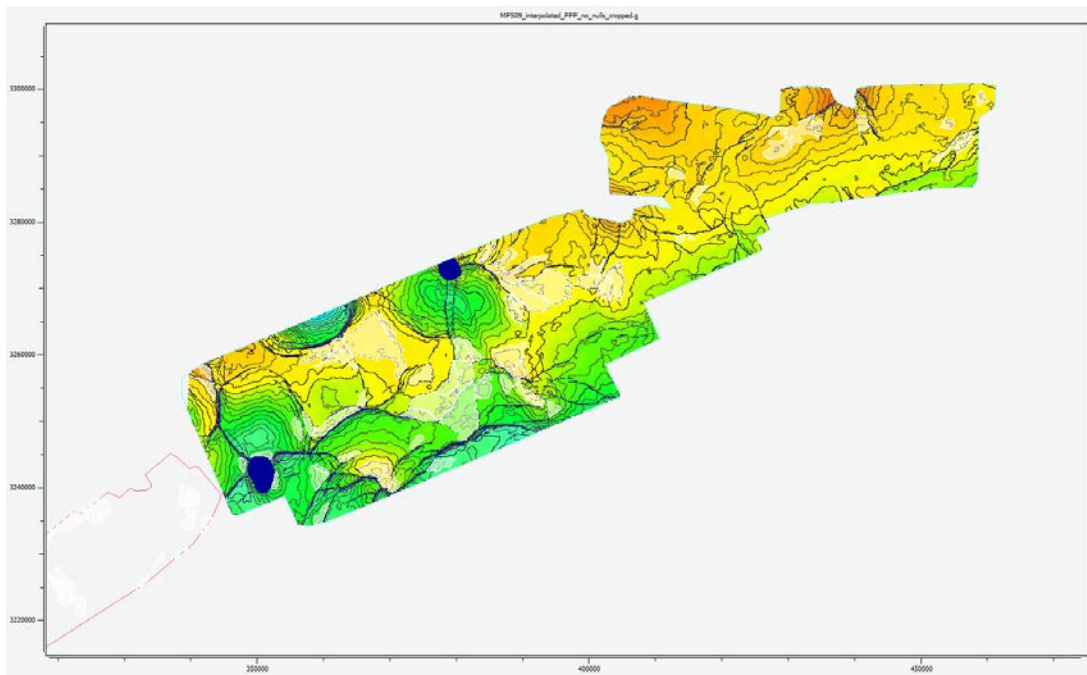


Figure 2.3.1.5 – Structural closures (white-filled polygons) identified in the northeastern area (TXLA3D seismic survey).

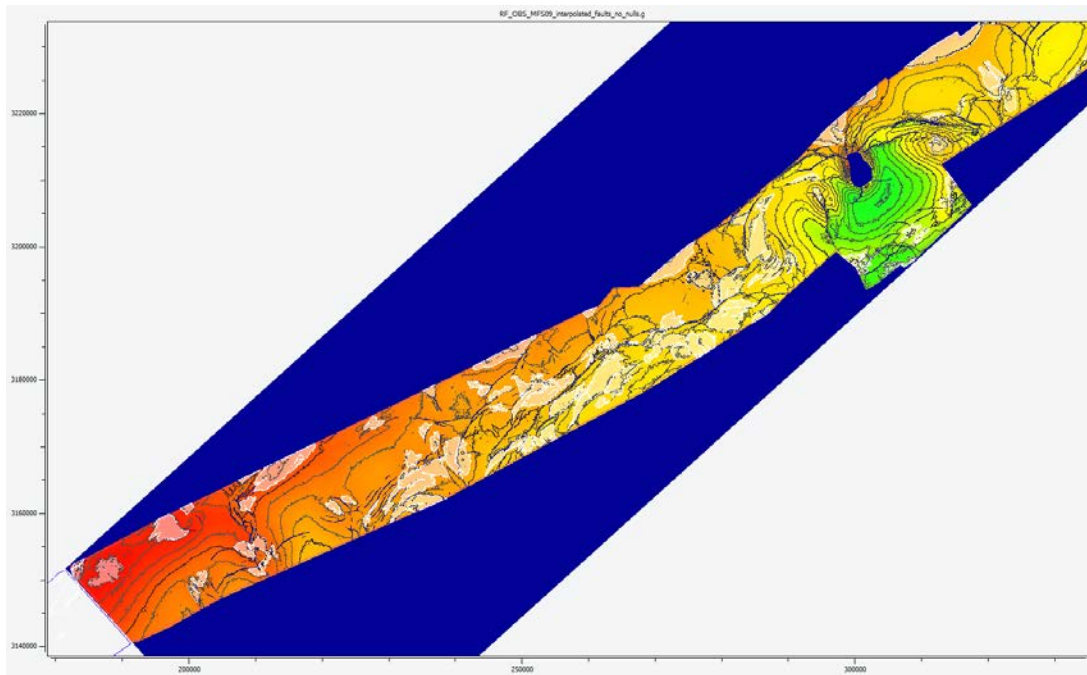


Figure 2.3.1.6 – Structural closures (white-filled polygons) identified in the central area (OBS seismic survey). Note that closures near the edge of the seismic surveys are invalid.

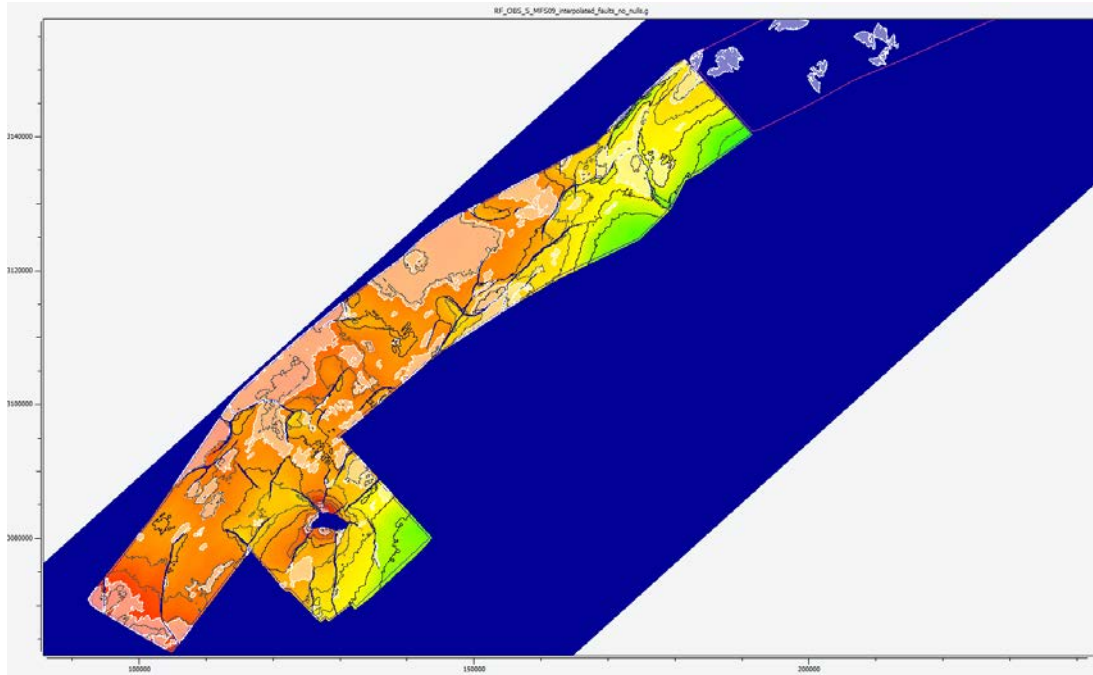


Figure 2.3.1.7 – Structural closures (white-filled polygons) identified in the southwestern area (OBS South seismic survey). Note that closures near the edge of the seismic surveys are invalid.

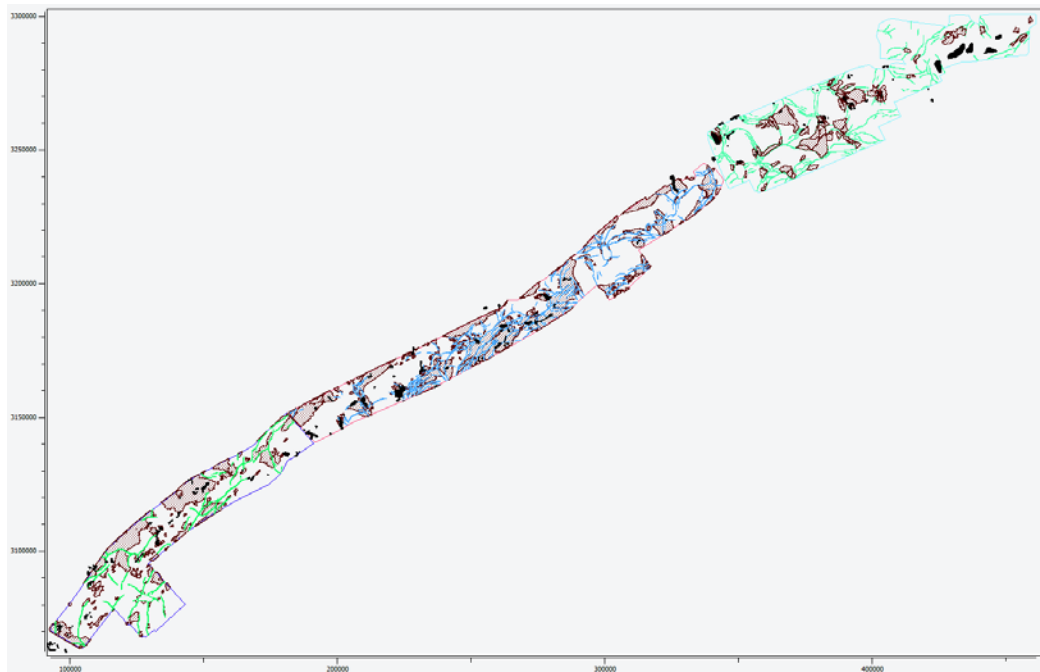


Figure 2.3.1.8 – Distribution of closures (brown-filled polygons), faults (blue and green polygons), and existing oil and gas fields (black-filled polygons) in the study area of the Gulf of Mexico. Most of the existing oil and gas fields coincide with the structural closures identified by this study.

### **Task 3.0 – Risk Assessment, Simulation and Modeling**

#### **Subtask 3.1 – Risk Assessment and Mitigation Strategies**

##### **Subtask 3.1.1 Assess the adaptation of existing tools to offshore settings**

Optimization of storage resource is a key parameter in siting and financing storage hubs. We invert petroleum exploration approaches at a geologic play level to assess subsurface risks to long-term storage, as a mechanism to lower cost and increased security. Basin-scale screening, play definition and prospect description are core tasks of petroleum exploration however and there is a well-defined suite of tools to deal with the problem. The work described here are the first steps in adapting and applying those tools to the identification of CCS sites. We focus on the U.S. Gulf of Mexico as it is a well-understood petroleum basin and the Gulf Coast is a hub of CO<sub>2</sub> emissions (Figure 3.1.1.1).

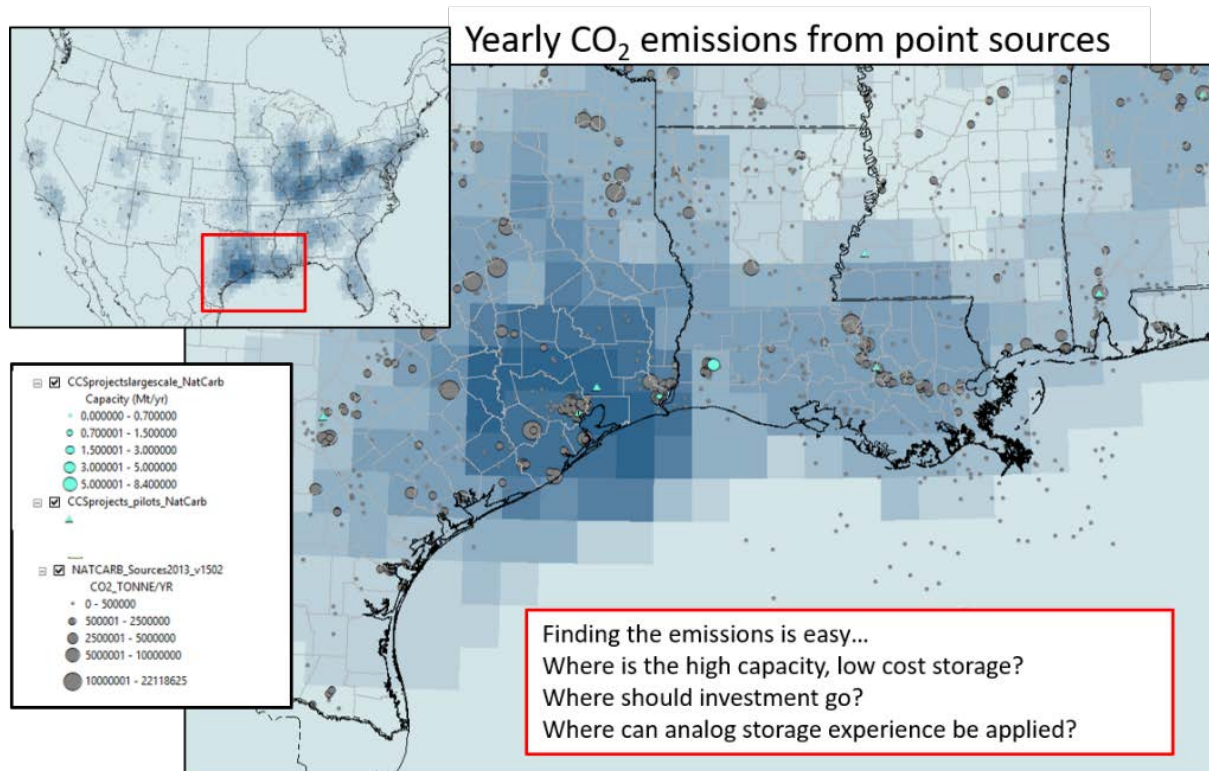


Figure 3.1.1.1: Yearly point-source CO<sub>2</sub> emissions (data: NATCARB, 2019). Individual sources are shown as grey circles (sized by emissions volume). The background colors show the total emissions within a 1.5-degree radius (darker shades for greater emissions volumes).

This is essentially a three-part approach. First, we use regional cross-sections to identify and describe potential storage plays. Second, we map the intersection of potential reservoir strata with the subsurface pressure window for CO<sub>2</sub> storage. Third, we create maps of layered subsurface elements to describe the suitability of potential sites, based on the areal quality variation of available reservoirs and seals, the locations of potential traps and CO<sub>2</sub> sources, and the distribution of surface constraints such as land usage, available infrastructure and accessibility.

With respect to the Gulf of Mexico CO<sub>2</sub> source locations, current land use, site access and the density of existing well penetrations all favor offshore storage. Accordingly, we have focused our efforts on the coastal waters of Texas and Louisiana, constructing a series of exploration-inspired cross-sections and maps that serve both to help adapt the tools of exploration for CCS and to identify and high-grade potential storage sites in coastal waters.

The depth window for CO<sub>2</sub> injection is defined by subsurface temperature and fluid pressure. Specifically, it lies between the minimum depth for supercritical CO<sub>2</sub>, which lies at roughly 1km depth and the top of hard over-pressure, which varies between 1.5 and 4km depth, based on extensive drilling data. Within this window, stratal ages vary from Early Cretaceous at the northern (onshore) basin edge to Plio-Pleistocene in the south (offshore), reflecting the long-term progradation of depositional systems toward the basin (Figure 3.1.1.2 and 3.1.1.3). For each of these stratigraphic intervals, play fairways are defined by a regional



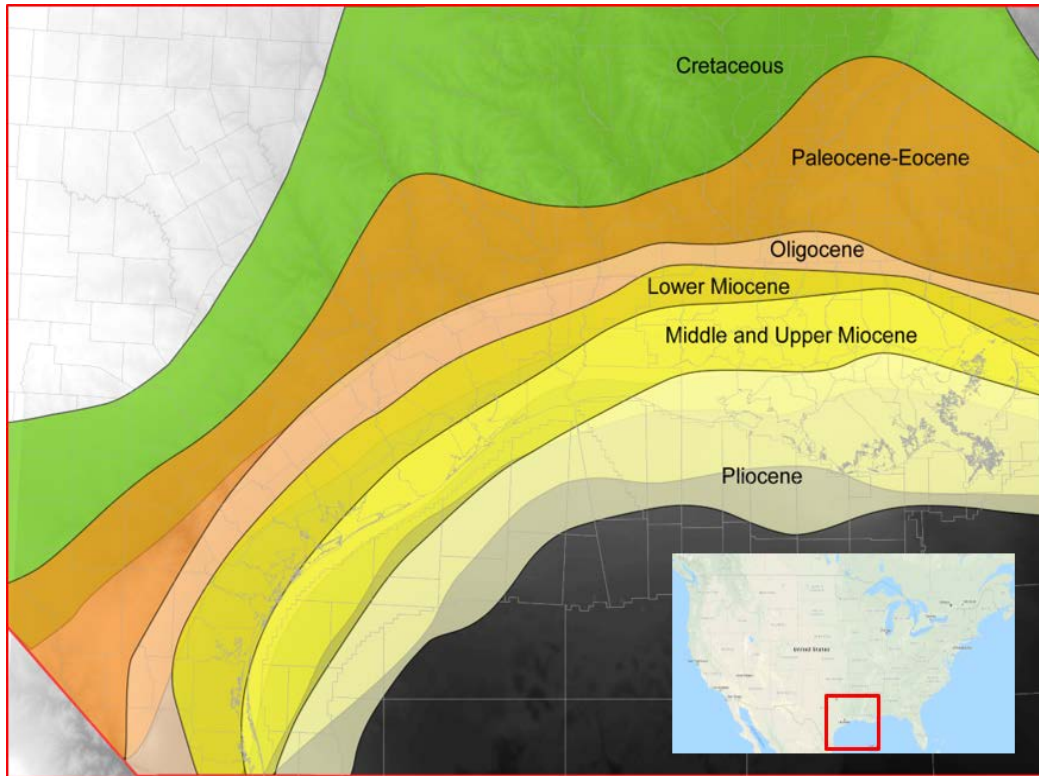


Figure 3.1.1.3: Map-view of stratal footprints within the pressure window for CO<sub>2</sub> storage. Map is based on seismic mapping of stratal ages and published maps of the top of geo-pressure.

The objective of this work is to allow efficient screening for storage sites, ensure that the focus on specific opportunities is well placed and create a framework for the intelligent application of analogs. More broadly, it creates a framework for strategic investment in storage hubs and infrastructure. The next steps are to:

- Broaden the work to Miocene reservoirs (i.e. create a view of available storage in the coastal plain and near-offshore).
- Add structural closures to the map to identify specific leads for storage sites.
- Use well characterized sites to validate and calibrate the maps, such that we can approximate the cost and capacity of available storage within each color band.

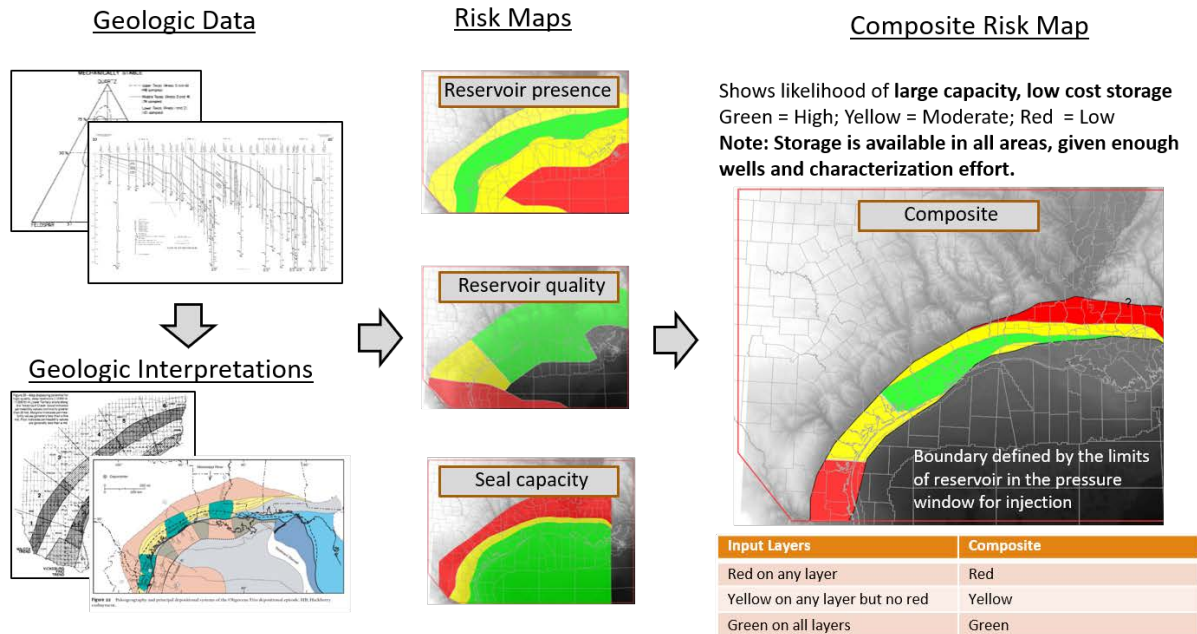


Figure 3.1.1.4: Summary of Common risk Segment (CRS) mapping. Geologic data, including well logs, seismic, outcrop descriptions and rock composition (upper right) are used to create maps of depositional environments and litho-facies (lower left). These maps are then turned into CRS maps for the key elements of the play (middle), including reservoir presence (porosity), reservoir quality (permeability) and seal capacity. The colors show the likelihood of finding each element (note that red is simply a low likelihood, not a definitive “no”). These maps are then added together according to the rules shown to create a composite risk map (right), showing the geographic chance of finding large, low-cost storage volumes. The map is clipped to the area of the formation within the pressure window for CO<sub>2</sub> storage (Figure 3.1.1.3). The example shown is for the Oligocene Frio reservoir and Anahuac seal.

**Subtask 3.1.2 Extend geomechanical assessment to additional areas of the basin**

No activity this quarter.

**Subtask 3.1.3 Dissolution and bubbling in water column**

**LBNL**

We received comments on our manuscript, “Major CO<sub>2</sub> blowouts from offshore wells are strongly attenuated in water deeper than 50 m,” that we submitted to *Greenhouse Gases: Science and Technology*. We made revisions in the organization and structure of the manuscript in response to the comments. The manuscript was accepted and finalized, and has been published online.

In addition, we presented a talk on CO<sub>2</sub> blowout attenuation in the water column at Stanford University on November 12, 2019. Comments received during and after the talk will help improve the presentation of this

material in the future.

We also presented a talk on this subject at the Fall AGU Meeting in December in San Francisco.

Finally, we wrote an abstract for a poster to be presented at the STEMM-CCS Open Science Meeting in Bergen, Norway February 11-13, 2020. The abstract was accepted and Curt Oldenburg is planning to attend and present. He will present both the CO<sub>2</sub> blowout work and a summary of the DAS monitoring work (Subtask 4.1.4) in a single poster.

#### **Subtask 3.1.4 Numerical modeling of heterogeneous reservoirs**

In the past quarter, we revised our paper on the multiscale and multipath channeling of CO<sub>2</sub> flow in the hierarchical fluvial reservoir at Cranfield, Mississippi. This paper was accepted for publication in Water Resources Research. The observed dynamic processes of CO<sub>2</sub> migration and storage are representative for any naturally heterogeneous reservoirs, like the ones to be modeled for the GoMCarb project. An invited talk on these findings was given in 2019 AGU Fall Meeting in December 13, 2019.

### **Subtask 3.2 – Geologic Modeling**

See Appendix I.

#### **Lawrence Livermore National Laboratory (LLNL)**

LLNL finished building an unstructured mesh and property model for the HI-24L site. A manuscript describing this geomodelling work (Mazuyer et al.) is nearly complete and will be submitted to IJGHGC.

We have started to run CO<sub>2</sub> injection scenarios on the model. Once we confirm the flow physics is working well, we will start adding geomechanics to inform our fault and deformation hazard assessment.

#### **Subtask 3.2.1 – Reservoir modeling**

No activity during this quarter.

#### **Subtask 3.2.2 Sub-basinal scale modeling**

No activity during this quarter.

#### **Subtask 3.2.3 History matching experiment via modeling**

No activity during this quarter.

#### **Subtask 3.2.4 Economic modeling**

No activity during this quarter.

### **TASK 4.0: Monitoring, Verification, and Assessment (MVA)**

#### **Subtask 4.1: MVA Technologies and Methodologies**

No activity during this quarter.

### Subtask 4.1.1 Geochemical Monitoring of Seabed Sediments

No activity during this quarter.

### Subtask 4.1.2 Geochemical Monitoring of Seawater Column

No activity during this quarter.

### Subtask 4.1.3 UHR3D Seismic

No activity during this quarter.

### Subtask 4.1.4 Distributed Acoustic Sensors

In the past quarter we revised, proofed, and published our paper documenting the analysis of a marine DAS experiment conducted near Moss Landing, CA in the Monterey Bay. As mentioned in the last quarterly, the DAS experiment successfully observed a sequence of mapped and unmapped faults near the seafloor using the passive noise field, mainly mode conversions generated by local earthquakes. The combination of fault identification and EQ detection suggest two modes that future seafloor DAS cables might be utilized in the context of GCS. The final publication information for the paper is:

Lindsey, N., Dawe, C.T., and **J.B. Ajo-Franklin**, “Illuminating seafloor faults and ocean dynamics with dark fiber distributed acoustic sensing”. *Science*, Vol. 366, No. 6469, pp. 1103-1107. DOI: 10.1126/science.aay5881

We are now developing a processing flow to utilize non-EQ ambient noise to image the same fault zones at finer resolutions. Figure 4.1.4.1 shows a preliminary result from this approach; the three panels correspond to different empirical Green’s functions with sources at the red line illuminating a presumed fault lineament (green line). As can be seen, energy is scattered at the fault with some hints of fault resonance. Further studies, including forward modeling to improve understanding of the response, will be carried out in the next quarter.

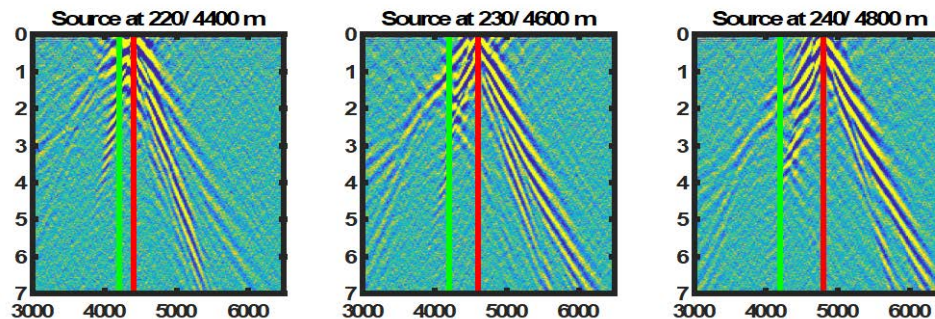


Figure 4.1.4.4 – Example of using empirical Green's functions and ambient noise to illuminate a presumed fault zone (green line). Virtual sources are shown in red. Note the scattered energy generated in the fault zone and hints of a resonance.

## Subtask 4.1.5 Pipeline MVA

### 1. High Island 10L

High Island 10L, a hydrocarbon field suitable for CO<sub>2</sub> storage, is located in the Gulf of Mexico, long-94.00 and lat 29.554, Figure 4.1.5.1.



Figure 4.1.5.1 Location of the High Island 10L [1]

Three stations in the High Island 10L region are used to collect environmental conditions. The stations are located at the Sabine Pass, Sabine Bank Channel, and the Galveston Bay Entrance, Figure 4.1.5.2.

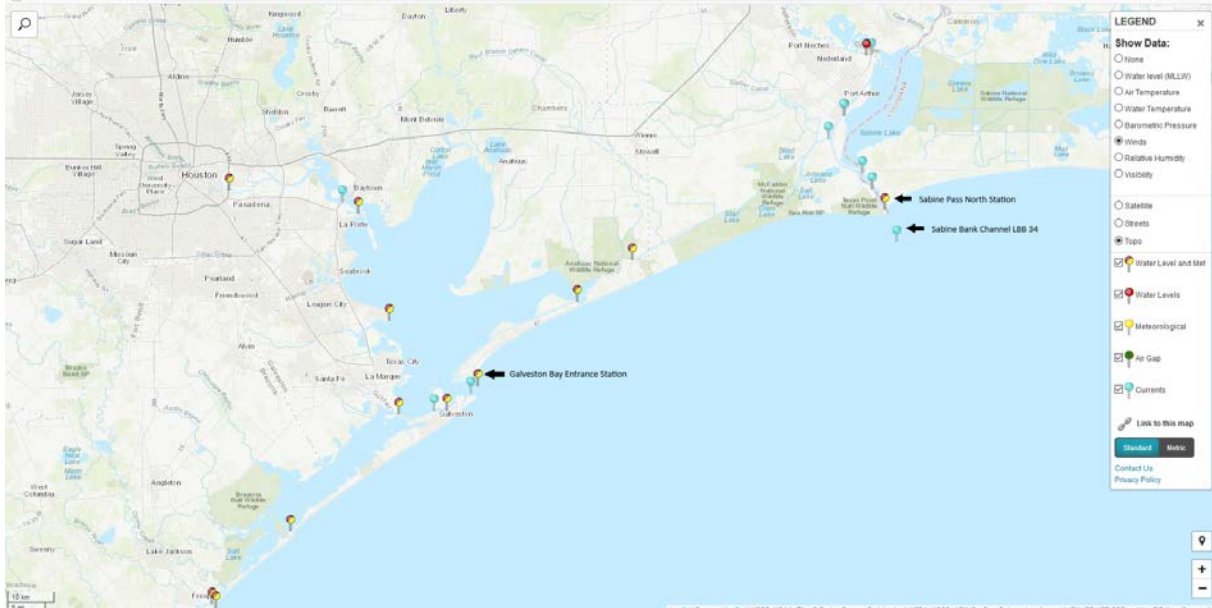


Figure 4.1.5.2 Location of Stations [2]

## 2. Environmental Data for High Island 10L

The data available from each station is summarized in Figures 4.1.5.3 and 4.1.5.4. The speed and direction of surface sea currents are monitored only in the Sabine Bank Channel LBB 34. The stations data can be exported to Excel.

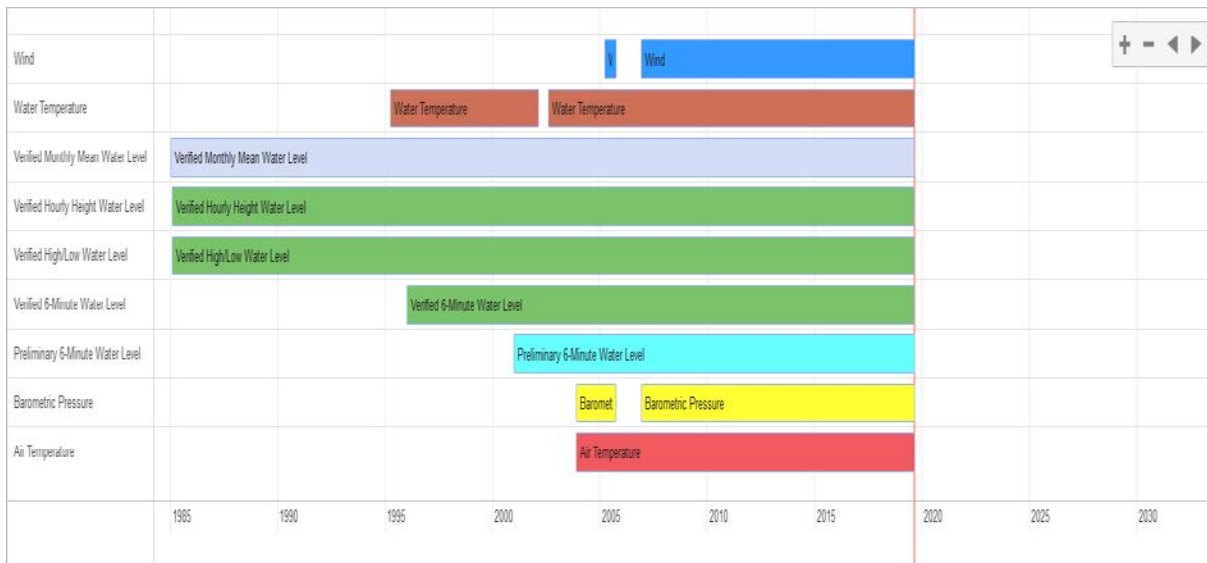


Figure 4.1.5.3 Sabine Pass North Station available data

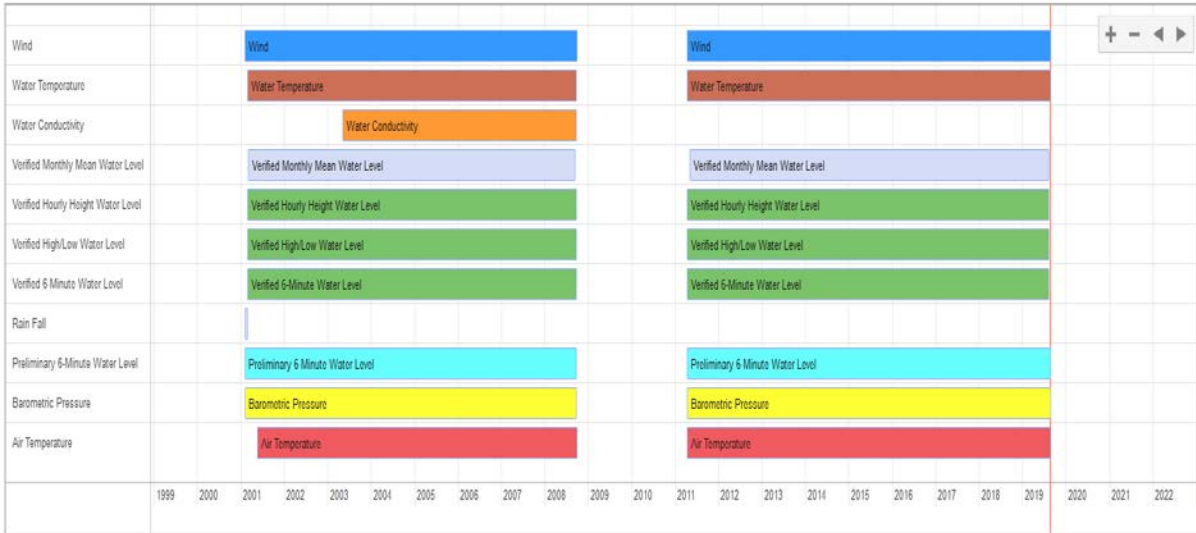


Figure 4.1.5.4 Galveston Bay Entrance Station available data

According to the Gulf of Mexico bathymetric map, (Figure 4.1.5.5) the depth around High Island 10L is 20 meters. Furthermore, the terrain at High Island 10L is essentially flat, Figure 4.1.5.6.

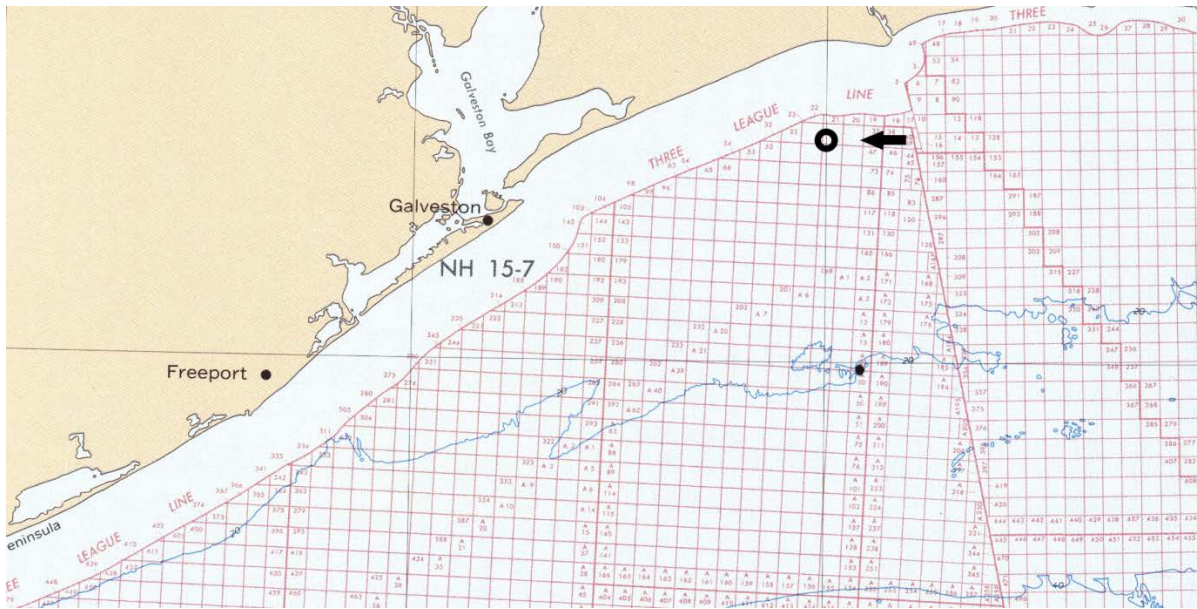


Figure 4.1.5.5 Gulf of Mexico Bathymetric Map, High Island 10L Location

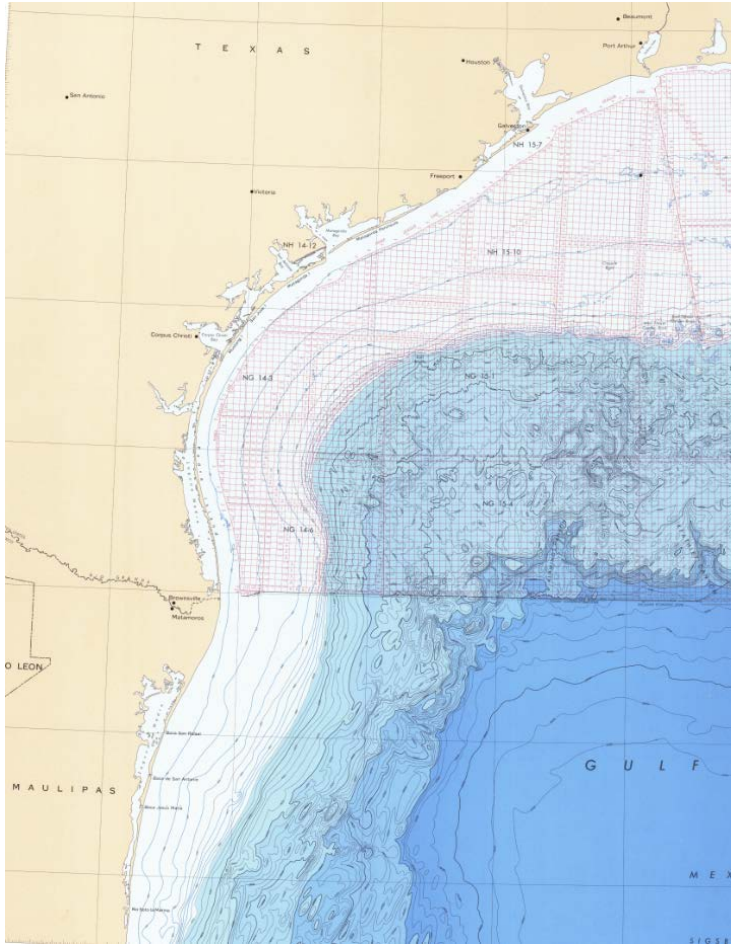


Figure 4.1.5.6 Gulf of Mexico Bathymetric Map [3]

Useful interactions with GoMCarb team members, Curtis Oldenburg at the Lawrence Berkeley National Laboratory (LBL) regarding marine environmental data near 10L and 24L lease blocks in Texas State Waters are acknowledged.

### 3. ANSYS Fluent Simulation of CO<sub>2</sub> Leakage from an High Island 10L Injection Well

The scenario of CO<sub>2</sub> leak from the High Island 10 L Injection Well was evaluated. The well information is summarized in Figure 4.1.5.7 [4].

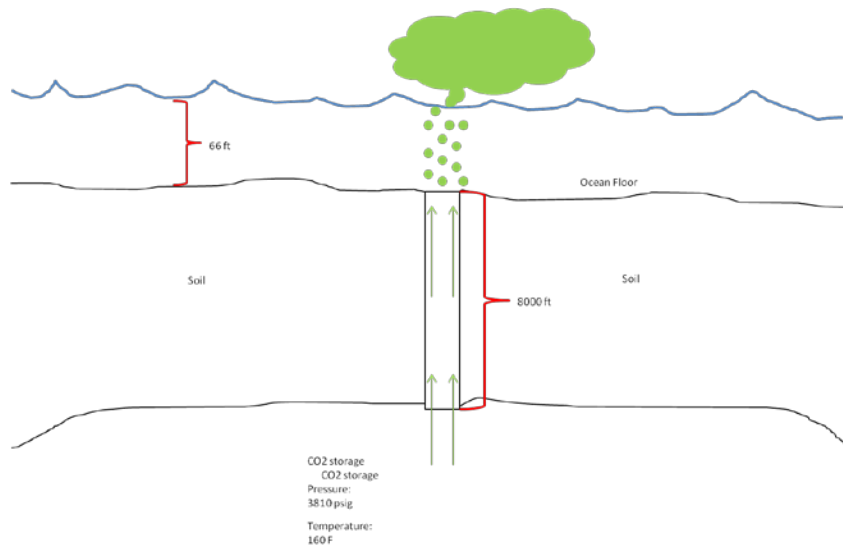


Figure 4.1.5.7 CO<sub>2</sub> Leakage from High Island 10L Injection Well

The worst case scenario for the CO<sub>2</sub> leakage was assumed, total rupture of the pipe at the top of the injection well (bottom of the ocean). The flow rate of CO<sub>2</sub> that can be injected to the well is approximately 195,000 lb/hr [5]. The pipe diameter size utilized in the study is 4". Table 4.1 was used to select the pipe size. The leakage of CO<sub>2</sub> was evaluated using the computational fluid dynamics (CFD) software Ansys Fluent.

Table 4.1.5.1 CO<sub>2</sub> Flow at Different Pipe Diameters

Pipe Size (in) sch 40	CO <sub>2</sub> Choke flow (lb/hr)	Choke Velocity (ft/s)
3.00	202000	21.43
4.00	426059	27.29
6.00	1257993	32.175
8.00	2574963	41.1
10.00	4581550	48.31

In the CFD simulation, 3 fluids were used: CO<sub>2</sub>, water and air, Figure 4.1.5.8. The mass transfer of CO<sub>2</sub> to water was included in the simulation [6]. Table 4.2 summarizes the inputs used in the simulation.

Table 4.2 ANSYS Fluent Inputs

Input	Value
Model	Multiphase Eulerian
Phases	3

Unidirectional Mass Transfer Constant (1/s)	0.005
CO2 Inlet Velocity (ft/s)	27.29
Water Inlet Velocity (ft/s)	3.28
Air Inlet Velocity (ft/s)	3.28

The results showed that most of the CO<sub>2</sub> is dissolved in water (Figure 4.1.5.9). Therefore, the aqueous CO<sub>2</sub> changes the water pH due to the possible formation of hydrogen carbonate. No dispersion of CO<sub>2</sub> in air was observed.

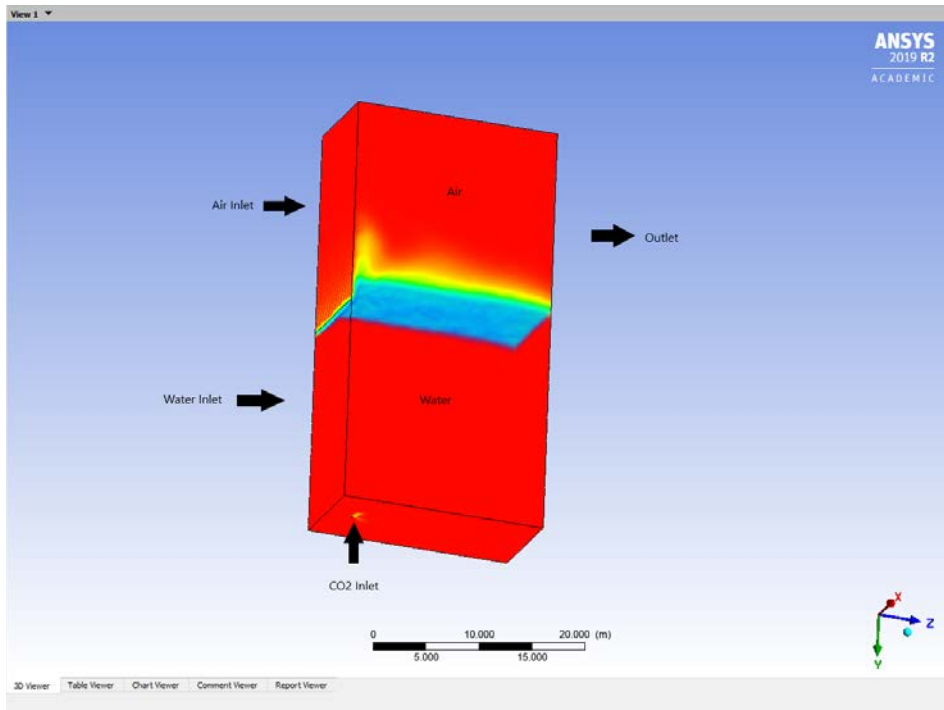


Figure 4.1.5.8 CO<sub>2</sub> Simulation Leak from High Island 10L Injection Well

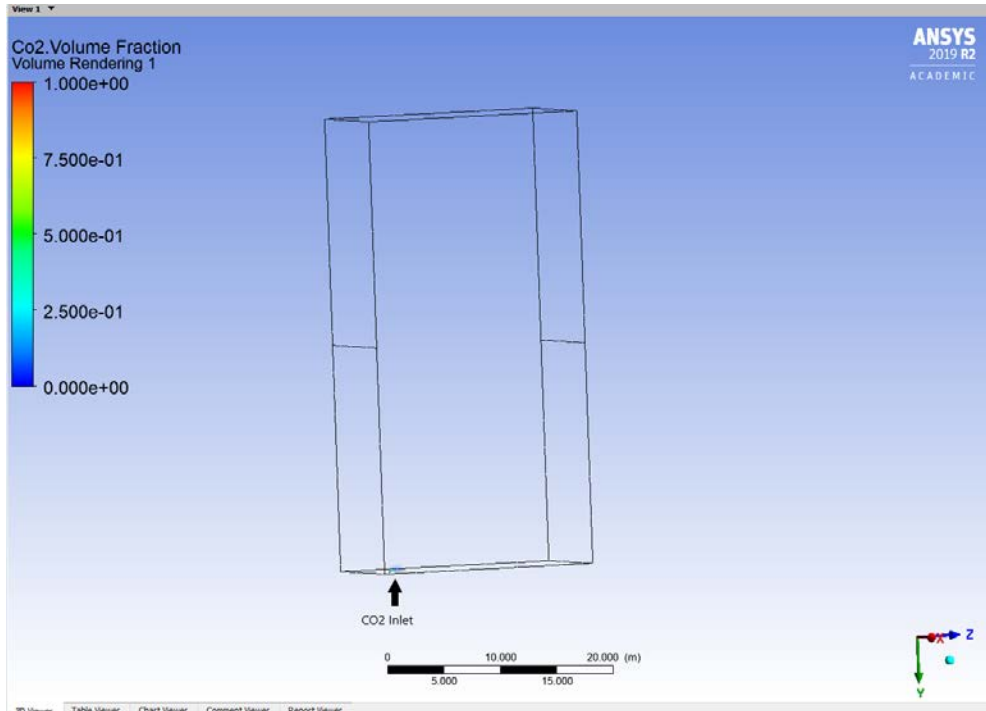


Figure 4.1.5.9 CO<sub>2</sub> Volume Fraction

#### References Cited

- [1] <http://gis.rrc.texas.gov/gisviewer/>
- [2] <https://tidesandcurrents.noaa.gov/map/index.html>
- [3] <https://maps.ngdc.noaa.gov/viewers/fishmaps/>
- [4] Fowler, Jesse, and Charles Caughey. "High Island 10-L Field." (1987): 286-290.
- [5] Fernandes, Dan, et al. "Process and carbon footprint analyses of the Allam cycle power plant integrated with an air separation unit." *Clean Technologies* 1.1 (2019): 325-340.
- [6] Al-Hindi, Mahmoud, and Fouad Azizi. "Absorption and desorption of carbon dioxide in several water types." *The Canadian Journal of Chemical Engineering* 96.1 (2018): 274-284.

### **Subtask 4.2: Plans for Testing of MVA Technologies**

#### **Subtask 4.2.1 Priority list for MVA Technologies and testing methods**

No activity during this quarter.

## **TASK 5.0: Infrastructure, Operations and Permitting**

### **Subtask 5.1: CO<sub>2</sub> Transport and Delivery**

Trimeric reviewed various literature sources and talked with industry experts about offshore infrastructure and its reuse.

A summary of findings and Trimeric's plans to incorporate this information into the infrastructure screening criteria are now summarized.

### **Project Meetings with UT BEG**

Trimeric met with UT BEG on November 18, 2019 to discuss progress to date and to receive guidance on path forward. Some of the highlights and decisions out of the meeting include the following:

- Trimeric will work with a research assistant from BEG to expand the well assessment from the initial focus on HI-10L and HI-24L to the broader GoM Carb research region
  - UT proposed downloading data in transects (narrow regions extending from shoreline) in areas of interest to expedite the data gathering/filtering process
- Trimeric will plan a kickoff meeting with Aker and UT BEG once Aker officially joins the project team. In the kickoff meeting, Trimeric will work with Aker to define Aker's scope within Task 5.
- LNG Case Study – Trimeric will further develop a case study for LNG as a CO<sub>2</sub> source for storage in the Gulf of Mexico, as several LNG facilities are starting-up in Texas and Louisiana
  - Identifies technical/economic challenges for LNG as a source
  - Is a means to engage key stakeholders in the region
  - Provides an approach to assess/identify technical challenges the CO<sub>2</sub> source may pose for transport and infrastructure.
- Trimeric will review literature to identify a range of costs associated with preparing plugged wells for re-use offshore. Trimeric's initial research on HI-10L revealed many plugged wells, so this may be a critical path item to re-using wells.
- Trimeric and UT BEG will check select wells for the presence of a caliper log – best approach to identify the quality of a cement job, another critical item for well re-use. Could serve as another screening criterion.
- For a few select high priority wells from Trimeric's screening, UT BEG would like to gather permit data and details on the well to see what kind of information is available for the next level of screening. Trimeric to work with UT BEG research assistants.
- Trimeric will pursue engaging an industry expert to gather/analyze pipeline data in the GoM. UT BEG is particularly interested if there are pipeline "deserts" in the GoM (large regions without existing pipelines).
- UT BEG will provide guidance for Trimeric on expected reservoir pressures to help

Trimeric assess acceptable pipeline pressure rating for CO<sub>2</sub> transport (Class 600 vs. Class 900 pipelines).

### **General**

As Trimeric has gathered data on existing infrastructure in the GoM and applied screening criteria in analog/proxy regions, Trimeric has developed and updated a work flow/research approach for evaluating infrastructure. The goal of this workflow is to document the high-level methodology used in the infrastructure evaluation and organize research activities moving forward (e.g., assessment of other infrastructure). The workflow developed by Trimeric is provided in Figure 5.1.1.

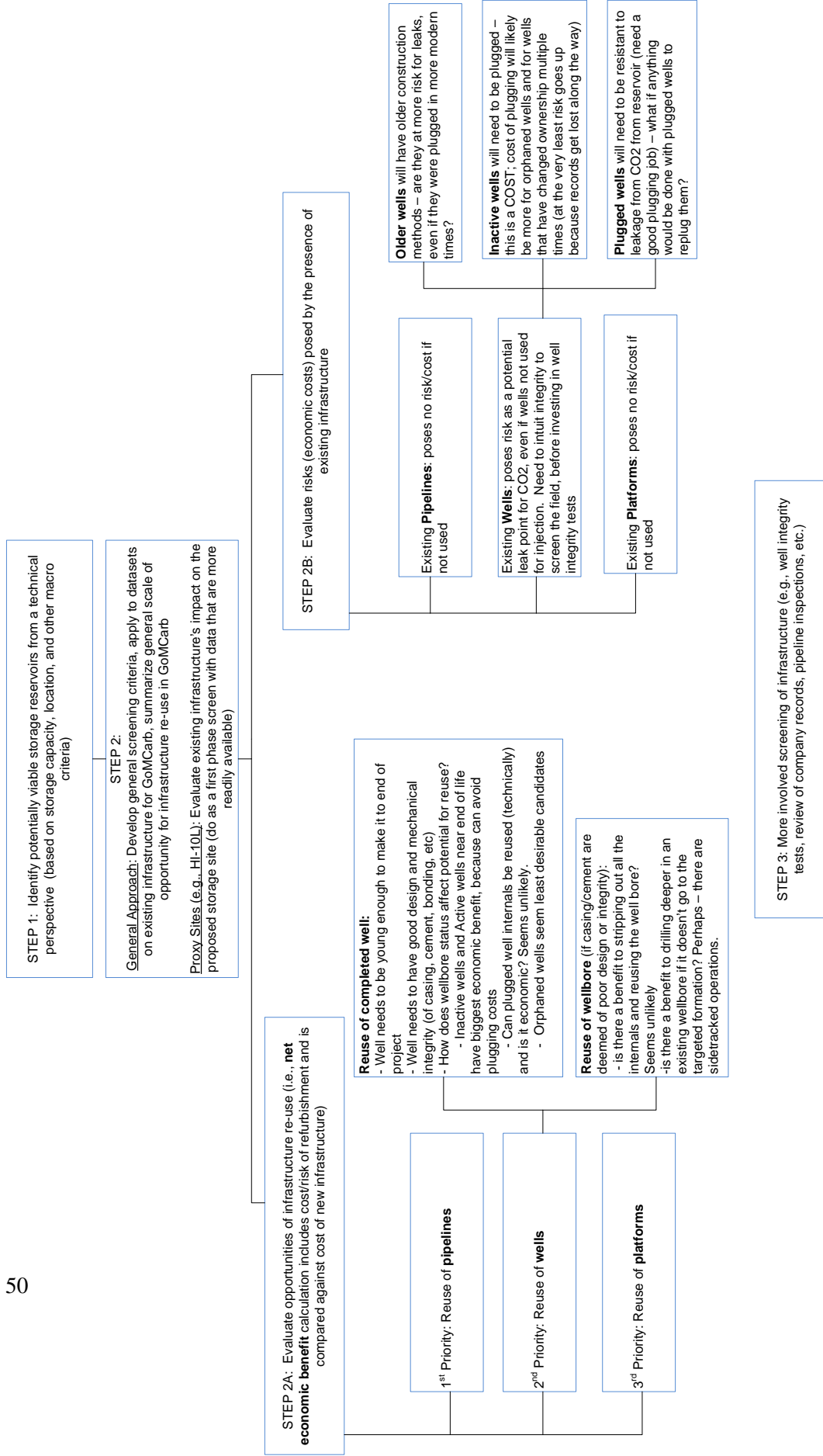


Figure 5.1.1: Infrastructure Assessment Workflow

Trimeric also initiated drafting a project report to summarize progress through the end of 2019. The purpose of the report will be to document specific results for the infrastructure task through the initial phases of the GoM Carb project and create a document that can be shared with project stakeholders to summarize the Infrastructure task methods, approach, and results. The draft report is expected to be complete in Q1 CY2020.

### **Pipelines**

- During this quarter, Trimeric interviewed an oil and gas expert with specific experience in the Gulf of Mexico, Texas, and Louisiana. The discussion spanned each infrastructure topic (see platforms and wells topics for expert input in those areas.)
  - Regarding pipelines, the industry expert believed that most large diameter pipelines would be in use.
  - Cited a project in Louisiana where a pipeline was re-used (CO<sub>2</sub> for EOR), but the pipeline quality necessitated the use of multiple booster stations to limit the maximum pressure in the pipeline during transport.
  - Expert cited familiarity with both public and private tools to evaluate existing pipeline data in Texas and Louisiana state waters as well as associated federal data. Trimeric will engage the expert for further evaluation of pipeline data in Q1 2020.

### **Platforms**

- Trimeric is working with UT BEG to identify the Texas General Land Office (GLO) as a source for platform data in Texas state waters. Trimeric prepared a platform data request list to present to GLO, as the data do not appear to be readily available in a public online database.
- The oil and gas industry expert generally commented that platforms in the GoM are well-constructed and may often have life left after end of O&G operations.

### **Wells**

- Trimeric developed a summary of the approach to well-screening developed during the assessment of the analog HI-10L and HI-24L sites and reviewed this document with UT BEG in the November 18, 2019 meeting.
- In Trimeric's interview with an oil and gas industry expert, the expert provided several important insights:
  - Plugging and Abandonment (P&A) methods are the single most important criteria for well-screening (more important than age alone as screening tool).
    - State of Louisiana allows operators to plug wells without pulling tubing strings out (they pump cement down the tubing); this makes it more difficult to go back into a well.
    - He looks at the P&A records to decide if a plug needs to be fixed (e.g., can

see if an operator didn't set the bottom cement plug properly) – need a good set of records.

- For EOR, operators often re-enter plugged wells and use them for CO<sub>2</sub> injection. They drill out the cement plugs, test the casing and then use it – this gives more confidence in the well than just relying on the plug job to hold.
- Well records can be a major problem if a well has changed hands many times (may be a screening criteria), as the risk for poor P&A practices increases.
- Expert said he would generally avoid fields with a high density of existing wells – too complicated, too much risk for communication between wells.
- Casing diameter matters – larger better, 2-3/8” tubing can go in 5-1/2” casing
- Look at the wells in the proration schedule for TXRRC – these are the wells that have not been plugged and abandoned.

#### **Subtask 5.1.2 Evaluate feasibility of subsea template in GoM**

(See Task 1, note on Aker Solutions.)

#### **Subtask 5.1.3 Preliminary Risk Assessment of CO<sub>2</sub> Release from Truck/Barge Transfer Operations**

No activity this quarter.

#### **Subtask 5.1.4 Site Leasing**

No activity this quarter.

### **Subtask 5.2: Scenario Optimization**

During the most recent quarter, Trimeric continued the development of an LNG case study to facilitate outreach in the region and develop a basis for potential scenario optimization moving forward.

In a previous report, Trimeric developed a basic block flow diagram of an LNG facility and the potential integration of CO<sub>2</sub> storage into the existing process. Figure 5.2.1 is presented here again for reference and depicts a generic LNG pre-treatment process including potential integration and benefits of CO<sub>2</sub> storage.

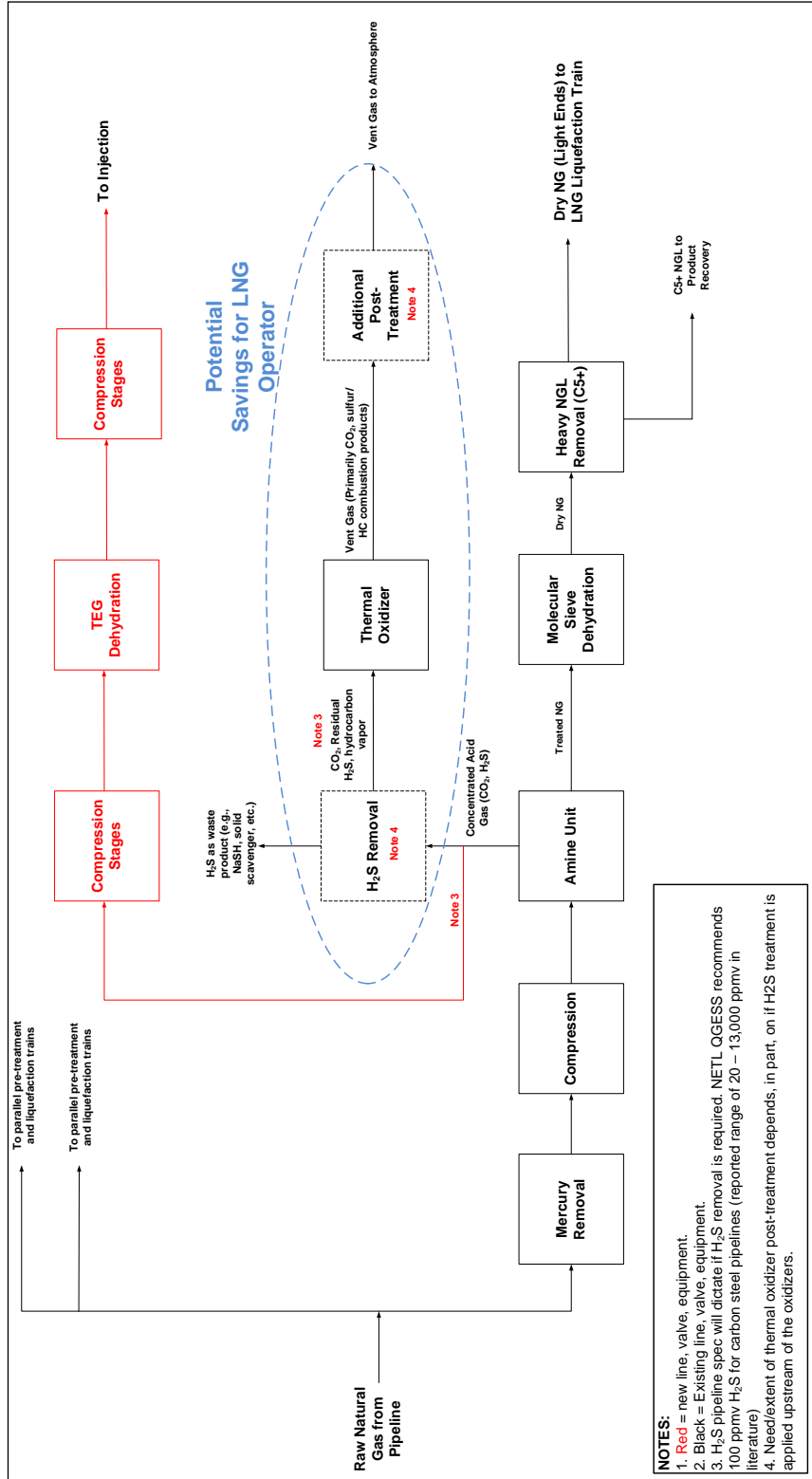


Figure 5.2.1: Overview of LNG Liquefaction Pre-Treatment Train and Potential CO<sub>2</sub> Storage Project Integration/Benefits

Using the preceding process flow diagram as a guide, Trimeric developed a design basis for a generic LNG facility for the case study and outlined the scope of a potential economic evaluation to support the case study. Tables 5.2.1 and 5.2.2 summarize the design basis and economic evaluation framework, respectively.

Table 5.2.1: CO<sub>2</sub> Capture and Transport Design Basis Summary for a Generic LNG Facility

Study Assumptions	Value	Unit	Comments
Number of LNG Trains	3		
Total Gas Flow Rate	44.5	MMscfd	Leaving Amine Unit.
CO <sub>2</sub> Concentration	96%	mol %	Leaving Amine Unit.
H <sub>2</sub> S Concentration	200	ppmv	Leaving Amine Unit.
Total CO <sub>2</sub> Flow Rate	820,109	tonnes/yr	From 3 Thermal Oxidizers.
Total CO <sub>2</sub> Flow Rate	42.7	MMscfd	From 3 Thermal Oxidizers.
Suction Pressure for Compression	14.7	psia	Atmospheric Pressure discharge from amine unit
Destination Pressure at Wellhead	1500	psia	Assumption for wellhead pressure requirement.
Pipeline Length	5	miles	Assumption
Pipeline Size	8	inches	Based on empirical correlation for CO <sub>2</sub> transport
Pressure Drop in Pipeline	58	psi	Based on empirical correlation (0.0022psi/ft)
Compressor Discharge Pressure	1558	psia	Wellhead pressure + pipeline pressure drop.

Table 5.2.2: Framework of LNG Case Study Analysis

Component	CAPEX Only (Total Installed Cost)		Notes
	New Build	Retrofit	
Compression and Dehydration	TBD	TBD	Data from Trimeric In-House Data.
Pipeline	TBD	TBD	5 miles of pipeline. Cost would currently be based on literature data/correlations.
Platform & Well	TBD	TBD	<b>Additional research required for costs.</b>
H <sub>2</sub> S/SO <sub>2</sub> Treatment Avoided Cost	TBD	OPEX Savings Only	Specific technology may vary. Cost represents a capex for a liquid scavenger scrubbing system (e.g., caustic scrubber). OPEX may be significant depending on technology. <b>NOTE: May not be able to avoid this step due to pipeline H<sub>2</sub>S spec.</b>
Thermal Oxidizer - Avoided Cost	TBD	OPEX Savings Only	Data from Trimeric In-House Data.
<b>Net Total Installed Capital Cost</b>	TBD	TBD	

The framework in Table 5.2.2 is preliminary for the purposes of planning and discussion and may be modified as the case study is pursued. However, the table does summarize the basic economic structure of a CO<sub>2</sub> capture and storage project from LNG (before accounting for benefits from 45-Q tax credits or other economic incentives). The values in the table denoted as “TBD” will be populated as part of the LNG case study evaluation.

### Lamar University

In this simulation, Aspen Plus™ was used to simulate the Steam Methane Reforming (SMR) Reaction and the Water Gas Shift (WGS) reaction. The feed to the reactor was methane and steam. Both the streams were mixed in MIX-01 and heated to ~1,300 °F before being introduced into the SMR reactor. The stream was then cooled down to 750 °F and fed to the WGS.<sup>1-3</sup> The flow rates of steam and methane were obtained from data gathered from Air Products, Inc. in connection with the two steam methane reformers at the Valero Port Arthur Refinery.<sup>4</sup> Using the all above parameters, the output stream (WGSOUTV) as shown below, consists of ~0.5 million metric tons (MMtons) per year of CO<sub>2</sub> from one SMR.

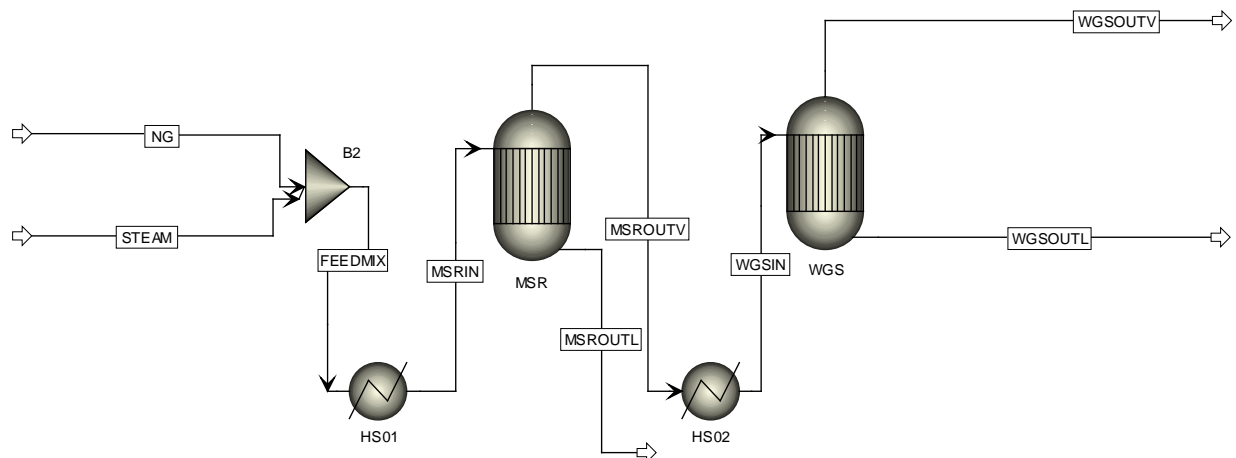


Figure 5.2.2 – Process flow diagram for Steam Methane Reforming combined with Water Gas Shift for the production of H<sub>2</sub>.

Table 5.2.3 – Estimated CO<sub>2</sub> production from a Steam Methane Reformer that delivers one-half of H<sub>2</sub> needed for a 310,000 barrel per day refinery

	Units	Input		Output
		Natural Gas	STEAM	WGSOUTV
Stream Class		CONVEN	CONVEN	CONVEN
<b>Mass Flows (total)</b>	MMtons/year	0.45	1.75	2.20
CH <sub>4</sub>	MMtons/year	0.45	0	0
H <sub>2</sub> O	MMtons/year	0	1.75	1.05
CO	MMtons/year	0	0	0.46
H <sub>2</sub>	MMtons/year	0	0	0.19
CO <sub>2</sub>	MMtons/year	0	0	0.49

### 1. Sizing and Energy Requirements for Multistage Compressors

Using the results obtained from the SMR simulation, a multistage compressor was sized for the SMR reactor, assuming that all of the CO<sub>2</sub> generated from the SMR reactor can be captured. Two compression scenarios were evaluated.

- a) 1 to 54.4 atm
- b) 1 to 154.4 atm

The compression ratio of the discharge pressure to input pressure is significantly large. Hence, it is advised to use a multi-stage compressor. A multi-stage compressor is a series of compressors with inter-stage

cooling to maintain the gas at ~100 °F at each stage.

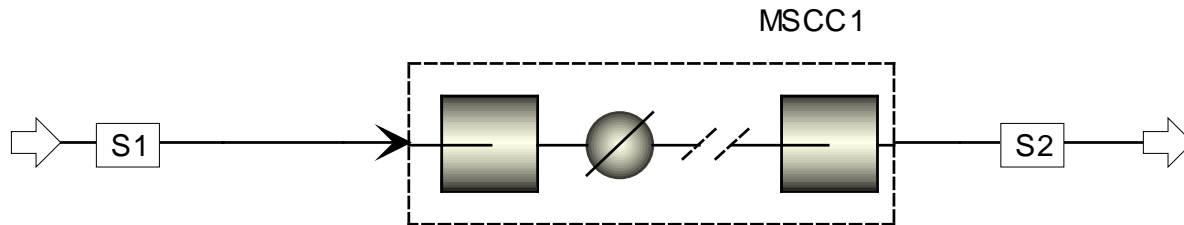


Figure 5.2.3 – Diagram of a multi-stage compressor with inter-stage cooling.

The compression ratio (CR) is a critical parameter for choosing the number of stages for a multistage compressor. The greater the compression ratio, the greater will be the power required by the compressor. An acceptable compression ratio for centrifugal compressors is 1.5 to 2. If the number of stages to be installed in series of a compressor to achieve a desired final pressure, then each compressor stage can be operated at a compression ratio according to

$$CR = (PR_T)^{\frac{1}{N}}$$

where  $PR_T$  and  $N$  are the overall compression pressure ratio and the number of compressor stages in series, respectively. Using Aspen Plus™, the energy requirements for a 6-stage compressor was obtained to compress CO<sub>2</sub> from 1 to 54 atm.

Table 5.2.4 – Overall summary and the compressor profile for the 6-stage compressor

<b>Outlet Pressure</b>	<b>atm</b>	54.4
<b>Total Work</b>	<b>Hp</b>	6,288
<b>Total Cooling Duty</b>	<b>Btu/hr</b>	-1.82 x 10 <sup>7</sup>
<b>Net Work required</b>	<b>hp</b>	628.5
<b>Net Cooling Duty</b>	<b>Btu/hr</b>	-1.82 x 10 <sup>7</sup>

Table 5.2.5 – Breakdown of compressor duties stage-by-stage (1 – 54.4 atm)

Stage	Temperature	Pressure	Pressure ratio	Brake horsepower
	F	atm		hp

1	182	1.95	1.95	1,043
2	218	3.79	1.95	1,101
3	219	7.38	1.95	1,091
4	219	14.36	1.95	1,070
5	220	27.95	1.95	1,031
6	221	54.40	1.95	952

Supercritical Compression: 1 atm to 154.4 atm

In a similar fashion, the least number of stages for supercritical compression with inter-stage cooling for the simulation was determined to be 8.

*Table 5.2.6 – Overall summary and the compressor profile for the 8-stage compressor*

<b>Outlet Pressure</b>	<b>atm</b>	154.4
<b>Total Work</b>	<b>hp</b>	7,225
<b>Total Cooling Duty</b>	<b>Btu/hr</b>	-2.91 x 10 <sup>7</sup>
<b>Net Work required</b>	<b>hp</b>	7,225
<b>Net Cooling Duty</b>	<b>Btu/hr</b>	-2.91 x 10 <sup>7</sup>

*Table 5.2.7 – Breakdown of compressor duties stage-by-stage (1 – 154.4 atm)*

Stage	Temperature	Pressure	Pressure ratio	Brake horsepower
	F	atm		hp
1	175	1.88	1.88	982
2	212	3.53	1.88	1,038
3	212	6.62	1.88	1,029
4	212	12.43	1.88	1,012
5	213	23.33	1.88	981
6	214	43.80	1.88	922
7	212	82.24	1.88	804
8	169	154.40	1.88	456

Thus far, only the CO<sub>2</sub> produced by SMR has been evaluated through process simulation. However, data obtained from the EPA – Facility Level Information on GreenHouse Gases Tool (FLIGHT) were used for the comprehensive CO<sub>2</sub> compression that is produced at refineries.<sup>5,6</sup>

Table 5.2.8 – Output of CO<sub>2</sub> emissions as reported by the GHGRP (2018).

Refinery	CO <sub>2</sub> Flow Rate (MMtons/yr)
Valero	2.1
Total Petrochemicals	5.6
Motiva	5.5
ExxonMobil	2.1

Table 5.2.9 – Summary of total work requirements for comprehensive CO<sub>2</sub> compression.

Refinery	Total Work (hp)		Total Cooling Duty (BTU/hr)	
	Subcritical Compression	Supercritical Compression	Subcritical Compression	Supercritical Compression
Valero	2.65 x 10 <sup>7</sup>	3.05 x 10 <sup>7</sup>	7.68 x 10 <sup>10</sup>	1.23 x 10 <sup>11</sup>
Total Petrochemicals	2.68 x 10 <sup>7</sup>	3.09 x 10 <sup>7</sup>	7.76 x 10 <sup>10</sup>	1.24 x 10 <sup>11</sup>
Motiva	7.08 x 10 <sup>7</sup>	8.15 x 10 <sup>7</sup>	2.05 x 10 <sup>11</sup>	3.27 x 10 <sup>11</sup>
ExxonMobil	7.12 x 10 <sup>7</sup>	8.19 x 10 <sup>7</sup>	2.06 x 10 <sup>11</sup>	3.29 x 10 <sup>11</sup>

## References

1. van Straelen, J.; Geuzebroek, F.; Goodchild, N.; Protopapas, G.; Mahony, L. CO<sub>2</sub> Capture for Refineries, a Practical Approach. *Int. J. Greenh. Gas Control* 2010, 4 (2), 316–320.
2. Xu, J.; Froment, G. F. Methane Steam Reforming, Methanation and Water-gas Shift: I. Intrinsic Kinetics. *AIChE J.* 1989, 35 (1), 88–96.
3. Amran, U. I.; Ahmad, A.; Othman, M. R. Kinetic Based Simulation of Methane Steam Reforming and Water Gas Shift for Hydrogen Production Using Aspen Plus. *Chem. Eng. Trans.* 2017, 56 (March), 1681–1686.
4. The CCS Project at Air Products Port Arthur Hydrogen Production Facility, 2018
5. Valero, Port Arthur GHGRP Data  
<https://ghgdata.epa.gov/ghgp/service/facilityDetail/2018?id=1002657&ds=E&et=&popup=true>
6. EPA - Facility Level Information on GreenHouse gases Tool (FLIGHT),  
<https://ghgdata.epa.gov/ghgp/main.do#>

### Subtask 5.2.1 Analog Site Optimization

No activity during this quarter

### Subtask 5.3: Communication

No activity during this quarter

## ***TASK 6.0: Knowledge Dissemination***

### Subtask 6.1: Stakeholder Outreach

No activity this quarter.

### Subtask 6.2: Technical Outreach

**November 9, 2019:** [GoMCarb](#) project consultant, Dr. Robert J. Finley, traveled to Austin to teach a class to GCCC first-year master's students. Finley has a long and celebrated career in geology, including decades at the Bureau of Economic Geology and the Illinois State Geological Survey. The class, titled "An Introduction to Some Concepts of Reservoir Heterogeneity," explored how different sedimentary depositional systems affect reservoir quality (and ultimately capacity) for carbon dioxide injection, providing a more nuanced view of reservoir models particularly relevant to sand intervals that are potential targets for CO<sub>2</sub> injection.

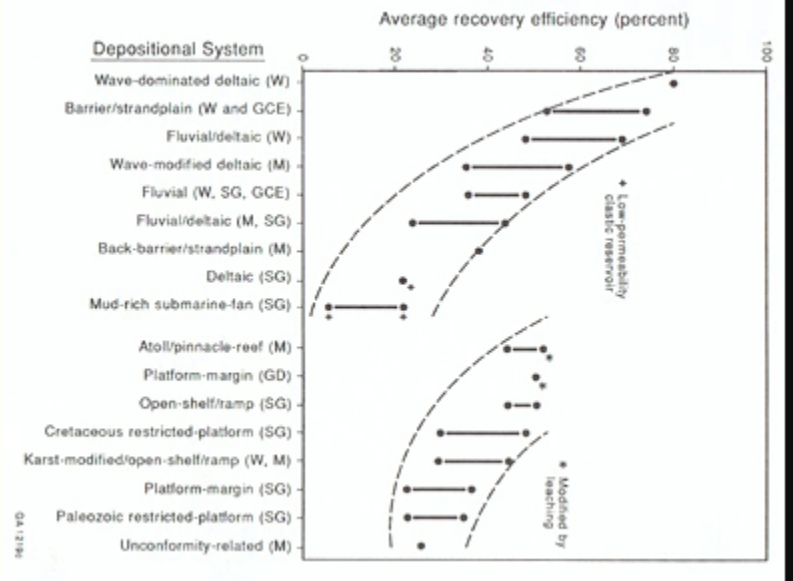


Figure 6.2.1 – (Left) Dr. Rob Finley teaching a class to GCCC students on reservoir heterogeneity and how it affects reservoir quality for CO<sub>2</sub> injection. (Right) graph from Tyler and Finley (1991) describing how depositional systems impact the average recovery efficiency in hydrocarbons; the recovery efficiency can be used as an analog for CO<sub>2</sub> injection and geo-sequestration.

### Subtask 6.3: Advisory Committee

No activity this quarter.

## PLANS FOR THE NEXT PROJECT QUARTER

In the next quarter, work will continue on:

### *Task 1*

- Prepare for annual Partnership meeting.

### *Task 2*

Subtask 2.1:

Efforts to be addressed include integrating the seismic and well-log data and identifying significant structures, particularly faults, within the study area.

### *Task 3* Risk Assessment, Simulation and Modeling

Subtask 3.1:

- Present poster at STEMM-CCS Open Science meeting in Bergen, Norway in February.
- Give talk at Texas A&M on the CO<sub>2</sub> blowout work on March 23, 2020.
- Attend the SECARB-GoMCarb joint meeting in New Orleans, March 25-27, 2020.
- Discuss water-column blowout results with Daniel Chen (Lamar U.) and look for collaborative opportunities and synergies for risk assessment.
- Check with BEG the status of the geological model with hydrofacies distributions during the SECARB-GoMCarb joint meeting.

### *Task 4* Monitoring Verification and Assessment

Results from the DAS effort will be presented as an invited talk at the upcoming SSA meeting in Albuquerque. A last component we are working on this quarter is refinement of a design for the marine CASSM source we will work on constructing in the next several quarters for seafloor/water column imaging using DAS as the detector. We anticipate performing lab tests over the summer.

### *Task 5* Infrastructure, Operations and Permitting

- Subtask 5.1: Broader data assessment of wells across the GoMCarb region.
- Subtask 5.1: Focus on first-level screening of pipeline data, specifically via engagement of an industry expert to guide the pipeline assessment activity.
- Subtask 5.2: Continued development of CO<sub>2</sub> source list along the Texas and Louisiana coast, including outreach and education of industry in the region.
- Subtask 5.2: Develop first draft of an LNG Case study for presentation to the broader project team and regional stakeholders.

### *Task 6*

- Field stakeholder survey in southeast Texas.
- Dr. Curtis Oldenburg will present a paper at the fall AGU (American Geophysical Union)

- meeting in San Francisco.
- Present topics in CCS to audiences of opportunity.

### **3. PRODUCTS**

Publications, conference papers, and presentations.

We received comments on our manuscript, “Major CO<sub>2</sub> blowouts from offshore wells are strongly attenuated in water deeper than 50 m,” that we submitted to *Greenhouse Gases: Science and Technology*. We made revisions in the organization and structure of the manuscript in response to the comments. The manuscript was accepted and finalized, and has been published online.

In addition, we presented a talk on CO<sub>2</sub> blowout attenuation in the water column at Stanford University on November 12, 2019. Comments received during and after the talk will help improve the presentation of this material in the future.

We also presented a talk on this subject at the Fall AGU Meeting in December in San Francisco.

Finally, we wrote an abstract for a poster to be presented at the STEMM-CCS Open Science Meeting in Bergen, Norway February 11-13, 2020. The abstract was accepted and Curt Oldenburg is planning to attend and present. He will present both the CO<sub>2</sub> blowout work and a summary of the DAS monitoring work (Subtask 4.1.4) in a single poster.

We revised our paper on the multiscale and multipath channeling of CO<sub>2</sub> flow in the hierarchical fluvial reservoir at Cranfield, Mississippi. This paper was accepted for publication in *Water Resources Research*. The observed dynamic processes of CO<sub>2</sub> migration and storage are representative for any naturally heterogeneous reservoirs, like the ones to be modeled for the GoMCarb project. An invited talk on these findings was given in 2019 AGU Fall Meeting in December 13, 2019.

Lindsey, N., Dawe, C.T., and **J.B. Ajo-Franklin**, “Illuminating seafloor faults and ocean dynamics with dark fiber distributed acoustic sensing”. *Science*, Vol. 366, No. 6469, pp. 1103-1107. DOI: 10.1126/science.aay5881

Websites

<http://www.beg.utexas.edu/gccc/research/gomcarb>

Technologies or techniques

None generated to date.

Inventions, patent applications, and/or licenses

None generated to date.

Other products

None to date.

#### **4. PARTICIPANTS & OTHER COLLABORATING ORGANIZATIONS**

##### **The University of Texas at Austin**

###### **Bureau of Economic Geology, GCCC (Gulf Coast Carbon Center)**

Name: Susan Hovorka, PhD

Project Role: Principal Investigator

Nearest person month worked: 1

Contribution to Project: Leadership in planning and negotiating

Name: Tip Meckel, PhD

Project Role: Co-Principal Investigator

Nearest person month worked: 1

Contribution to Project: Dr. Meckel oversaw geologic interpretation work

Name: Ramón Treviño

Project Role: Co-Principal Investigator (project manager)

Nearest person month worked: 1

Contribution to Project: Mr. Treviño provided project management and project reporting; he acted as the primary contact for the NETL project manager and contracting specialist.

Name: Michael DeAngelo

Project Role: Researcher (geophysicist seismic interpreter)

Nearest person month worked: 1

Contribution to Project: Mr. DeAngelo conducted structural interpretation of the “TexLa Merge,” “Texas OBS” and “Chandeleur Sound” regional 3D seismic datasets.

Name: Iulia Olariu, PhD

Project Role: sedimentologist

Nearest person month worked: 1

Contribution to Project: Interpretation of subsurface geology; supervisor of undergraduate research assistants.

Name: Dallas Dunlap

Project Role: seismic interpreter,

Nearest person month worked: 1

Contribution to Project: worked with Dr. Purkey-Phillips to interpret seismic in the Chandeleur Sound area.

Name: Reynaldy Fifariz, PhD

Project Role: post-doctoral fellow,

Nearest person month worked: 1

Contribution to Project: geological and seismic interpreter; liaison with Lamar U. doctoral student.

**UT Institute for Geophysics, GBDS (Gulf Basin Depositional Synthesis) Industrial Associates Program**

Name: Marcie Purkey-Phillips, PhD

Project Role: Biostratigrapher

Nearest person month worked: 1

Contribution to Project: Dr. Purkey-Phillips contributed expertise in biostratigraphy and integrated well and seismic data in the Chandeleur Sound 3D survey area.

**Fugro Marine Geoservices, Inc.**

**Lamar University**

**Louisiana Geological Survey**

**Trimeric Corp.**

**Lawrence Berkeley National Laboratory**

**Lawrence Livermore National Laboratory**

**TDI-Brooks, Inc.**

**Texas A&M University GERG (Geochemical & Environmental Research Group)**

**U.S. Geological Survey (USGS)**

**5. IMPACT:**

**6. CHANGES/PROBLEMS**

Changes in approach and reasons for change: **None**

Actual or anticipated problems or delays and actions or plans to resolve them:

A no-cost extension (NCE) of budget period 1 has been requested in order to accomplish the acquisition of a high-resolution 3D seismic survey, which will not occur until late 2020.

Changes that have a significant impact on expenditures: **None**

Change of primary performance site location from that originally proposed: **None**.

### **7. SPECIAL REPORTING REQUIREMENTS**

Respond to any special reporting requirements specified in the award terms and conditions, as well as any award specific requirements. **None**

### **References Cited**

- Burke, L. A., Kinney, S. A., Dubiel, R. F., & Pitman, J. K. (2012). Regional Map of the 0.70 PSI/FT Pressure Gradient and Development of the Regional Geopressure-Grandient Model for the Onshore and Offshore Gulf of Mexico Basin, U.S.A. . *GCAGS Journal*, 1 97-106.
- Pitman, J. K. (2011). Reservoirs and petroleum systems of the Gulf Coast: Depth to top overpressure [map]. In <http://www.datapages.com/Services/GISUDRIL/OpenFiles/ReservoirsandPetroleumSystemsoftheGulfCoast.aspx>: U.S. Geological Survey.

## Appendix I

### Compressibility Effects on Viscous Instability Under Sealing and Partially Sealing Boundaries Part I: Tracer Flow

**Compressibility Effects On Viscous Instability Under  
Sealing and Partially Sealing Boundaries  
Part I: Tracer Flow**

By

Aura N. Araque-Martinez and Larry W. Lake

The University of Texas at Austin

December 15, 2019

# Table of Contents

<b>Summary .....</b>	<b>1</b>
<b>Introduction.....</b>	<b>2</b>
<b>Basic Equations.....</b>	<b>5</b>
<b>Results.....</b>	<b>10</b>
Analytic Solutions.....	10
Comparison Against Numerical Simulation.....	12
Instability Analysis - Tracer Flow .....	15
<b>Conclusions .....</b>	<b>17</b>
<b>Acknowledgements .....</b>	<b>17</b>
<b>References .....</b>	<b>17</b>
<b>Nomenclature.....</b>	<b>19</b>
<b>Appendix A: Analytical Solution for Large and Constant Compressibility – Tracer Flow.....</b>	<b>20</b>
<b>Appendix B: Front Position Calculation .....</b>	<b>26</b>

---

# Tables and Figures

## Tables

Table 1:	Stabilized pressure solutions for zero compressibility and different outer boundary conditions.....	10
Table 2:	Stabilized pressure solutions for very small compressibility and different outer boundary conditions .....	11
Table 3:	Stabilized pressure solutions for small compressibility and different outer boundary conditions.....	11
Table 4:	Stabilized pressure solutions for large compressibility and different outer boundary conditions.....	12

## Figures

Figure 1:	Schematic of a 1-D linear displacement showing the perturbation,.....	5
Figure 2:	Schematic of flow regimes for constant flow rate (adapted from Walsh and Lake, 2003).....	6
Figure 3:	Comparison of analytical and simulated pressure profiles for single fluid under different compressibility ( $f=1$ , steady-state flow transparent outer boundary).....	13
Figure 4:	Analytical and Simulation rate (reservoir conditions) results comparison for single fluid under different compressibility ( $f=1$ , steady-state flow). .....	13
Figure 5:	Comparison of analytical and simulated pressure profiles for single fluid under different compressibility ( $f=0.5$ , partially sealed outer boundary). .....	14
Figure 6:	Comparison of analytical and simulation rate (reservoir volume) results comparison for single fluid under different compressibility ( $f=0.5$ , partially sealed outer boundary). ..	14
Figure 7:	Comparison of analytical and simulation pressure profiles for single fluid under different compressibility ( $f=0$ , semisteady-state flow, sealed outer boundary). .....	14
Figure 8:	Comparison of analytical and simulated rates (reservoir conditions) for single fluid under different compressibility ( $f=0$ , semisteady-state flow, sealed outer boundary). .....	15
Figure 9:	Compressibility effect on front position history under stabilized steady-state flow ( $f=1$ ) ..	15
Figure 10:	Compressibility effect on front position history under stabilized unsteady-state flow ( $f=0$ ) .....	16
Figure 11:	Boundary effect on front position under stabilized flow for small and constant compressibility fluid .....	16
Figure 12:	Boundary effect on front position under stabilized flow for large and constant compressibility fluid .....	16

---

## Summary

The knowledge of the effects of instability and heterogeneity on displacements, primarily enhanced oil recovery and carbon dioxide storage, are well known though they remain difficult to predict. The usual recourse to modeling these effects is through numerical simulation. Simulation remains the gold standard for prediction; however, its results lack generality, being case specific. There are also several analytic models for displacements that are usually more informative than simulation results. However, these methods apply to steady-state, incompressible flow. Combining the effects of instability with compressible flow is the objective of this work.

Part I, presented here, deals entirely with tracer flow. Part II will cover displacements when the two fluids, displacing and displaced, have different properties.

Carbon dioxide injection for storage uses compressible fluids, and, in the absence of producers, will not approach steady-state flow (Yun et al., 2017). Consequently, is unlikely that storage will be in reservoirs of open boundaries. Flow of compressible fluid necessitates the use of closed or partially sealed boundaries, a factor that is consistent with compressible flow. It is the object of this work to investigate the effect of how partially sealed boundaries and compressible fluids affects the displacement behavior in CO<sub>2</sub> storage.

Results show that adding compressibility always makes displacements more unstable for steady-state flows. For semi-steady flow (sealed outer boundary) displacements will become more stable as a front approaches the outer boundary.

---

## Introduction

Front displacement viscous/gravity stability, mainly related to enhanced oil recovery (EOR), has been long studied, but still remains difficult to evaluate. In fact, this problem has been studied since the mid-50's and its prediction mostly relies on numerical simulation techniques and laboratory scale experiments.

In 1952, Hill studied channeling in packed columns during the displacement of sugar liquors by water. He defined a critical velocity based on fluid viscosity and fluid density differences, after which the displacement becomes unstable. Hill's work is evidently the first on this subject (Homsy, 1978)

The well-known criterion for the onset of viscous fingering is based on the so-called Saffman-Taylor (ST) instability work (Saffman and Taylor, 1958). The criterion involves incompressible fluids under steady-state flow and states that a steady-state flow will exhibit front displacement instability (an arbitrary perturbation in the front will grow) if the driving fluid is less viscous than the displaced fluid, e.g. mobility ratio  $M > 1$ .

Chuoque and van Meurs (1959) presented a theoretical and experimental study on unstable displacements in laterally constrained permeable media. They defined an instability criterion based on the ratio of a perturbation wavelength to lateral media dimension and studied the scaling from laboratory prototype to reservoir conditions.

Russell and Prats (1962) investigated mathematically a well's behavior in a multilayer bounded radial reservoir for a single fluid with small and constant compressibility. The model includes 2-layers that are assumed to be homogeneous, isotropic and without gravity effects. The outer boundary is sealed in this work as are the upper and lower boundaries

Perrine and Lammers (1964) discussed a modified analysis of the perturbation equations for miscible displacement that resulted in stability coefficients. Their study focused on a 3-dimensional 3D porous media that is laterally bounded. The fluids used are incompressible, dispersion coefficients are constant, fluid density depends linearly on solvent concentration and fluid viscosity depends exponentially on solvent concentration.

Kyle and Perrine (1965) analyzed experimental results using a linear model with flow through spherical glass beads pack to measure rate of growth of the transition zone, flow velocity variations in the transition zone and the effect of a graded viscosity zone on stability. There is no macroscopic mixing. Results show that higher viscosity ( $M > 1$ ) ratios produced more random flow characteristics than did lower ones.

Perrine, R.L. and Gay, G.M. (1966) focused on numerical computation of miscible displacement of incompressible fluids in 3D heterogeneous reservoir with gravity and dispersion. This method is based on perturbation analysis.

Bloom (1967) presented a semianalytical technique applied to the sharp interface model of immiscible fluid displacement with small capillary effects and dispersion. The model

---

assumes tilted rectangular geometry, open outlet boundary, mass balance and pressure continuity across the interface, constant properties except at the boundary between both fluids, and no accumulation term. This work provides the position of the interface as a function of fractional pore volume.

Varnon and Greenkorn (1969) investigated unstable fingering in two-fluid flow through a porous medium to determine if the dimensionless finger width is unique. The paper also presents a discussion on literature concerning viscous and gravity-induced unstable displacements. Results show that viscous fingers are not always half as wide as their spacing.

Gringarten and Ramey (1973) tabulated source functions that may be used to generate many new reservoir flow solutions by means of the Newman product method for transient flow of a slightly compressible fluid in a homogeneous and anisotropic porous media bounded by a surface.

Kuo (1974) focused on the transient flow solution of the injection of a fluid into a porous medium to displace interstitial fluid initially present in the reservoir. The solution includes 2-phase flow, immiscible displacement in a homogeneous reservoir of infinite areal extent and finite thickness. Results show that fall-off pressure depends mainly on mobility of the displaced fluid after the well is shut-in.

Bentsen (1985) presented a new approach to predict a steady-state velocity at which a finger propagates based on force potential as opposed to velocity potential used in earlier work on viscous fingering. The paper considers an ideal porous media (identical flow paths in shape and size) and both fluids separated by a plane interface to treat the problem as a moving boundary problem.

Homsy (1987) presented a comprehensive review of viscous fingering in porous media including an evaluation of previous work.

Soucemarianadin *et al.* (1987) studied displacements in layered porous media and focus on the effects of viscous instability and capillarity. Results are based on experimental data and pore network simulation.

Greenkorn and Haselow (1988) discussed the scaling of unstable flow in heterogeneous porous media including a background review and also a discussion of miscible and immiscible displacements. The scaling is based on theories including the effects of gravity, viscosity, capillary pressure and heterogeneity. In a tilted gas-liquid immiscible displacement 4 flow regimes are identified: gravity induced stable flow, gravity dominated unstable flow, gravity-viscous balanced stable flow, and viscous dominated unstable flow

Christie (1989) described an accurate numerical method used by Christie and Bond (1987) for detailed simulation of miscible viscous fingering. They extended the work to

---

couple miscible and immiscible flows. It assumes 2-phase incompressible flow, 3-components, oil and solvent first contact miscible, ideal mixing for oil and solvent densities and one-fourth power mixing rule for viscosities and horizontal flow.

Chang *et al.*, (1994) presented the results of numerical simulation to investigate: conditions under which viscous fingering is the dominant flow pattern when gravity effects are included, comparison of first contact miscible displacements vs. CO<sub>2</sub> displacements for viscous fingering conditions and effects of heterogeneity, gravity, capillary pressure and dispersion on the flow pattern for field-scale CO<sub>2</sub> flooding. Results show that phase behavior and capillary effects tend to reduce fingering

Waggoner *et al.* (1992) investigated the combined effect of heterogeneity and viscous fingering on miscible displacements. They showed that resident fluid bypassing is caused by fingering, if  $M > 1$ , or heterogeneity, for large heterogeneity. This work was a numerical study of incompressible fluids.

Yang, Z. and Yortsos, Y. C. (1998) discussed boundary effect on the preferential propagation of viscous fingers for miscible displacement. The model is a 2-dimensional porous media in a rectilinear geometry. Fluids are incompressible. Displacing fluid is of lower viscosity than that of the displaced fluid.

Hyungjun *et al.* (2009) discussed the incompressible radial fingering problem in a 2-phase (gas-liquid) flow in a Hele-Shaw cell including viscous potential flow to account for the effects of viscosity on the normal stress at the gas-liquid interface. This method, removes discrepancies of previous solutions and experimental data for large capillary numbers.

Ghanbarnezhad (2012) presented a semi-analytical technique using the method of characteristics (MOC) including constant limited compressibility of the fluids and rock. The model assumes 1-D homogeneous aquifer, 2-component and 2-phase flow. Pressure gradients are calculated from numerical simulation, then used in the saturations evaluation from this paper's derivations.

Sohrabi *et al.*, (2012), discussed pore-scale interactions between supercritical CO<sub>2</sub> and brine based on experimental data. Results show that as CO<sub>2</sub> entered the porous medium, it began dissolving in water and displaced part of the water. The video clips and images taken during their experiments show that part of the CO<sub>2</sub> that has been dissolved in water can be released from solution and form a new free phase. The authors claim that this phenomenon, can impact the flow of CO<sub>2</sub> as well as the integrity of the storage.

Ajibola, J. (2016), presented results on numerical simulation, using conventional finite-difference simulator, to evaluate the predictions of analytical solutions for stability analysis and growth rate of the fingers at different Rayleigh numbers. Focuses on 2D, incompressible, 2-phase, 3-components miscible and immiscible displacement including effects of gravity, capillary pressure and molecular solvent diffusion.

As described above all of this experimental, theoretical and numerical work are based on incompressible or small compressible flows in porous media mainly under steady-state flow conditions

For CO<sub>2</sub> storage, there are no producers. Therefore; we are dealing with sealed (or partially sealed) outer boundaries and compressible fluids. Based on this, there is a need to evaluate the effect of compressibility and different outer boundary conditions on the ST instability criteria. This is the main objective of this work.

## Basic Equations

This work deals with one dimensional 1D linear compressible flow as in Figure 1.

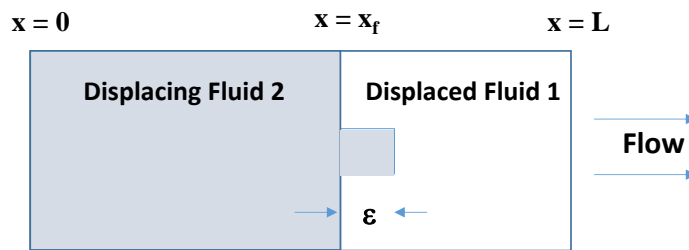


**Figure 1: Schematic of a 1-D linear displacement showing the perturbation,**

Fluid 2 is displacing fluid 1 with no transition (mixing) zone between them; the two components are locally segregated or the displacement is piston like. The absence of a transition zone means that the results apply to both miscible and immiscible displacements, absent dispersion or local capillary pressure. The main displacement boundary is at location

$x_f$  and moves with velocity  $\frac{dx_f}{dt}$ . We imagine an arbitrary perturbation  $\epsilon$  on the front that

moves with velocity  $\frac{d\epsilon}{dt}$ . The displacement is stable if the perturbation dies out with time (

$\frac{d\epsilon}{dt} < 0$ ) and unstable ( $\frac{d\epsilon}{dt} > 0$ ) or neutral ( $\frac{d\epsilon}{dt} = 0$ ), otherwise.

The condition for stability is necessary and sufficient; the condition for instability is only necessary inasmuch as there are several factors that would make a displacement. We use the word *unstable* to describe a displacement for which the perturbation would grow. We will show below that this criterion is equivalent to a criterion on the velocity of the front. Flow is from left to right

An important novelty here is the nature of the external boundary at  $x=L$ . Because our work considered compressible flow, this boundary may range from sealing (no flow) to

completely transparent (no barrier to flow) according to a pre-specified parameter in the problem. These definitions play a role in the problem according to Figure. 2.

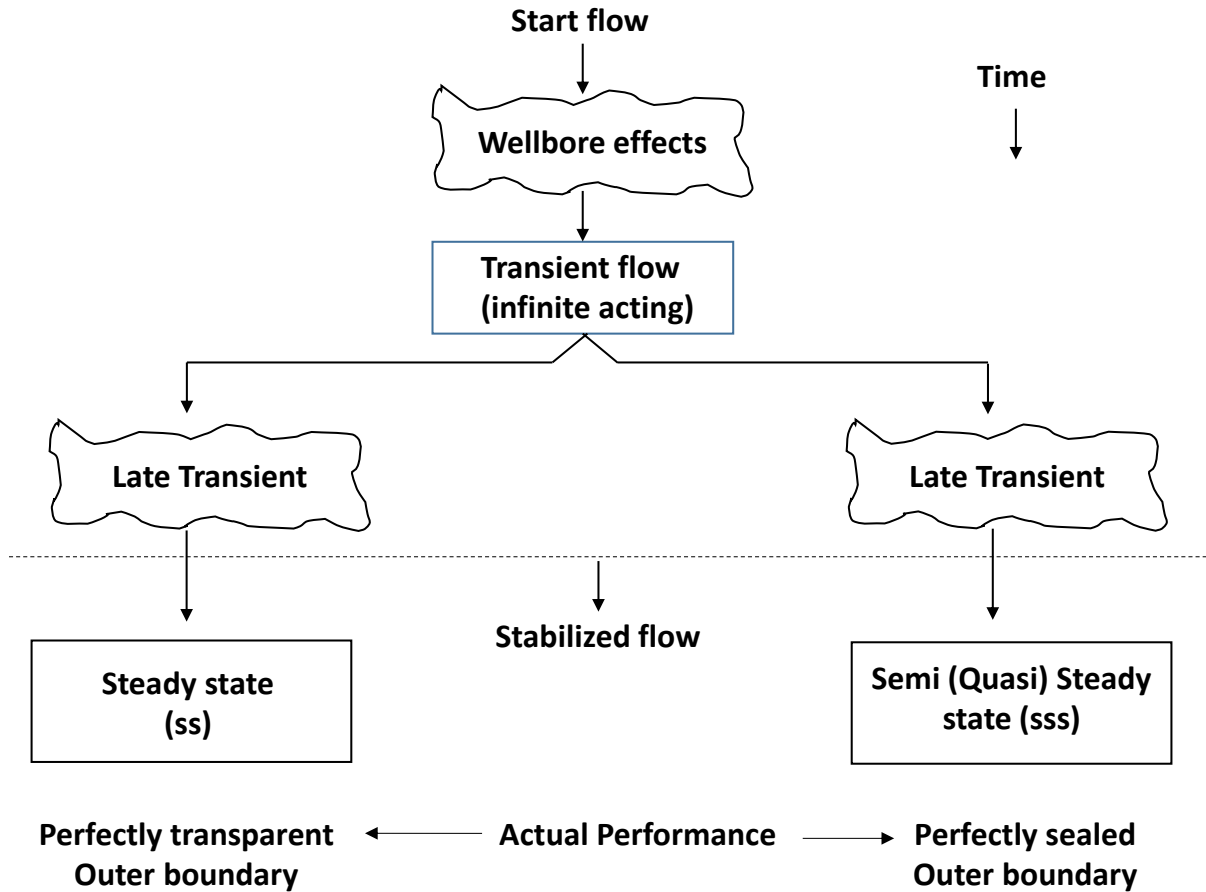


Figure 2: Schematic of flow regimes for constant flow rate (adapted from Walsh and Lake, 2003)

When flow begins at the left boundary  $x=0$ , there is a period of time when the pressure change caused by the flow does not reach the external; this time or flow regime is called transient or infinite-acting because the location of the boundary is unimportant to the flow. At late time (*stabilized* in Fig. 2) the nature of the external boundary dominates the flow. If the boundary is transparent, the flow is steady-state and flow does not depend on time; if the boundary is sealed, as though there is no source of fluid offtake, the flow is semi steady-state. Flow under both semi-steady state and steady flow is *stabilized*.

The analytical work presented below deals entirely with stabilized flow, under most conditions the longest period of flow. The flow of fluid 1 becomes stabilized before introducing fluid 2.

---

### Working Equations.

The conservation equations for components 1 and 2 are

$$\frac{\partial(C_1 ru)}{\partial x} = j \frac{\partial(C_1 r)}{\partial t} \quad (1)$$

$$\frac{\partial(C_2 ru)}{\partial x} = j \frac{\partial(C_2 r)}{\partial t} \quad (2)$$

where C is a concentration of the respective components in a single flowing phase, u is the volumetric flux, there is dispersive flux, no adsorption and porosity is constant. These rather restrictive assumptions are invoked so as to not detract from the main theme of this work, the role of compressibility. We seek a pair of working equations in this section.

Expanding Eqs. (1) and (2) gives

$$ru \frac{\partial C_1}{\partial x} + C_1 \frac{\partial(ru)}{\partial x} = j C_1 \frac{\partial r}{\partial t} + r \frac{\partial C_1}{\partial t} \quad (3)$$

$$ru \frac{\partial C_2}{\partial x} + C_2 \frac{\partial(ru)}{\partial x} = j C_2 \frac{\partial r}{\partial t} + r \frac{\partial C_2}{\partial t} \quad (4)$$

If component 1 is a tracer, then component 2 is present in excess and its concentration is essentially constant. The Eqn. (4) becomes

$$\frac{\partial(ru)}{\partial x} = j \frac{\partial r}{\partial t} \quad (5)$$

Which is a continuity equation for the carrier fluid. And combining this with the first equation gives

$$u \frac{\partial C}{\partial x} = j \frac{\partial C}{\partial t} \quad (6)$$

where we have replaced  $C_1$  with just C, the subscript now being superfluous. Equations (5) and (6) are the two working equations for tracer flow. We will deal with Eq. (6) first.

---

**Tracer flow.** The solution to the Eq. (6) is from the method of characteristics where

$$v|_{dC=0} = \frac{u}{j} \quad (7)$$

is the velocity of a fixed concentration C. For incompressible flow, the velocity is a constant. For compressible flow it is a function of time and position. Equation (7) gives the velocity of a point with velocity  $u(x,t)$ , which is given by the solution to Eq. 6 (Appendix A). If the front is at  $x = x_f$ , then its velocity is given by

$$\frac{dx_f}{dt} = \frac{u(x_f, t)}{j} \quad (8)$$

**Behavior of perturbation.** From the definition of the perturbation given above in Figure 1, we have

$$\frac{de}{dt} = \frac{d(x_f + e)}{dt} - \frac{dx_f}{dt} = \frac{1}{j} \left( u(x_f + e, t) - u(x_f, t) \right) \quad (9)$$

Which means that the behavior of the perturbation is entirely determined by the behavior of the carrier fluid velocity. If  $u(x_f + e, t) > u(x_f, t)$ , the volumetric flow rate increasing from left to right, the flow is unstable, otherwise it is stable. This is a substantial simplification from solving for the behavior of the perturbation because all that is needed is an examination of the trends in carrier velocity. The perturbation can be at any position  $x$  and time. Note that we should have  $\frac{de}{dt} = 0$  for incompressible flow.

Similarly to Eq. (9), we can express the perturbation growth as follows:

$$\begin{aligned} \dot{\varepsilon} &= \frac{d\varepsilon}{dt} = \Delta t \frac{d}{dt} \left( \frac{x_f(t + \Delta t) - x_f(t)}{\Delta t} \right) \\ \dot{\varepsilon} &= \frac{d\varepsilon}{dt} = \Delta t \frac{d^2 x_f}{dt^2} \end{aligned} \quad (9a)$$

As  $\Delta t$  is always positive, the criterion for the perturbation growth will be driven by the sign of the  $\frac{d^2 x_f}{dt^2}$ .

---

**Velocity of carrier fluid.** The quantity on the left side of Eq. (5) is the mass flux or

$$\frac{\partial m}{\partial x} = \phi \frac{\partial \rho}{\partial t} \quad (10)$$

But Darcy's Law, the primary connection between density and pressure, is based on volumetric flux which means it is more convenient to continue with Eq. (5). Inserting Darcy's law into Eq. (5) gives

$$-\frac{k}{m} \frac{\partial}{\partial x} \left( r \frac{\partial P}{\partial x} \right) = j \frac{\partial r}{\partial t} \quad (11)$$

assuming that permeability and viscosity are independent of pressure, which is consistent with tracer flow.

**Fluid properties.** The connection between density and fluid compressibility is given by

$$c_f = \frac{1}{r} \frac{\partial r}{\partial P} \quad (12)$$

where  $c_f$  the fluid compressibility is a constant, not necessarily small. Combining Eqs. (11) and (12) gives the working equation

$$\frac{\partial}{\partial x} \left( \rho \frac{\partial P}{\partial x} \right) = \frac{\rho}{\alpha} \frac{\partial P}{\partial t} \quad (13)$$

where  $\alpha$  is the diffusivity. See Nomenclature section. We use the  $c_f \Delta P$  cut-off to differentiate the compressibility group (Dake, 1978, Dranchuk and Quon, 1967). Here, small and large compressibility groups correspond to the cases where  $c_f \Delta P < 0.1$  and  $c_f \Delta P > 0.1$  respectively

For small compressibility ( $c_f \Delta P < 0.1$ ), the definition (12) is linear

$$\rho = \rho_R (1 + c_f (P - P_R)) \quad (14)$$

For large constant compressibility ( $c_f \Delta P > 0.1$ ), we have

$$\rho = \rho_R e^{c_f (P - P_R)} \quad (14a)$$

And for incompressible flow ( $c_f \Delta P = 0$ ), the density is constant.

Insights based on solutions to Eqs. (9), (13), and (14a) comprise the remainder of this work.

## Results

This section discusses the analytic solution formulation for the tracer flow analog, including the method to qualitatively and quantitatively perform the perturbation analysis. Pressure and rates profiles are compared against numerical simulation results for different fluid compressibilities and different outer boundary conditions.

### Analytic Solutions

The formulations discussed in this section corresponds to the solutions to Eqn. (5) for single fluid stabilized flow under different compressibility and boundary conditions (BC). A total of 36 possible solutions, depending on the boundary conditions (inlet-pressure, outlet-pressure, mass flux and volumetric flux) combinations, as shown in Table 1 through Table 4. Each table corresponds to a different fluid compressibility group to define the fluid density as a function of pressure in the working equation (13). In this regard, the very small compressibility group correspond to cases where  $c_f \Delta P < 0.01$ , while small and large compressibility groups correspond to the cases where  $c_f \Delta P < 0.1$  and  $c_f \Delta P > 0.1$  respectively (Dake, 1978, Dranchuk and Quon, 1967). Cases including fluxes and inlet-pressure showed the same solution for the corresponding compressibility group regardless of BC's combination. The term "f" in solutions in Table 1 through Table 4, is the outlet to inlet mass flux ratio. For steady-state flow cases f=1 (transparent outer boundary) and for the unsteady-state flow cases (sealed boundary) f=0, Figure 2.

**Table 1: Stabilized pressure solutions for zero compressibility and different outer boundary conditions**

Compressibility	Inlet	Outlet	Pressure Solution
zero	Mass flux	Mass flux	$P(x) = -\frac{u_o \mu}{k} x + P_o$
zero	Volumetric flux	Mass flux	$P(x) = -\frac{u_o \mu}{k} x + P_o$
zero	Pressure	Mass flux	$P(x) = -\frac{u_o \mu}{k} x + P_o$
zero	Mass flux	Volumetric flux	$P(x) = -\frac{u_o \mu}{k} x + P_o$
zero	Volumetric flux	Volumetric flux	$P(x) = -\frac{u_o \mu}{k} x + P_o$
zero	Pressure	Volumetric flux	$P(x) = -\frac{u_o \mu}{k} x + P_o$
zero	Mass flux	Pressure	$P(x) = -\frac{u_o \mu}{k} (x - L) + P_L$
zero	Volumetric flux	Pressure	$P(x) = -\frac{u_o \mu}{k} (x - L) + P_L$
zero	Pressure	Pressure	$P(x) = -\frac{(P_o - P_L)}{L} x + P_o$

**Table 2: Stabilized pressure solutions for very small compressibility and different outer boundary conditions**

Compressibility	Inlet	Outlet	Pressure Solution
Very small and constant $c_f \Delta P < 0.01$	Mass flux	Mass flux	$P(x, t) = \frac{u_o \mu}{kL} (1-f) \frac{x^2}{2} - \frac{u_o \mu}{k} x + P_o$
Very small	Volumetric flux	Mass flux	$P(x, t) = \frac{u_o \mu}{kL} (1-f) \frac{x^2}{2} - \frac{u_o \mu}{k} x + P_o$
Very small	pressure	Mass flux	$P(x, t) = \frac{u_o \mu}{kL} (1-f) \frac{x^2}{2} - \frac{u_o \mu}{k} x + P_o$
Very small	Mass flux	Volumetric flux	$P(x, t) = \frac{u_o \mu}{kL} (1-f) \frac{x^2}{2} - \frac{u_o \mu}{k} x + P_o$
Very small	Volumetric flux	Volumetric flux	$P(x, t) = \frac{u_o \mu}{kL} (1-f) \frac{x^2}{2} - \frac{u_o \mu}{k} x + P_o$
Very small	pressure	Volumetric flux	$P(x, t) = \frac{u_o \mu}{kL} (1-f) \frac{x^2}{2} - \frac{u_o \mu}{k} x + P_o$
Very small	Mass flux	pressure	$P(x, t) = \frac{u_o \mu}{kL} (1-f) \frac{x^2 - L^2}{2} - \frac{u_o \mu}{k} (x - L) + P_L$
Very small	Volumetric flux	pressure	$P(x, t) = \frac{u_o \mu}{kL} (1-f) \frac{x^2 - L^2}{2} - \frac{u_o \mu}{k} (x - L) + P_L$
Very small	pressure	pressure	$P(x, t) = \frac{u \mu}{kL} (1-f) \frac{(x^2 - xL)}{2} + \left( \frac{P_L - P_o}{L} \right) x + P_o$

**Table 3: Stabilized pressure solutions for small compressibility and different outer boundary conditions**

Compressibility	Inlet	Outlet	Pressure Solution
Small and constant $c_f \Delta P < 0.1$	Mass flux	Mass flux	$P(x, t) + c_f \frac{P(x, t)^2}{2} = \frac{\dot{m}_o \mu}{\rho_R k L} (1-f) \frac{x^2}{2} - \frac{\dot{m}_o \mu}{\rho_R k} x + P_o + \frac{P_o^2}{2}$
Small	Volumetric flux	Mass flux	$P(x, t) + c_f \frac{P(x, t)^2}{2} = \frac{\dot{m}_o \mu}{\rho_R k L} (1-f) \frac{x^2}{2} - \frac{\dot{m}_o \mu}{\rho_R k} x + P_o + c_f \frac{P_o^2}{2}$
small	pressure	Mass flux	$P(x, t) + c_f \frac{P(x, t)^2}{2} = \frac{\dot{m}_o \mu}{\rho_R k L} (1-f) \frac{x^2}{2} - \frac{\dot{m}_o \mu}{\rho_R k} x + P_o + c_f \frac{P_o^2}{2}$
small	Mass flux	Volumetric flux	$P(x, t) + c_f \frac{P(x, t)^2}{2} = \frac{\dot{m}_o \mu}{\rho_R k L} (1-f) \frac{x^2}{2} - \frac{\dot{m}_o \mu}{\rho_R k} x + P_o + c_f \frac{P_o^2}{2}$
small	Volumetric flux	Volumetric flux	$P(x, t) + c_f \frac{P(x, t)^2}{2} = \frac{\dot{m}_o \mu}{\rho_R k L} (1-f) \frac{x^2}{2} - \frac{\dot{m}_o \mu}{\rho_R k} x + P_o + c_f \frac{P_o^2}{2}$
small	pressure	Volumetric flux	$P(x, t) + c_f \frac{P(x, t)^2}{2} = \frac{\dot{m}_o \mu}{\rho_R k L} (1-f) \frac{x^2}{2} - \frac{\dot{m}_o \mu}{\rho_R k} x + P_o + c_f \frac{P_o^2}{2}$
small	Mass flux	pressure	$P(x, t) + c_f \frac{P(x, t)^2}{2} = \frac{\dot{m}_o \mu}{\rho_R k L} (1-f) \frac{(x^2 - L^2)}{2} - \frac{\dot{m}_o \mu}{\rho_R k} (x - L) + P_L + c_f \frac{P_L^2}{2}$
Small	Volumetric flux	pressure	$P(x, t) + c_f \frac{P(x, t)^2}{2} = \frac{\dot{m}_o \mu}{\rho_R k L} (1-f) \frac{(x^2 - L^2)}{2} - \frac{\dot{m}_o \mu}{\rho_R k} (x - L) + P_L + c_f \frac{P_L^2}{2}$
small	pressure	pressure	$P(x, t) + c_f \frac{P(x, t)^2}{2} = \frac{\dot{m}_o \mu}{\rho_R k L} (1-f) (x^2 - xL) + \left( P_L + c_f \frac{P_L^2}{2} \right) \frac{x}{L} - \left( P_o + c_f \frac{P_o^2}{2} \right) \left( \frac{x-L}{L} \right)$

**Table 4: Stabilized pressure solutions for large compressibility and different outer boundary conditions**

Compressibility	Inlet	Outlet	Pressure Solution
Large and constant, $c_f \Delta P > 0.1$	Mass flux	Mass flux	$e^{c_f P(x,t)} = \frac{c_f \dot{m}_o \mu}{\rho_R k L} (1-f) \frac{x^2}{2} - \frac{c_f \dot{m}_o \mu}{\rho_R k} x + e^{c_f P_o}$
large	Volumetric flux	Mass flux	$e^{c_f P(x,t)} = \frac{c_f \dot{m}_o \mu}{\rho_R k L} (1-f) \frac{x^2}{2} - \frac{c_f \dot{m}_o \mu}{\rho_R k} x + e^{c_f P_o}$
large	pressure	Mass flux	$e^{c_f P(x,t)} = \frac{c_f \dot{m}_o \mu}{\rho_R k L} (1-f) \frac{x^2}{2} - \frac{c_f \dot{m}_o \mu}{\rho_R k} x + e^{c_f P_o}$
large	Mass flux	Volumetric flux	$e^{c_f P(x,t)} = \frac{c_f \dot{m}_o \mu}{\rho_R k L} (1-f) \frac{x^2}{2} - \frac{c_f \dot{m}_o \mu}{\rho_R k} x + e^{c_f P_o}$
large	Volumetric flux	Volumetric flux	$e^{c_f P(x,t)} = \frac{c_f \dot{m}_o \mu}{\rho_R k L} (1-f) \frac{x^2}{2} - \frac{c_f \dot{m}_o \mu}{\rho_R k} x + e^{c_f P_o}$
large	pressure	Volumetric flux	$e^{c_f P(x,t)} = \frac{c_f \dot{m}_o \mu}{\rho_R k L} (1-f) \frac{x^2}{2} - \frac{c_f \dot{m}_o \mu}{\rho_R k} x + e^{c_f P_o}$
large	Mass flux	pressure	$e^{c_f P(x,t)} = \frac{c_f \dot{m}_o \mu}{\rho_R k L} (1-f) \frac{(x^2 - L^2)}{2} - \frac{c_f \dot{m}_o \mu}{\rho_R k} (x - L) + e^{c_f P_L}$
large	Volumetric flux	pressure	$e^{c_f P(x,t)} = \frac{c_f \dot{m}_o \mu}{\rho_R k L} (1-f) \frac{(x^2 - L^2)}{2} - \frac{c_f \dot{m}_o \mu}{\rho_R k} (x - L) + e^{c_f P_L}$
large	pressure	pressure	$e^{c_f P(x,t)} = \frac{c_f \dot{m}_o \mu}{\rho_R k L} (1-f) \frac{(x^2 - xL)}{2} + \left( \frac{e^{c_f P_L} - e^{c_f P_o}}{L} \right) (x - L) + e^{c_f P_L}$

### Comparison Against Numerical Simulation

Different cases were run using a commercial black-oil numerical simulator for comparison purposes. Outer boundary conditions and fluid compressibility were varied in each case. The model dimensions are 1000 ft x 1ft x 1 ft in the x, y and z-direction, respectively, and included 2000 cells in the x-direction. The relative permeability curves are assumed to have a very narrow mobility region as to achieve a sharp displacement front within the simulation runs similar to the analytic solution.

In general, black-oil simulators are good for small fluid compressibility where changes in fluid density are not very large. As fluid compressibility increases to the order of  $10^{-4}$  1/psi or larger, simulation results show significant material balance errors, especially to calculate the displacement front position.

Pressure and rate from analytical and simulation results are compared in this section for different fluid compressibility and different outlet-inlet mass flux ratio (f). The steady-state (f=1) results are in Figure 3 and Figure 4, while the unsteady-state (f=0) results are in Figure 7 and Figure 8. Figure 5 and Figure 6 include the results for an in-between case (f=0.5) to show the generality of the formulation developed in this work. All these cases include inlet and outlet volumetric fluxes as boundary conditions and the inlet pressure is known. Results show a perfect agreement between simulation and analytic solution from this work.

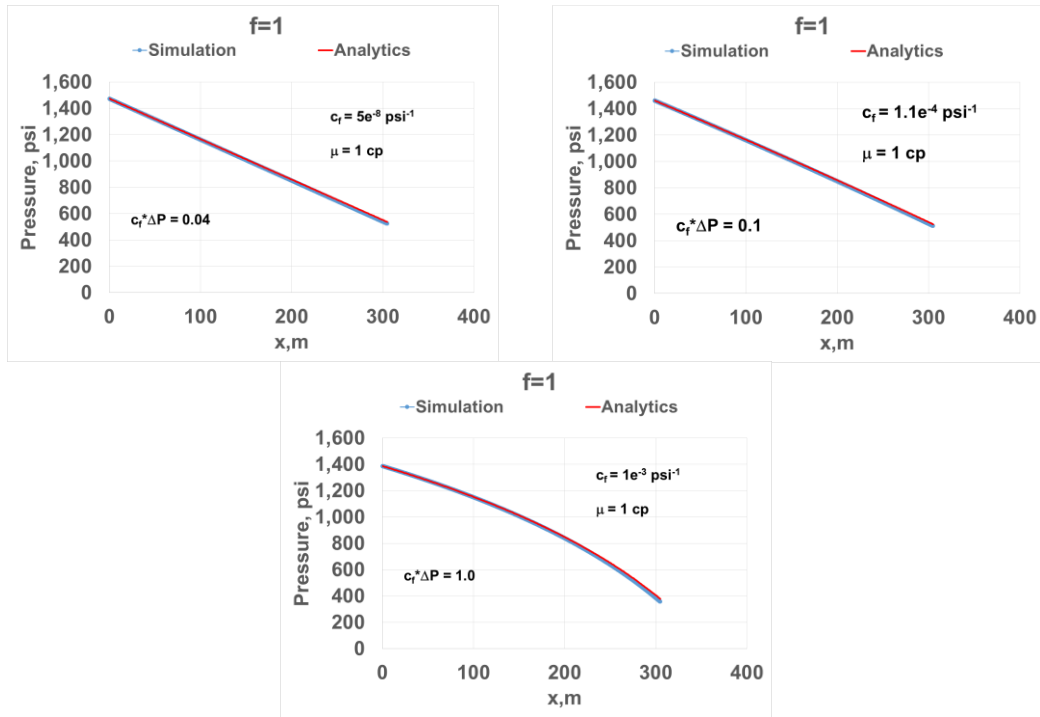


Figure 3: Comparison of analytical and simulated pressure profiles for single fluid under different compressibility ( $f=1$ , steady-state flow transparent outer boundary).

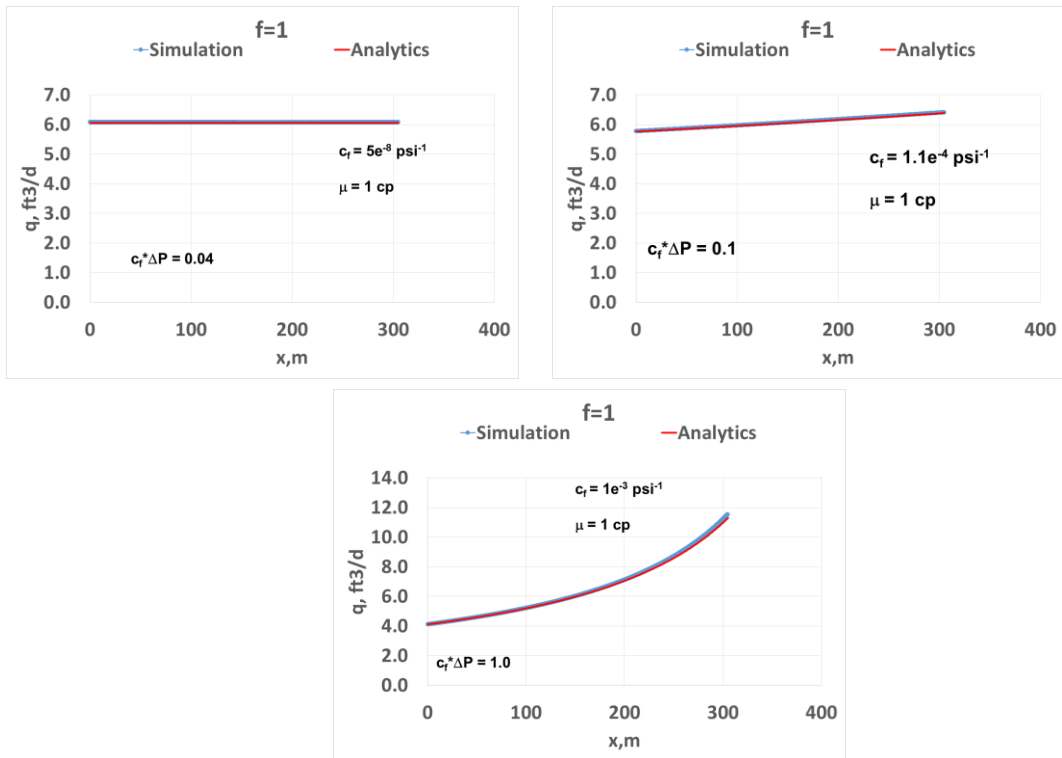


Figure 4: Analytical and Simulation rate (reservoir conditions) results comparison for single fluid under different compressibility ( $f=1$ , steady-state flow).

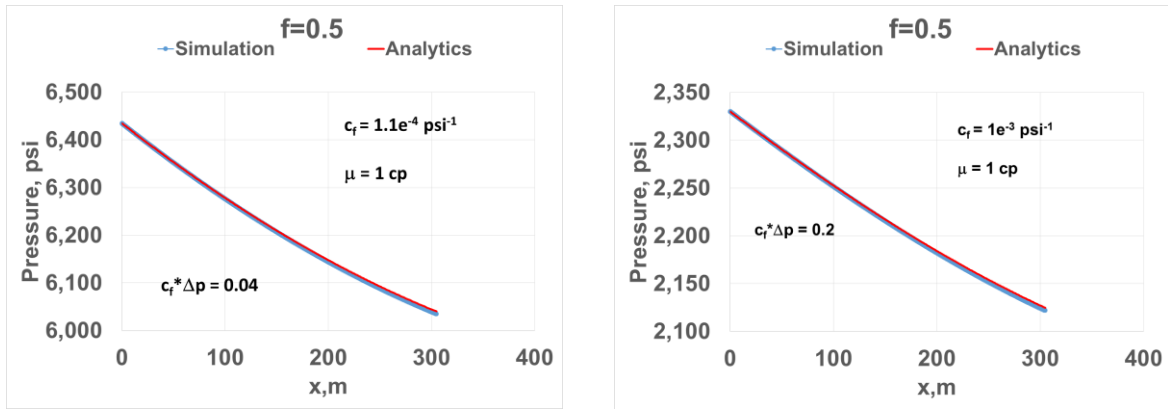


Figure 5: Comparison of analytical and simulated pressure profiles for single fluid under different compressibility ( $f=0.5$ , partially sealed outer boundary).

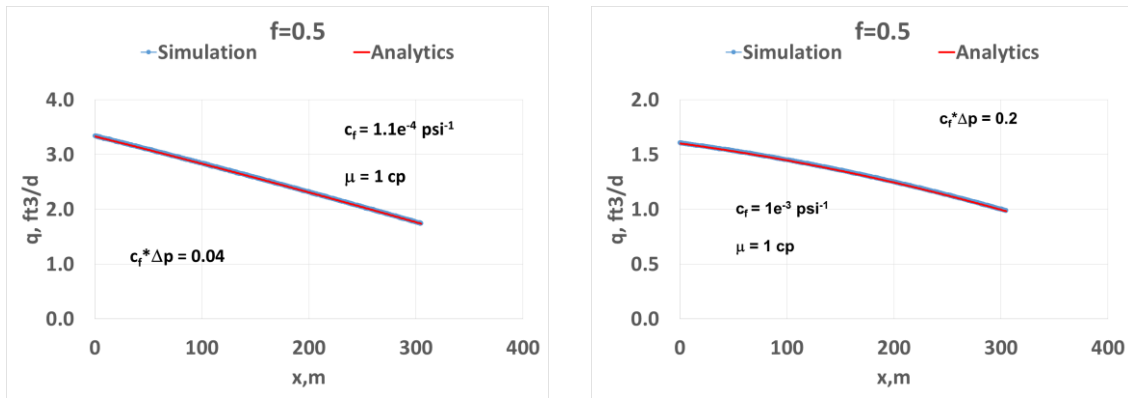


Figure 6: Comparison of analytical and simulation rate (reservoir volume) results comparison for single fluid under different compressibility ( $f=0.5$ , partially sealed outer boundary).

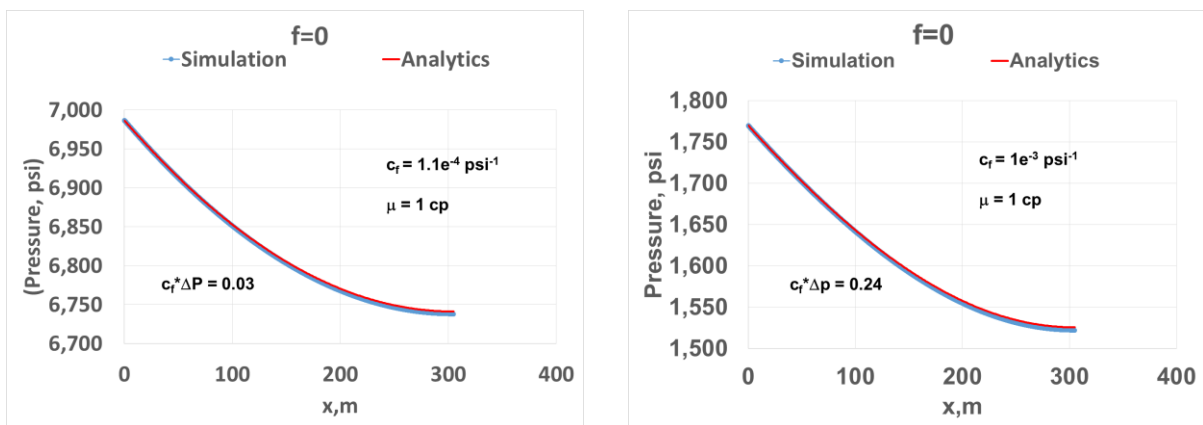


Figure 7: Comparison of analytical and simulation pressure profiles for single fluid under different compressibility ( $f=0$ , semisteady-state flow, sealed outer boundary).

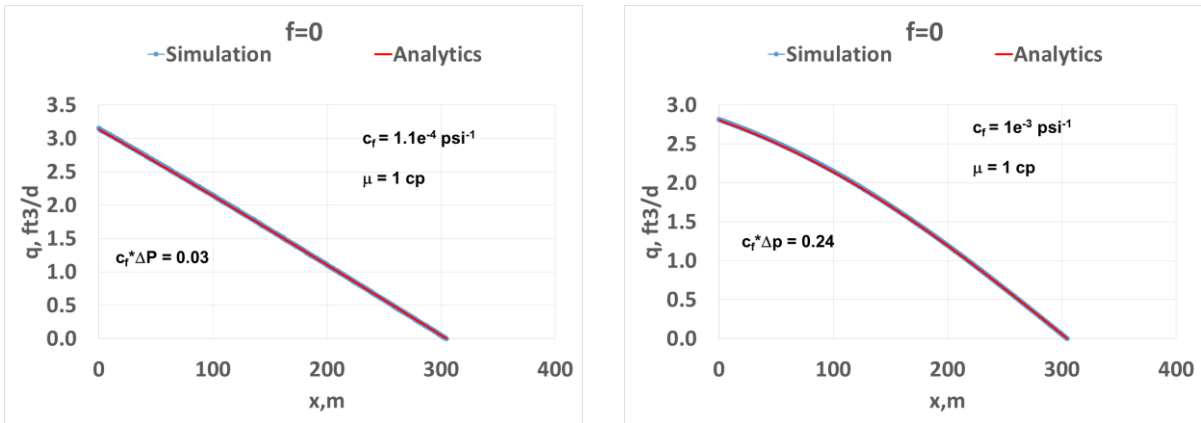


Figure 8: Comparison of analytical and simulated rates (reservoir conditions) for single fluid under different compressibility ( $f=0$ , semisteady-state flow, sealed outer boundary).

### Instability Analysis - Tracer Flow

This section presents the instability results based on the perturbation analysis for tracer flow. The mathematical formulation is detailed in Appendix A. Figure 9 and Figure 10 show the comparison of the front position history from simulation and analytics results in the case of stabilized steady state ( $f=1$ ) and unsteady state ( $f=0$ ) flow respectively. Results show good matches in both cases. Under steady-state flow conditions, the displacement becomes more unstable as compressibility increases. This is shown as a positive and increasing slope in the front position history plot in Figure 9. In the case of a sealed boundary or unsteady state flow, results still show a positive slope, but in this case the slope is decreasing towards the outlet because of the no-flow boundary. This means that the displacement will become stable near the outlet boundary

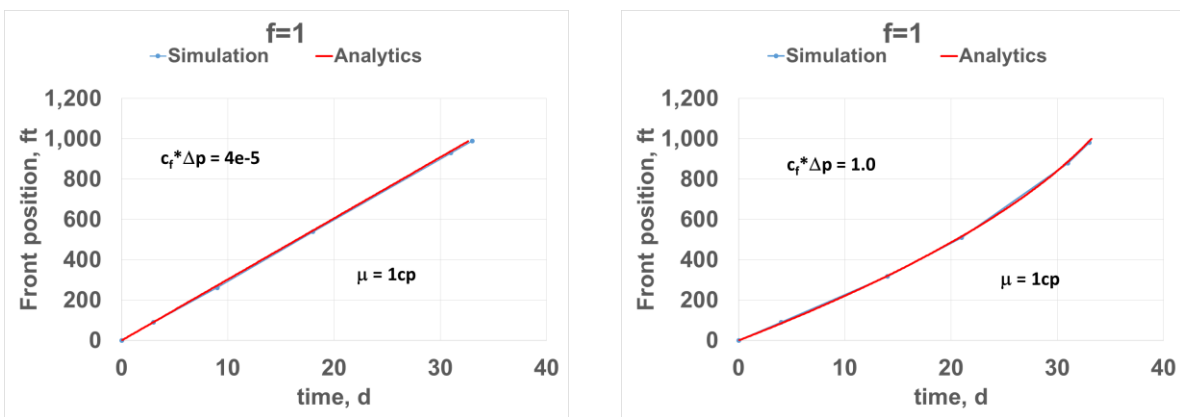


Figure 9: Compressibility effect on front position history under stabilized steady-state flow ( $f=1$ )

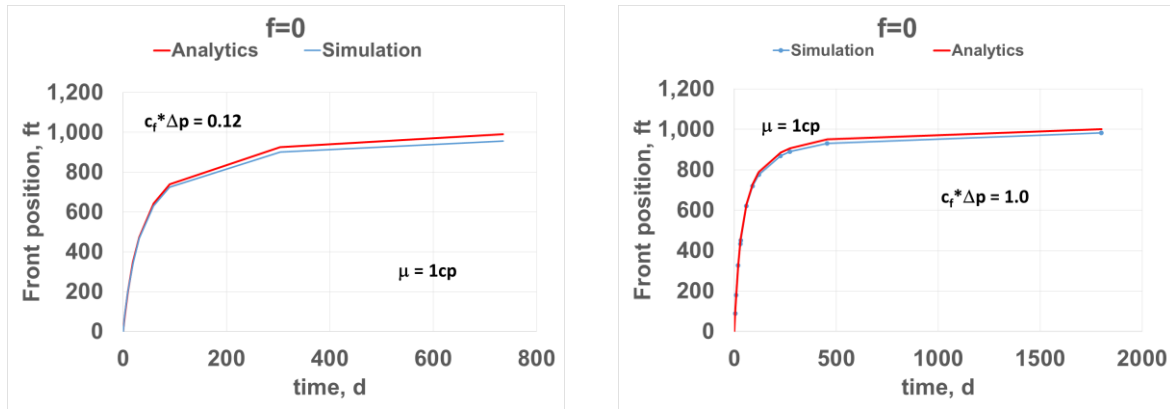


Figure 10: Compressibility effect on front position history under stabilized unsteady-state flow ( $f=0$ )

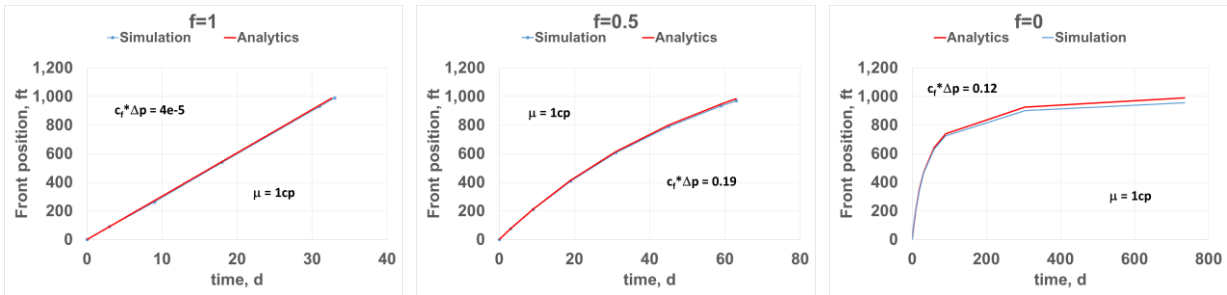


Figure 11: Boundary effect on front position under stabilized flow for small and constant compressibility fluid

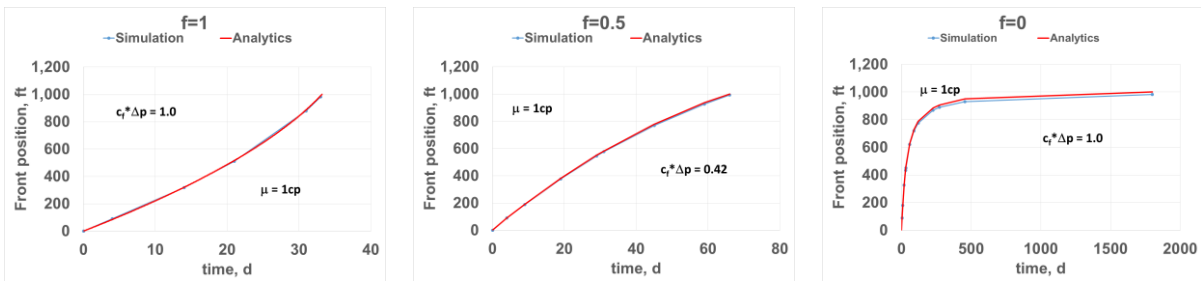


Figure 12: Boundary effect on front position under stabilized flow for large and constant compressibility fluid

---

## Conclusions

1. The ST approach analyzed the behavior of a perturbation of a displacement front for a tracer in stabilized flow. A perturbation in the tracer front position will grow and the front will be unstable when the volumetric flux of the fluid increases with distance to the production end.
2. For steady-state flow (transparent outer boundary) adding compressibility always makes displacements more unstable. The simple reason for this is that as flow proceeds downstream, pressure declines, specific volume (1/density) of the fluid increases (density decreases) and velocity increases.
3. For semi-steady flow (sealed outer boundary) displacements will become more stable as a front approaches the outlet boundary simply because the front velocity must slow down there and average pressure rise.

## Acknowledgements

Larry W. Lake holds the Shahid and Sharon Chair at the University of Texas. This work was supported by DOE through the BEG GoMCarb project.

## References

Ajibola, Jeuspelumi, Adam, Alexander and Muggeridge, Ann. Gravity Driven Fingering and Mixing During CO<sub>2</sub> Sequestration. SPE Asia Pacific Oil & Gas Conference and Exhibition. 2016. SPE-182317-MS.

Bentsen, R.G. A New Approach to Instability Theory in Porous Media. Society of Petroleum Engineers Journal. 1985. SPE-12725-PA

Bloom, Sanford G. A Semianalytical Method for the Mathematical Solution of a Moving Boundary Problem. Fall Meeting of the Society of Petroleum Engineers of AIME. 1967. SPE-1882-MS

Chang, Yih-Bor, Lim, M.T., Pope, G.A., Sepehrnoori, K. CO<sub>2</sub> Flow Patterns Under Multiphase Flow: Heterogeneous Field-Scale Conditions. SPE Reservoir Engineering. 1994. SPE-22654-PA

Chouke, R. L., van Meurs, P., van der Poel, C. The Instability of Slow, Immiscible, Viscous Liquid-Liquid Displacements in Permeable Media. Trans. AIME 216:1 88-94, 1959.

Christie, M.A. High-Resolution Simulation of Unstable Flows in Porous Media. SPE Reservoir Engineering Journal. 1989. SPE-16005-PA

Christie, M.A. and Bond, D.J.: "Detailed Simulation of Unstable Processes in Miscible Flooding," SPERE (Nov. 1987) 514-22; Trans. AIME 283

---

Dake L. P. *Fundamentals of Reservoir Engineering*, Elsevier, 1978

Dranchuk, P.M. and Quon, D.: "Analysis of the Darcy Continuity Equation". Producers Monthly Journal, volume 31-32, pages 25-28, October 1967.

Ghanbarnezhad Moghanloo, Rouzbeh. Applying Method of Characteristics to Model the Flow of Compressible CO<sub>2</sub> in Aquifers. SPE Western Regional Meeting. Bakersfield, California, USA.2012. SPE-154114-MS

Greenkorn, R.A. and Haselow, J.S. Unstable Flow in Heterogeneous Porous Media. SPE General. January 1, 1988. SPE-17114-MS

Gringarten, Alain C. and Ramey, Henry J., Jr. The Use of Source and Green's Functions in Solving Unsteady-Flow Problems in Reservoirs. Society of Petroleum Engineers Journal. 1973. SPE-3818-PA

Hill, S., Channeling in Packed Columns. *Chem. Eng. Sci. I* : 247-53, 1952

Homsy, G. M. Viscous Fingering in Porous Media. *Ann. Rev. Fluid Mech.* 1987. 19, pp. 271-311.

Hyungjun Kim, Toshio Funada, Daniel D. Joseph, and G. M. Homsy. Viscous Potential Flow Analysis of Radial fingering in a Hele-Shaw cell. *Physics of Fluids* 21, 074106 \_2009.

Kuo, C.H. A Moving Boundary Problem In Underground Storage. SPE General, January 1, 1974. SPE-4799-MS

Kyle, C.R. and Perrine, R.L. Experimental Studies of Miscible Displacement Instability. Society of Petroleum Engineers Journal. September 1, 1965. SPE-1113-PA

Nilsen, Halvor Moll and Lie, Knut-Andreas. Front Tracking Methods for Use in Streamline Simulation of Compressible Flow. SPE Reservoir Simulation Symposium. The Woodlands, Texas. 2009. SPE-119099-MS

Perrine, R.L. and Gay, G.M. Unstable Miscible Flow in Heterogeneous Systems. Society of Petroleum Engineers Journal. 1966. SPE-1436-PA

Perrine, Richard L. and Lammers, Donald L. Numerical Solution of The Perturbation Equations For Miscible Displacement. 39th Annual Fall Meeting of the Society of Petroleum Engineers on Oct. 11-14, 1964. SPE-960-MS

Russell, D.G. and Prats, M.. Performance of Layered Reservoirs with Crossflow--Single-Compressible-Fluid Case. 1962. SPE-99-PA

Saffman P. G., Taylor S. G., The penetration of a fluid into a porous medium or Hele-Shaw cell containing a more viscous liquid. *Proc. R. Soc. London Ser. A* 245:312-329, 1958.

---

Sohrabi, Mehran, Riazi, Masoud, Bernstone, Christian, Jamiolahmady, Mahmoud and Christensen, Nils-Peter. New Insights Into CO<sub>2</sub> Injection and Storage in Saline Aquifers. SPE Europec/EAGE Annual Conference. 2012. SPE-154527-MS

Soucemarianadin, A., Touboul, E., Bourlion, M., Nittmann, J., Lenormand, R. Sweep Efficiency in Multilayered Porous Media: Contrast Between Stable and Unstable Flow. SPE Annual Technical Conference and Exhibition. 1987. SPE-16955-MS

Varnon, J.E. and Greenkorn, R.A. Unstable Two-Fluid Flow in a Porous Medium. Society of Petroleum Engineers Journal. 1969. SPE-2182-PA

Walsh, Mark P. and Lake, Larry W. *Primary Hydrocarbon Recovery*, Elsevier, 2004.

Waggoner, J.R., Castillo, J.L., and Lake, L.W., "Simulation of EOR Processes in Stochastically Generated Permeable Media," SPE Formation Evaluation, Vol. 7, No. 2, June, 1992.

Wu, Yun, Bryant, Steven L., and Lake, Larry W., "Pressure Management of CO<sub>2</sub> Storage by Closed-loop Surface Dissolution", Energy Procedia 114, 2017, pp. 4811-4821.

Yang, Zhengming and Yortsos, Yanis C. Effect of No-Flow Boundaries on Viscous Fingering in Porous Media of Large Aspect Ratio. SPE Journal. 1998. SPE-51257-PA

## **Nomenclature** F is force; m is mass; L is length, t is time

A: cross-sectional area [=] L<sup>2</sup>  
c<sub>f</sub>: fluid compressibility [=] L<sup>2</sup>/F  
c<sub>r</sub>: rock compressibility [=] L<sup>2</sup>/F  
c<sub>t</sub>: total compressibility [=] L<sup>2</sup>/F  
f: outlet to inlet mass flux ratio, unitless  
k: absolute permeability [=] L<sup>2</sup>  
L: total length of the system [=] L  
 $\dot{m}$ : mass flux [=] m/L<sup>2</sup>-t  
P: pressure [=] F/L<sup>2</sup>  
P<sub>L</sub>: outlet pressure [=] F/L<sup>2</sup>  
P<sub>o</sub>: inlet pressure [=] F/L<sup>2</sup>  
P<sub>R</sub>: reference pressure [=] F/L<sup>2</sup>  
q: volumetric fluid rate [=] L<sup>3</sup>/t  
t: time [=] t  
u: Darcy velocity – volumetric flux [=] L/t  
V<sub>p</sub>: pore volume [=] L<sup>3</sup>  
x: flow direction [=] L  
x<sub>f</sub>: front position  
u<sub>f</sub>: front velocity [=] L/t

---

## Symbols

$\alpha$ :	diffusivity constant [=] L <sup>2</sup> /t
$\varepsilon$ :	perturbation [=] L
$\phi$ :	porosity, fraction
$\mu$ :	fluid viscosity [=] F-t/L <sup>2</sup>
$\theta$ :	substitution variable, unitless
$\rho$ :	fluid density [=] m/L <sup>3</sup>
$\rho_R$ :	reference fluid density [=] m/L <sup>3</sup>

## Appendix A: Analytical Solution for Large and Constant Compressibility – Tracer Flow

This Appendix presents an analytical solution for tracer flow, or flow in which the properties of the carrier fluid are unaffected by component concentration. We start with Eqn. (13), repeated below, for large and constant compressibility.

$$\frac{\partial}{\partial x} \left( \rho \frac{\partial P}{\partial x} \right) = \frac{\rho}{\alpha} \frac{\partial P}{\partial t} \quad (13)$$

For Stabilized flow...

$$\frac{\partial}{\partial x} \left( \rho \frac{\partial P}{\partial x} \right) = C_o \quad (15)$$

$$\frac{\rho}{\alpha} \frac{\partial P}{\partial t} = C_o \quad (15a)$$

As stated previously, flow conditions are limited to 1-D homogeneous linear flow with no gravity or capillary effects. In this particular formulation, we are not limited to small compressibility, therefore we use the auxiliary Eqn. (14a) to evaluate fluid density as a function of pressure.

$$r = r_R e^{c_f P} \quad (14a)$$

Where we have taken the reference pressure to be zero. Substituting Eqn. (14a) into (15) and (15a), we have

$$\frac{\partial}{\partial x} \left( r_R e^{c_f P} \frac{\partial P}{\partial x} \right) = C_o \quad (16)$$

---


$$\frac{\partial}{\partial x} \left( e^{c_f P} \frac{\partial P}{\partial x} \right) = \frac{C_o}{r_R} \quad (16a)$$

Let's define

$$q = e^{c_f P} \quad (16b)$$

As a sort of compressible flow potential (similarly to the work by Dranchuk and Quon, 1967). Then

$$dq = c_f q dP$$

and,

$$\frac{\partial P}{\partial x} = \frac{1}{c_f q} \frac{\partial q}{\partial x} \quad (16c)$$

$$\frac{\partial P}{\partial t} = \frac{1}{c_f q} \frac{\partial q}{\partial t} \quad (16d)$$

Substituting Eqn. (16b) and (16c) in Eqn. (16a)

$$\frac{\partial}{\partial x} \left( \frac{\partial q}{\partial x} \right) = \frac{c_f}{r_R} C_o \quad (17)$$

Repeating the same substitution for the time derivative, we have

$$\frac{\partial q}{\partial t} = \frac{c_f}{r_R} C_o \quad (18)$$

After first integration of Eqn (17)

$$\frac{\partial q}{\partial x} = \frac{c_f}{r_R} C_o x + C_1$$

Then

$$q = \frac{c_f}{r_R} C_o \frac{x^2}{2} + C_1 x + C_2 \quad (19)$$

---

Using Eqn (19) to evaluate the time derivative of  $\theta$ , we have

$$\frac{\partial \theta}{\partial t} = \frac{dC_1}{dt} x + \frac{dC_2}{dt}$$

As the term  $\frac{\partial \theta}{\partial t}$  cannot be a function of position,  $\frac{dC_1}{dt}$  should be zero, then

$$\frac{\partial \theta}{\partial t} = \frac{dC_2}{dt} \quad (19a)$$

Substituting Eqn (18) into Eqn. (19a)

$$\frac{dC_2}{dt} = \frac{c_f \alpha}{r_R} C_o \quad (19b)$$

After integration of Eqn. (19b)

$$C_2 = \frac{c_f \alpha}{r_R} C_o t + C_3 \quad (19c)$$

Substituting Eqn. (19c) into Eqn. (19)

$$\theta(x,t) = \frac{c_f}{\rho_R} C_o \frac{x^2}{2} + C_1 x + \frac{c_f \alpha}{\rho_R} C_o t + C_3 \quad (20)$$

Inlet BC

$$\frac{\partial P}{\partial x} = -\frac{u_o m}{k} \quad \text{at } x=0$$

Or

$$\frac{1}{c_f q} \frac{\partial q}{\partial x} = -\frac{u_o m}{k}$$

$$\frac{\partial q}{\partial x} = \frac{c_f}{r_R} C_o x + C_1$$

Then

$$\frac{1}{c_f q_o} \left( \frac{c_f}{r_R} C_o x + C_1 \right)_{x=0} = -\frac{u_o m}{k}$$

$$\frac{1}{c_f q_o} C_1 = -\frac{u_o m}{k}$$

$$C_1 = -\frac{u_o m}{k} c_f q_o \quad (20a)$$

Then

$$\theta(x,t) = \frac{c_f}{\rho_R} C_o \frac{x^2}{2} - \frac{u\mu}{k} c_f \theta_o x + \frac{c_f \alpha}{\rho_R} C_o t + C_3 \quad (20b)$$

Outlet BC

$$\frac{\partial P}{\partial x} = -\frac{u_L \mu}{k} \quad \text{at } x=L \quad (\text{volumetric flux condition})$$

Note that the outlet and inlet fluxes are not in general equal for compressible flow

$$\frac{1}{c_f q} \frac{\partial q}{\partial x} = -\frac{u_L m}{k}$$

$$\frac{\partial q}{\partial x} = -c_f q_L \frac{u_L m}{k} \quad \text{at } x=L \quad (20c)$$

The space derivative of Eqn. (20b) at  $x=L$  is

$$\frac{\partial q}{\partial x} = \frac{c_f}{r_R} C_o L + C_1 \quad (20d)$$

Substituting Eqn. (20c) and (20a) into (20d)

$$\frac{c_f}{r_R} C_o L + C_1 = -c_f \frac{u_L m}{k} q_L$$

---


$$C_o = \frac{\rho_R}{L} \left( -\frac{u_L \mu}{k} \theta_L + \frac{u_o \mu}{k} \theta_o \right)$$

Using the mass flux definition, we have

$$C_o = \frac{1}{L} \left( -\frac{m_L \mu}{k} + \frac{m_o \mu}{k} \right)$$

Defining the f-term as the outlet to inlet mass flux ratio

$$m_L = f m_o$$

The term f allows generality in the treatment of the condition at the external boundary (x=L). For f=1 the external boundary perfectly transparent (steady-state flow); for f=0 there is a perfectly sealed external boundary (semi steady-state flow). A partially sealed boundary would have 0<f<1.

We finally have,

$$C_o = \frac{m_o \mu}{kL} (1-f) \tag{21}$$

Substituting Eqn. (13) into (12b)

$$\theta(x,t) = \frac{c_f}{\rho_R} \frac{m_o \mu}{kL} (1-f) \left( \frac{x^2}{2} + \alpha t \right) - \frac{u \mu}{k} c_f \theta_o x + C_3$$

The additive constant  $C_3$ , can only be evaluated from a known pressure value, here we take

$$\theta = \theta_o \text{ At } x=0,$$

Then

$$q_o = \frac{c_f}{r_R} \frac{m_o m}{kL} (1-f) (\alpha t) + C_3$$

---


$$C_3 = \left( q_o - \frac{c_f}{r_R} \frac{m_o}{kL} m (1-f) (at) \right)$$

And finally we have,

$$\theta(x,t) = \frac{c_f}{\rho_R} \frac{m_o}{kL} \mu (1-f) \left( \frac{x^2}{2} \right) - \frac{u_o \mu}{k} c_f \theta_o x + \theta_o \quad (22)$$

Substituting  $\theta$  back into Eqn (22)

$$e^{c_f P(x,t)} = \frac{c_f}{\rho_R} \frac{m_o}{kL} \mu (1-f) \frac{x^2}{2} - \frac{c_f}{\rho_R} \frac{m_o}{k} \mu x + e^{c_f P_o} \quad (23)$$

As shown in Table 4 using volumetric fluxes (inlet and outlet) as boundary conditions

---

## Appendix B: Front Position Calculation

This section presents the solution for the front position calculation. We have shown in the body of this report that the instability analysis does not require the front position calculation, however we find it a useful contribution to track the displacement front as shown in Figure 9 through Figure 12.

The formulation starts adding a tracer to the solution above, Eqn (22)

$$\dot{m}A = \frac{d(Ax_f\phi\bar{\rho})}{dt} \quad (24)$$

For constant area

$$\dot{m} = \frac{d(x_f\phi\bar{\rho})}{dt} \quad (24a)$$

By definition

$$\bar{\rho} = \frac{\rho_R}{x_f} \int_0^{x_f} e^{c_f P} dx \quad (25)$$

Or

$$\bar{\rho} = \frac{\rho_R}{x_f} \int_0^{x_f} \theta(x, t) dx \quad (26)$$

Substituting  $\theta$  (Eqn 22) inside the integral in Eqn (26)

$$\bar{\rho} = \frac{\rho_R}{x_f} \int_0^{x_f} \left( \frac{c_f}{\rho_R} \frac{\dot{m}_o \mu}{Lk} (1-f) \left( \frac{x^2}{2} \right) - \frac{c_f}{\rho_R} \frac{\dot{m}_o \mu}{k} x + \theta_0 \right) dx \quad (26a)$$

After integration we have

$$\bar{\rho} = \rho_R \left( \frac{c_f}{\rho_R} \frac{\dot{m}_o \mu}{Lk} (1-f) \left( \frac{x_f^2}{6} \right) - \frac{c_f}{\rho_R} \frac{\dot{m}_o \mu}{k} \left( \frac{x_f}{2} \right) + \theta_0 \right) \quad (27)$$

Substituting Eqn (27) in Eqn (24a), we have

$$\dot{m}_o = \phi \rho_{R2} \frac{d \left( \frac{c_f}{\rho_R} \frac{\dot{m}_o \mu}{Lk} (1-f) \left( \frac{x_f^3}{6} \right) - \frac{c_f}{\rho_R} \frac{\dot{m}_o \mu}{k} \left( \frac{x_f^2}{2} \right) + \theta_0 x_f \right)}{dt}$$

---

Solving for the time derivative and rearranging terms

$$\dot{m}_o = \varphi \rho_R \left( \frac{c_f \dot{m}_o \mu}{\rho_R Lk} (1-f) \left( \frac{x_f^2}{2} \right) - \frac{c_f \dot{m}_o \mu}{\rho_R k} (x_f) + \theta_0 \right) \frac{d(x_f)}{dt}$$

Which gives the front velocity as

$$\frac{dx_f}{dt} = \frac{\dot{m}_o}{\varphi \rho_R \left( \frac{c_f \dot{m}_o \mu}{\rho_R Lk} (1-f) \left( \frac{x_f^2}{2} \right) - \frac{c_f \dot{m}_o \mu}{\rho_R k} (x_f) + \theta_0 \right)} \quad (28)$$

or

$$\frac{dx_f}{dt} = \frac{u_o e^{c_f P_o}}{\varphi \rho_R e^{c_f P_{x_f}}} \quad (28a)$$

$$\dot{m}_o t + CI = \varphi \rho_R \left( \frac{c_f \dot{m}_o \mu}{\rho_R Lk} (1-f) \left( \frac{x_f^3}{6} \right) - \frac{c_f \dot{m}_o \mu}{\rho_R k} \left( \frac{x_f^2}{2} \right) + \theta_0 x_f \right)$$

At t=0  $x_f=0$ , then

$$\dot{m}_o t = \varphi \rho_R \left( \frac{c_f \dot{m}_o \mu}{\rho_R Lk} (1-f) \left( \frac{x_f^3}{6} \right) - \frac{c_f \dot{m}_o \mu}{\rho_R k} \left( \frac{x_f^2}{2} \right) + \theta_0 (x_f) \right) \quad (29)$$

Perturbation analysis (second derivative of front velocity, Eq. (9a))

$$\dot{\epsilon} = \frac{d^2 x_f}{dt^2} = \frac{-\dot{m}_o \left( \frac{c_f \dot{m}_o \mu}{\rho_R Lk} (1-f) (x_f) - \frac{c_f \dot{m}_o \mu}{\rho_R k} \right)}{\varphi \rho_R \left( \frac{c_f \dot{m}_o \mu}{\rho_R Lk} (1-f) \left( \frac{x_f^2}{2} \right) - \frac{c_f \dot{m}_o \mu}{\rho_R k} (x_f) + \theta_0 \right)^2} \quad (30)$$